Terahertz cavity cooling for cuprate superconductors

SAMUEL JONATHAN DENNY

A thesis submitted in partial fulfilment of
the requirements for the degree of
Doctor of Philosophy at the University of Oxford

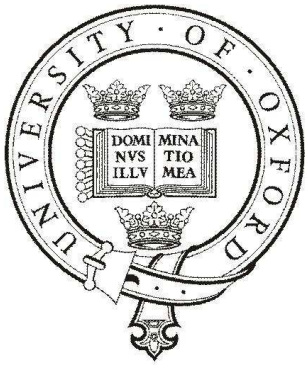

Exeter College
University of Oxford
Trinity Term 2015

Terahertz cavity cooling for cuprate superconductors

Samuel Jonathan Denny, Exeter College, Oxford

Trinity Term 2015

Abstract

Optical cooling is a well-established class of methods for reducing the temperature of a wide variety of atomic, mechanical and condensed matter systems. In this thesis, we demonstrate that it may be possible to cool the fluctuations of the Josephson phase in a cuprate single crystal by the application of coherent terahertz radiation. Such cooling strengthens the superconducting state as measured by switching current distribution, and may lead to an enhancement of the transition temperature T_c.

We develop a parametric cooling scheme for bilayer cuprates in which intense terahertz driving produces a modulation in the dielectric material properties. This modulates the coupling between interlayer and intralayer Josephson plasmons which we exploit to upconvert thermal fluctuations of the Josephson phase and reduce their effective temperature. We quantify this as the suppression of the fluctuations in both position and momentum quadratures, and additionally via simulated switching current measurements. We predict a reduction in temperature of 30% given realistic material parameters, and identify the cuprates YBCO and TBCCO-2201 as candidate materials in which this effect may be observed experimentally.

With a view to developing cavity cooling schemes, we study the coupling between the Josephson modes and the electromagnetic modes of an external cavity. Following a review of the literature, we examine in detail a specific microcavity array geometry which is expected to provide a large coupling through minimisation of the mode volume. Numerical calculations using finite element methods and an effective dielectric model suggest that strong coupling with $g/\omega_p \sim 0.2$ can be achieved using this geometry.

Contents

Contents ii

List of Figures iv

List of Symbols v

1 Introduction 1

2 Superconductivity 7
- 2.1 Josephson junctions . . . 10
  - 2.1.1 RCSJ model . . . 13
- 2.2 High-T_c superconductors . . . 14
  - 2.2.1 Josephson stack electrodynamics . . . 17
  - 2.2.2 In-plane dynamics . . . 20
- 2.3 Coupling between the Josephson phase and electromagnetic fields . . . 24
  - 2.3.1 Junction array in a cavity . . . 25
  - 2.3.2 Electrodynamical approach . . . 30
- 2.4 Summary . . . 31

3 Laser cooling methods 33
- 3.1 Cavity cooling of an optomechanical oscillator . . . 33
- 3.2 Josephson sideband scheme . . . 39
- 3.3 Parametric cooling . . . 42
- 3.4 Summary . . . 46

4 Parametric cooling in short junctions 47
- 4.1 Model derivation . . . 48
- 4.2 Toy model: Two junctions . . . 54
  - 4.2.1 Numerical results . . . 55
  - 4.2.2 Theory for cooling . . . 57
  - 4.2.3 Quantum regime . . . 59

4.3 Multilayered stack . . . 61
4.3.1 Temperature scale T_0 . . . 66
4.4 Summary . . . 67

5 Coupling the Josephson phase with a microcavity **69**
5.1 Introduction to the finite element method . . . 70
5.1.1 Formulation . . . 71
5.1.2 Microcavity array . . . 78
5.2 Single Josephson junction radiation via the finite element method . . . 81
5.2.1 Numerical results . . . 84
5.3 Microcavity array via the finite element method . . . 86
5.3.1 Effective tensor dielectric model . . . 89
5.3.2 Fitting a model Hamiltonian . . . 91
5.4 Outlook and further work . . . 93

6 Conclusions and Outlook **97**

Appendix A Numerical methods **99**
A.1 Langevin dynamics . . . 99
A.1.1 Numerical integrators . . . 100
A.1.2 Fokker-Planck formulation . . . 101

Bibliography **105**

List of Figures

2.1 Transition temperature T_c in BCS theory 10
2.2 Josephson junction schematic 11
2.3 Resistively- and capacitively-shunted Josephson model 13
2.4 A cuprate: YBCO atomic structure 15
2.5 2D XY model behaviour and Kosterlitz-Thouless transition 21
2.6 2D XY model lattice plots and vortices 24
2.7 Artificial Josephson array schematic 25

3.1 Optomechanical cavity cooling schematic 34

4.1 Schematic of bilayer cuprate geometry 49
4.2 Parametric cooling in a two-junction unit cell 56
4.3 Analytic theory of cooling efficiency 57
4.4 Quantum master equation calculation for two-junction unit cell 60
4.5 Parametric cooling of Josephson stack 62
4.6 Signature of cooling in stack switching current statistics 63
4.7 Systematics of parametric cooling of Josephson stack 64
4.8 Model transition temperature 66

5.1 Finite element sample problem schematic 72
5.2 Two-dimensional mesh and solution 79
5.3 Microcavity array spectral response 80
5.4 Single junction geometry 82
5.5 Single junction electrodynamics via FEM 85
5.6 3D and 2D microcavity array geometry 87
5.7 FEM calculations of 2D microcavity array, effective ϵ model 90
5.8 Double oscillator Hamiltonian spectra fit to FEM 94

List of Symbols

β_c	McCumber parameter
$\chi^{(j)}$	j^{th}-order nonlinear susceptibility
$\Delta\chi$	Josephson phase difference (as measured in a particular gauge)
Δ	BCS gap parameter
$\delta(t)$	Dirac delta distribution
Δ_c	Cavity detuning $\Delta_c = \omega_d - \Omega_c$
Δ_d	Discrete second derivative $\Delta_d Q_l = Q_{l+1} - 2Q_l + Q_{l-1}$
δ_{jk}	Kronecker delta
ϵ	Relative permittivity
ϵ_0	Free space permittivity $\epsilon_0 = 8.85 \times 10^{-12}$ F/m
ϵ_F	Fermi energy
Γ	Boundary label of FEM domain Ω
γ	Langevin damping rate
κ_c	Cavity decay rate
λ_c	London penetration depth (c-axis)
λ_L	London penetration depth
λ_{ab}	London penetration depth (ab-plane)
$\lambda_c^{(D)}$	Debye length

μ_0 Free space permeability $\mu_0 = 4\pi \times 10^{-7}$ N/A^2

ν Equilibrium occupation number

Ω FEM domain having boundary $\partial\Omega$

Ω_c Optical cavity frequency

ω_D Phonon Debye frequency

ω_d Angular driving frequency

ω_l, ω_h Low- and high-frequency Josephson plasmon frequencies

Ω_m Mechanical mode frequency

ω_p Josephson frequency (observed)

ϕ Gauge-invariant Josephson phase difference $\phi = \Delta\chi - \dfrac{2\pi}{\Phi_0}\int \vec{A}\cdot\vec{dl}$

Φ_0 Magnetic flux quantum, $\Phi_0 = h/2e = 2.07 \times 10^{-15}$ Wb

ψ Ginzburg-Landau complex order parameter

ρ Free charge density

ρ_s Superfluid density, having components $\rho_s^{(x)}$, $\rho_s^{(y)}$, $\rho_s^{(z)}$

Θ Electric scalar potential

Tr Trace (of a density matrix)

φ Normal coordinate of the gauge-invariant Josephson phase in a stack

ϖ Natural frequency of Josephson oscillators in stack (c.f. ω_p)

ς Anisotropy of a layered superconductor, $\varsigma = \lambda_c/\lambda_{ab} = \xi_{ab}/\xi_c$

$\vec{B}$ Magnetic flux density

$\vec{E}$ Electric field

$\vec{n}$ Outward normal on boundary of FEM domain Ω, pointing away from its interior

$\vec{dl}$ Line element

$\xi(t)$ Langevin noise term, assumed to be white and Gaussian

ξ_j Ginzburg-Landau coherence length along jth axis

C Capacitance

D	Cuprate insulator layer thickness
e	Electron charge $e = 1.60 \times 10^{-19}$ C
E_J	Josephson energy $E_J = \hbar I_c / 2e$
F	Free energy
$g(\epsilon_F)$	Electronic density of states at the Fermi energy
h, $\hbar$	Planck constant, reduced Plank constant $h = 6.63 \times 10^{-34}$ Js, $\hbar = h/2\pi$
I	Current
i	Imaginary unit $i = \sqrt{-1}$
I_{bias}	Applied bias current
I_c	Josephson critical current $I_c = J_c \times$ (junction area)
J	Current density
J_c	Josephson critical current density
k_B	Boltzmann constant $k_B = 1.38 \times 10^{-23}$ J/K
m_{eff}	Ginzburg-Landau effective mass
P	Polarisation density
R	Resistance
T	Temperature
t	Time
T_c	Transition temperature (of a superconductor)
t_I	Cuprate Cu-O layer thickness
u	Generic FEM solution, with $u = v + iw$.

1

Introduction

Since the discovery of superconductivity in 1911 [1], much attention has been given to the field due to both new technological possibilities as well as fundamental interest. The superconducting state is genuinely remarkable for its ability to carry a dissipationless current, in stark contrast to all previously known conductors. The first element discovered to have a superconducting phase was mercury, becoming superconducting when cooled below its critical temperature $T_c = 4.2$ K. Superconducting transitions at higher temperatures were discovered in other materials such as lead (7 K, 1913, [2]), niobium nitride (16 K, 1941, [3]), vanadium silicide (17 K, 1953, [4]), but these are all "conventional" superconductors which are well-described by the theory of Bardeen, Cooper and Schieffer [5] and have critical temperatures of no more than approximately 30 K. As such, their applications require liquid helium cooling and are expensive to operate.

This changed in 1986 with the discovery of $(LaBa)_2CuO_4$ [6], a ceramic beyond the scope of BCS theory and having a transition at 35 K. This was the first discovered "cuprate" superconductor, and it triggered enormous interest in seeking yet higher T_c materials due to the realisation that mechanisms beyond BCS could exist, potentially exceeding its apparent 30 K limit. Since then, new record-beating materials have been discovered, for example the cuprate YBCO in 1987 with a T_c of 92 K [7], and the current record is held by Hg-1223 ($HgBa_2Ca_2Cu_3O_8$) having $T_c = 134$ K at ambient pressure [8]. In general, higher values of T_c are favourable as less cooling is required and, all else being equal, applications should be cheaper as T_c increases. Any superconductor with a transition temperature above 77 K can be operated using liquid nitrogen, which is comparatively cheap with respect to other cryogenics. Even so, there are cases

when conventional superconductors are favoured. One such case is the Large Hadron Collider experiment, where the conventional superconductor NbTi is used for the 1200 tonnes of superconducting magnets. While this material has a T_c of 10 K, the magnets are operated at 1.9 K and cooled with helium. This operating temperature is below the helium superfluid transition at 2.2 K which substantially enhances its thermal conductivity and thus its efficacy for cooling. This implementation provides good overall performance of the cooling system. Nevertheless, the idea of ever higher values of T_c remains attractive, and the dream of eventually reaching room temperature persists. The implications for science and technology of such a drastic reduction in cost would be enormous.

A contributing factor to the current non-existence of a room-temperature superconductor is the lack of an underlying theory which satisfactorily explains, from a microscopic foundation, the mechanism of the high-T_c superconductors. There have been many attempts at this [9, 10], with part of the issue arising from poor overlap between measurable quantities and those which are clearly predicted in theory. This mismatch introduces multiple possibilities for interpretation and no clear consensus. One particular line of theory begins with the observation of Emery and Kivelson [11] that in the cuprates the superconducting carrier density is low and the electrostatic screening is poor. Both of these properties suggest that fluctuations of the complex phase of the order parameter should be important (in contrast to the conventional superconductors). Ref. [11] observes that the energy scale of long-range phase ordering closely follows the experimental T_c across the cuprates, suggesting a close link between the two. Specifically, the transition temperature is predicted to be the temperature at which the energy of thermal fluctuations is comparable with the phase ordering energy. Their work can be extended further into a more complete theory, for example the interlayer tunnelling theory [12, 13]. As with all existing theories of the cuprates this is considered controversial; we emphasise that our work is agnostic of the underlying theory of high-T_c superconductivity. However, a central tenet for this thesis is the acknowledgement of the strong evidence for the importance of classical phase fluctuations in the superconducting transition in cuprates.

With the cuprate superconductors forming the material subject of this thesis, the second principal thread concerns optical cooling. There is now a wide range of demonstrated experimental techniques whereby illuminating a system with light lowers its temperature. Initially this was of principal interest for spectroscopic purposes [14]:

the thermal distribution of energies of trapped ions undesirably broadens their spectra due to the Doppler shift, and optical cooling techniques were developed in order to reduce the kinetic energy of such trapped ions and increase the resolution of the spectra. More precisely, the electronic energy level structure of the ions provides a discrete set of possible electronic transitions, which when driven cause electrons to be excited by absorbing photons. Excited electrons eventually relax via isotropic spontaneous emission. Additionally, the photon absorption and emission processes involve an exchange of momentum, allowing the ion's kinetic energy to be reduced. There are further requirements such as that of a closed transition cycle, so that cooling can continue (as opposed to pumping all ions into states where they can no longer absorb), however this simple picture captures the essence of cooling with light. This is discussed in greater detail in Chapter 3.

It is also possible to optically cool macroscopic objects. This line of research arose from the needs of high-sensitivity Fabry-Pérot cavities, with the aim of detecting gravitational waves at facilities such as at the Laser Interferometer Gravitational-Wave Observatory (LIGO) in the US [15, 16]. In this case, a high finesse cavity with a length of 4 km is used to detect changes in the optical path on the order of 10^{-18} m. The mirrors must be laser cooled in order to achieve maximum sensitivity, placing them in their ground state and thus minimising the uncertainty in their position. The field of cavity optomechanics is generally interested in the coupling between optical and mechanical systems, including the gravitational wave detector case above, but also devices such as tunable optical filters and applications in optical quantum information processing where the nonlinearity of the interaction is crucial for developing a complete set of quantum gates [17]. The role of the cavity in such systems is to impose a carefully-designed electromagnetic mode structure upon the photon scattering processes, for example to enable selection of one sideband and thus one scattering process over another. This enables careful engineering of optomechanical cooling processes.

Laser cooling techniques have also been successfully applied in condensed matter systems, namely semiconducting materials and in transparent media with rare earth ion doping. This idea is not new, with the suggestion that anti-Stokes fluorescence can be used to cool the phonons of a solid material dating back to 1929 [18]. In 1968, Kushida and Geusic demonstrated lasing in Nd:YAG crystals[1] in which the heating from the

[1]Neodymium-doped yttrium aluminium garnet (Nd:YAG) is a common lasing medium used for solid-state lasers.

lasing process was reduced, attributed to an anti-Stokes process. In 1995, Epstein et al. [19] demonstrated net radiation cooling of 0.3 K below room temperature in a 43 mm^3 sample of ytterbium-doped fluorozirconate glass. The development of these cooling schemes in condensed matter systems has shown that optical cooling is not restricted to the simple and highly controllable scenarios of atomic and micromechanical systems. However, rare earth doping proved essential for providing an appropriate set of processes. The 4f electrons are optically active, allowing excitation and emission, while the screening by the occupied 5s and 5p outer shells limits the interaction with the surrounding lattice and heavily restricts nonradiative decay. This amounts to a high quantum efficiency for the anti-Stokes process: the fraction of incident photons which are upconverted and emitted from the sample must approach unity, otherwise the heating due to absorption of the remaining fraction is dominant. For a more complete overview of cooling in condensed matter systems, see the review of Nemova and Kashyap [20].

We propose to combine ideas from these fields; our aim in this thesis is to reduce the thermal fluctuations of the superconducting order parameter phase in cuprates via optical techniques. We pose the question of whether it is possible to extract energy from classical phase fluctuations of the superconducting order parameter through terahertz driving, and whether it is possible to do so at a sufficient rate that the effective temperature of these classical fluctuations is measurably reduced. Such a scheme can be orders of magnitude more efficient than cryogenic cooling, since in a small crystal the c-axis Josephson phase degrees of freedom contribute to the heat capacity an amount on the order of the number of layers, while the phonon contribution is on the order of the number of atoms in the crystal, thus the contribution from the Josephson phase is miniscule. We will restrict our attention to optical cooling of cuprates at temperatures *below* the superconducting transition, in which cooling has the physical consequence of strengthening the superconducting phase. Indeed, successful optical cooling above T_c would yield an out-of-equilibrium superconducting state in a sample above its equilibrium transition temperature. The experimental realisation of this is a long-term goal of this line of research, however its treatment lies beyond the scope of this thesis.

This work contributes to the Frontiers in Quantum Material Control (Q-MAC) project[2]. This project is composed of researchers from the Universities of Oxford, Paris and Geneva, and the Max Planck Institute for the Structure and Dynamics of Matter

[2]For further information, see `http://www.q-mac.eu`.

in Hamburg, and has the long-term goal of achieving stable high-temperature superconductivity via multiple approaches. These include approaches from materials science in which novel structures and materials may be fabricated, coherent terahertz probing of appropriate materials, and optical cooling approaches as taken in this thesis. Within the collaboration, there have now been many examples in which coherent light is used to drive a single low-energy degree of freedom in condensed matter systems [21–27], in which the driving is highly selective and produces little direct heating [28–32]. Systems with strong electronic correlations have been of principal interest for these methods, including materials displaying ferroelectricity and colossal magnetoresistance. Concerning cuprate superconductors, Refs. [23, 25] have demonstrated how femtosecond terahertz pulses may dynamically transform the material $La_{1.675}Eu_{0.2}Sr_{0.125}CuO_4$ from an insulating stripe-ordered phase into a superconductor, experimentally observed as a c-axis Josephson plasma resonance in the optical response. Later work [26, 27] demonstrated that a coherent excitation of the apical oxygen in the YBCO unit cell induced transient superconducting fluctuations at temperatures as high as 300 K. These experimental results on the manipulation of superconducting fluctuations provide direct inspiration for the present work.

In addition to the above, initial experiments are underway to explore the cavity-coupling of the Josephson phase. The work leading up to Ref. [33] dates back to the spring of 2013, where possible ways of arranging a cuprate crystal inside a terahertz cavity with minimal mode volume were considered. The geometry chosen allows for a sub-wavelength mode volume and is also amenable to fabrication by layered deposition, allowing the construction of such microcavities. The challenges there include matching insulating, superconducting and metallic materials, all of which must have compatible lattice dimensions for successful interfacing at the atomic scale. The most recent challenges involve navigating the proximity effects that one material may have at the interface with another, and in the case of very thin layers can potentially dominate the physics – here, suppressing the superconducting state. When these challenges are overcome, it will be possible to measure directly the Josephson phase-cavity coupling and begin an experimental study of cavity-based laser cooling schemes for cuprates.

This thesis is structured as follows. In the next chapter, we introduce conventional superconductors and the Josephson effect, followed by high-T_c superconductors and their low-energy description in terms of an intrinsic Josephson stack. We discuss the dynamics of the Josephson phase arising from the coupling between Cu-O layers, and

then later in Sec. 2.2.2 discuss the phase dynamics that occur within the 2D condensate, which become increasingly relevant as the temperature T_c is approached. Additionally, we review the existing approaches in the literature regarding the coupling between the Josephson phase and external electromagnetic modes.

In Chapter 3 we introduce the physics of optical cooling. First, we examine optomechanical cooling in detail in order to illuminate the underlying physical processes, and especially the properties of the system that enable cooling to be achievable at all. We also study the Josephson sideband scheme of Hammer, Aprili, and Petković [34], in which a cooling effect was measured experimentally in an artificial junction, and introduce the parametric cooling scheme which be later applied in Chapter 4.

In Chapter 4 we first address the problem of upconverting Josephson phase fluctuations, an essential first step in any proposed cooling scheme. This chapter is based on the publication Ref. [35], and makes a detailed proposal for cooling Josephson phase fluctuations in bilayer cuprates via the parametric cooling scheme described in Sec. 3.3. We are able to identify several possible candidates for attempting to observe the effect experimentally. Since the cooling scheme upconverts fluctuations to the intrabilayer mode, this is not viable as a continuous cooling scheme, for which we would require a coupling to an external bath. This is precisely the focus of Chapter 5, where we study the interaction between the Josephson phase and the external electromagnetic field. We first introduce the finite element method for electromagnetic problems, then numerically study the model of Bulaevskii and Koshelev [36]. We extend this to the microcavity array geometry of current interest, and find evidence of good Josephson-cavity coupling in this scenario using the effective dielectric model of Ref. [33].

2

Superconductivity

The phenomenon of superconductivity was first observed in 1911 by H. K. Onnes, in an experiment in which the resistance of mercury suddenly became indistinguishable from zero at 4.19 K [1]. Further experiments performed on this "perfect conductor" revealed the reversibility of this transition and persistence of the supercurrent [37]. Additionally, magnetic fields up to a critical field B_c were found to be expelled by the material [37]. Later, in 1933 Meissner and Ochsenfeld [38] showed that a magnetic field present in a material above its transition temperature is expelled when the superconducting state forms upon lowering the temperature. The superconducting state thus displays perfect diamagnetism. Meanwhile, several theories of the superconducting state appeared.

With no latent heat at the transition temperature $T = T_c$ (in zero magnetic field), the phase transition was known to be second order and should be describable within Landau's theory [39, 40]. In the Ginzburg-Landau description, a complex order parameter ψ is introduced in analogy with the theory developed for superfluid helium. As a function of temperature, ψ is expected to be finite for $T < T_c$, and zero for $T \geq T_c$. The free energy F_s of the superconducting state is required to be a continuous function of ψ[1] and so in the vicinity of T_c one assumes a series expansion around $\psi = 0$ [41],

$$F_s(T) - F_n(T) = \int dV \left(a(T)|\psi(\vec{x})|^2 + \tfrac{1}{2} b(T)|\psi(\vec{x})|^4 + \frac{\hbar^2}{2m_{\text{eff}}} |\nabla\psi(\vec{x})|^2 \right). \qquad (2.1)$$

This is the lowest order expansion which allows for a symmetry-breaking transition as the sign of $a(T)$ changes, and also includes a kinetic energy term $(\hbar^2/2m_{\text{eff}})|\nabla\psi(\vec{x})|^2$ where m_{eff} is an effective mass. The free energy of the normal state is accounted for in

[1] The free energy F depends continuously on ψ, since ψ should be a physical quantity.

$F_n(T)$. Taylor-expanding the coefficients $a(T)$ and $b(T)$ around $T = T_c$, we must have

$$F_s(T) - F_n(T) = \int dV \left(a_0(T - T_c)|\psi(\vec{x})|^2 + \tfrac{1}{2} b_0 |\psi(\vec{x})|^4 + \frac{\hbar^2}{2m_{\text{eff}}} |\nabla \psi(\vec{x})|^2 \right), \quad (2.2)$$

to lowest order in $(T - T_c)$. The homogeneous solution $\psi(\vec{x}) = \psi_0$ then has the desired transition at T_c. In the presence of magnetic fields, one makes the standard quantum mechanical replacement of the kinetic term to

$$\frac{1}{2m_{\text{eff}}} \left| \left(\frac{\hbar}{i} \nabla + 2e\vec{A} \right) \psi \right|^2,$$

where e is the electron charge and $\vec{A}$ the vector potential. This is the appropriate replacement for particles having charge $2e$ and effective mass m_{eff}. The field $\psi(\vec{x})$ which minimises Eq. (2.2) satisfies

$$-\frac{\hbar^2}{2m_{\text{eff}}} \left(\nabla + \frac{i}{\hbar} 2e\vec{A} \right)^2 \psi(\vec{x}) + \left(a + b|\psi(\vec{x})|^2 \right) \psi(\vec{x}) = 0. \quad (2.3)$$

Through Eq. (2.3), the Ginzburg-Landau theory provides a powerful phenomenological framework, capable of explaining much of the physics of superconductivity, covering all of the physics contained in the London theory as well as nonlinear effects in which the pairing density is modified. In 1957, Bardeen, Cooper, and Schrieffer [5] set out a microscopic theory of superconductivity in which the pairing mechanism arises from an electron-phonon interaction. The BCS theory is not of direct relevance for this thesis, and so we refer to the literature for full details [42, 43]. However, in order to appreciate the distinguishing characteristics of the cuprates, we discuss briefly a few aspects of BCS theory here.

As a consequence of the electron-phonon coupling and Thomas-Fermi screening of the electron-electron interaction at large separation, a weak effective electron-electron interaction arises, and is attractive at the relevant energies around the Fermi energy ϵ_F. In BCS theory, this is approximated as $V_{\text{eff}} = -|g_{\text{eff}}|^2$, i.e. a weak, frequency-independent attractive force. The BCS "pairing Hamiltonian"

$$\hat{H} = \sum_{\vec{k},\sigma} \epsilon_{\vec{k}} \hat{c}^\dagger_{\vec{k},\sigma} \hat{c}_{\vec{k},\sigma} - |g_{\text{eff}}|^2 \sum_{\vec{k},\vec{k}',\vec{q}} \hat{c}^\dagger_{\vec{k}+\vec{q},\uparrow} \hat{c}^\dagger_{-\vec{k},\downarrow} \hat{c}_{-\vec{k}'+\vec{q},\downarrow} \hat{c}_{\vec{k}',\uparrow} \quad (2.4)$$

is assumed to contain the only terms necessary for conventional superconductivity, where the operator $\hat{c}^\dagger_{\vec{k},\sigma}$ ($\hat{c}_{\vec{k},\sigma}$) describes the creation (annihilation) of an electron in a state with momentum $\vec{k}$ and spin σ. The first term contains the energy of an electron

having momentum $\vec{k}$, and the second term describes momentum- and energy-conserving scattering of pairs of electrons. In Cooper's problem [44], it was demonstrated that a bound state of two electrons (with states $\vec{k},\uparrow$ and $-\vec{k},\downarrow$) forms in the presence of a fixed Fermi sea for arbitrarily weak coupling g_{eff}. This is known as a Cooper pair. The final piece in BCS theory is to put forward the approximate BCS wavefunction,

$$|\psi_{\text{BCS}}\rangle = \prod_{\vec{k}} \left(u_{\vec{k}} + v_{\vec{k}} \hat{c}^{\dagger}_{\vec{k},\uparrow} \hat{c}^{\dagger}_{-\vec{k},\downarrow} \right) |0\rangle \,, \tag{2.5}$$

where $u_{\vec{k}}$ and $v_{\vec{k}}$ are variational parameters. This is an analytically tractable many-body wavefunction to describe the relevant electrons close to the Fermi energy as comprising a coherent state. This is a phase-coherent many-body quantum state in which operators such as $\hat{c}^{\dagger}_{\vec{k},\uparrow} \hat{c}^{\dagger}_{-\vec{k},\downarrow}$ can take on finite expectation values, in contrast with the normal state in which such operators have zero expectation value.

BCS theory provides a satisfactory microscopic basis for conventional superconductivity, and explains the isotope effect and underlying pairing mechanism [41]. A key prediction of BCS is that the gap parameter Δ at $T = 0$ is

$$|\Delta(0)| = 2\hbar\omega_D \exp\left(-\frac{1}{|g_{\text{eff}}|^2 g(\epsilon_F)} \right), \tag{2.6}$$

in which ω_D is the phonon Debye frequency and $g(\epsilon_F)$ is the density of states at the Fermi energy. The gap parameter $|\Delta(0)|$ is connected to the value of T_c, namely

$$2|\Delta(0)| = 3.52 k_B T_c. \tag{2.7}$$

In many materials, this effectively sets a limit on the maximum T_c achievable given this mechanism: a higher T_c implies a higher gap parameter $|\Delta(0)|$, which in turn requires a larger g_{eff}, and stronger electron-phonon interactions. However, past $T_c \sim 30$ K, the electron-phonon interaction is of sufficient strength that in many materials the normal metal state becomes unstable to a charge-density wave insulating state [45] (sketched in Fig. 2.1)[2]. However, there are very recent experiments on hydrogen sulfide H_2S demonstrating a superconducting state up to 203 K at a pressure of 90 GPa [48]. The presence of the isotope effect ($T_c \propto m^{-\alpha}$ with $\alpha \approx 0.5$, where m represents the atomic mass) strongly indicates a BCS-type mechanism, and thus a "conventional" superconductor with an extremely high T_c.

[2]There are a couple of loopholes to this, for example in the case of MgB_2 in which two bands conspire to produce a T_c of 39 K [46], or in the case of phonon anharmonicity in the presence of strong-coupling [47].

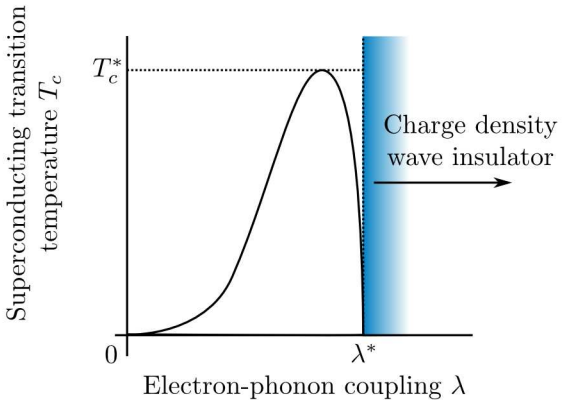

Figure 2.1: Sketch of variation of transition temperature T_c for many BCS superconductors with the electron-phonon coupling $\lambda = |g_{\text{eff}}|^2 g(\epsilon_F)$. In many materials, strong electron-phonon coupling yields a charge density wave insulating state rather than a superconductor with high T_c.

In the BCS ground state, all electrons around the Fermi surface form a coherent state of Cooper pairs. Excitations correspond to the breaking of these pairs, with a concomitant reduction in the BCS gap. In Sec. 2.2 we will contrast this behaviour with that of the cuprates.

2.1 Josephson junctions

In 1962, B. D. Josephson considered the tunnelling currents between two superconducting materials within the BCS theory [49]. Rather than revisiting his microscopic derivation, the essential physics can be revealed by an intuitive physical argument due to Feynman [50]. We emphasise at this point that the results of Josephson's derivation are not restricted to BCS superconductors, nor indeed to the geometry presented in Fig. 2.2. They are applicable to any pair of superconducting regions in close proximity, separated by an insulator, metal, or narrow constriction [41]. On the left side, the superconducting electron pairs are in a macroscopic quantum state with amplitude ψ_l which is assumed to obey a Schrödinger equation $i\hbar\frac{\partial\psi_l}{\partial t} = U_l\psi_l$ [50]. Likewise for the right junction, and in the presence of a coupling K between them, their dynamics are

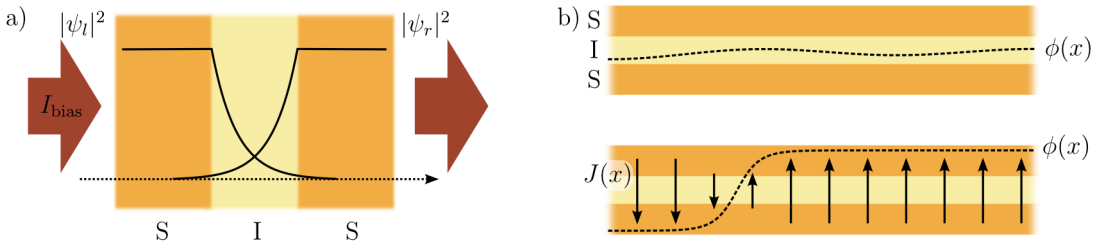

Figure 2.2: a) Sketch of a Josephson junction. The left and right superconducting regions have macroscopic wavefunctions ψ_l and ψ_r respectively; their overlap is responsible for the tunnelling central to the Josephson effect. b) Excitations of the Josephson phase. Above: (linear) excitations of the Josephson phase with finite k in-plane. Below: for contrast, excitations exist in which the Josephson phase revolves through 2π in a localised region of the junction. These excitations, known as Josephson vortices, can have momentum and thus propagate. In addition to the Josephson phase, the supercurrent flow $J(x)$ is indicated.

assumed to follow[3]

$$\begin{aligned} i\hbar\frac{\partial\psi_l}{\partial t} &= U_l\psi_l + K\psi_r, \\ i\hbar\frac{\partial\psi_r}{\partial t} &= U_r\psi_r + K\psi_l, \end{aligned} \tag{2.8}$$

assuming the simplest case of a symmetric junction. If the potential difference across the junction is V, we can choose $U_l = \frac{1}{2}\times 2eV$ and $U_r = -\frac{1}{2}\times 2eV$, with $2e$ being the charge of a Cooper pair. The relative phase of the amplitudes is of key importance to the dynamics, so we move to the representation

$$\psi_l = \sqrt{\rho_l}\exp(i\chi_l), \qquad \psi_r = \sqrt{\rho_r}\exp(i\chi_r).$$

Here, ρ_l (ρ_r) is the number density of the l (r) macroscopic wavefunction and χ_l (χ_r) is its complex phase. Substituting this representation into Eq. (2.8) gives the dynamics

$$\begin{aligned} \frac{\partial\rho_l}{\partial t} &= \frac{2}{\hbar}K\sqrt{\rho_l\rho_r}\sin(\chi_r-\chi_l), \\ \frac{\partial\rho_r}{\partial t} &= -\frac{2}{\hbar}K\sqrt{\rho_l\rho_r}\sin(\chi_r-\chi_l), \end{aligned} \tag{2.9}$$

$$\begin{aligned} \frac{\partial\chi_l}{\partial t} &= \frac{K}{\hbar}\sqrt{\frac{\rho_r}{\rho_l}}\cos(\chi_r-\chi_l) - \frac{eV}{\hbar}, \\ \frac{\partial\chi_r}{\partial t} &= \frac{K}{\hbar}\sqrt{\frac{\rho_l}{\rho_r}}\cos(\chi_r-\chi_l) + \frac{eV}{\hbar}. \end{aligned} \tag{2.10}$$

[3]The coupling K intuitively describes a rate of tunnelling across the junction.

There is an instantaneous current

$$J = \frac{2K}{\hbar}\sqrt{\rho_l \rho_r}\sin\Delta\chi, \tag{2.11}$$

defining $\Delta\chi = \chi_r - \chi_l$, the phase difference between the superconducting wavefunctions. We now perform a trick to account for the effect of any external battery, which is to hold constant the electron densities ρ_i, effectively by adding constant terms to Eq. (2.9). Eq. (2.11) then demonstrates that there is a tunnelling current between the electrodes taking maximum absolute value $J_{c,0} = \frac{2K}{\hbar}\sqrt{\rho_l\rho_r}$, and proportional to $\sin\Delta\chi$. The relation Eq. (2.10) can be arranged as

$$\frac{\partial\Delta\chi}{\partial t} = \frac{2eV}{\hbar}, \tag{2.12}$$

stating that a potential difference across the junction causes time-evolution of the Josephson phase. Eqs. (2.11–2.12) constitute the Josephson relations.

We now introduce the idea of a gauge-invariant Josephson phase. The present description of Josephson junctions is not invariant to gauge transformations, which have the form $\vec{A} \to \vec{A} + \nabla f$ for an arbitrary function f. The two phases transform as

$$\begin{aligned} \chi_l &\to \chi_l - \frac{2e}{\hbar}f, \\ \chi_r &\to \chi_r - \frac{2e}{\hbar}f, \end{aligned} \tag{2.13}$$

and so we can define a *gauge-invariant* phase difference ϕ as

$$\phi = \chi_r - \chi_l + \frac{2e}{\hbar}\int_l^r \vec{A}(\vec{x},t)\cdot\vec{dl}, \tag{2.14}$$

where the line integral is along a path from the left junction to the right. The quantity ϕ is now properly invariant under gauge transformations, and is the correct quantity to use to derive the Josephson current, as

$$J = J_{c,0}\sin\phi. \tag{2.15}$$

Similarly, Eq. (2.12) is replaced with

$$\frac{\partial\phi}{\partial t} = \frac{2eV}{\hbar}. \tag{2.16}$$

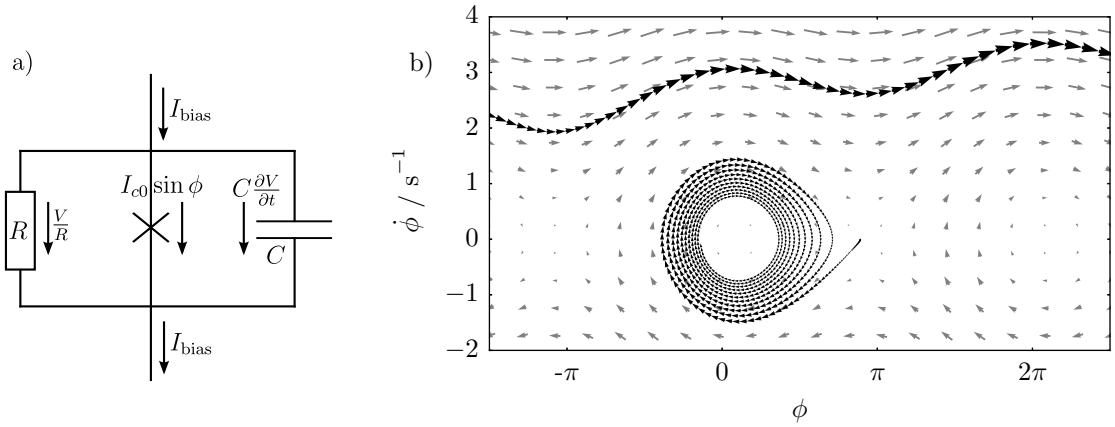

Figure 2.3: (a) RCSJ model. The "ideal" Josephson junction (marked by a cross) is augmented by a capacitance C and a resistance R to model a dissipative quasiparticle contribution. These circuit components model additional current paths across the junction. (b) Trajectories in phase space for the RCSJ model. Parameters used were McCumber parameter $\beta_c = 2500, \omega_{p,0} = 1\ \text{s}^{-1}, I_{\text{bias}}/I_{c,0} = 0.3$. The background grey arrows indicate the local flow at each point $(\phi, \dot{\phi})$, with two qualitatively distinct trajectories plotted in black. Larger arrowheads correspond to more rapid flows through phase space. The lower trajectory is in the superconducting state, with its phase ϕ oscillating about equilibrium. The amplitude of the oscillations decay by approximately $2\pi/\sqrt{\beta_c}$ per cycle. The upper trajectory has slipped into the resistive state, indicated by a finite time-averaged potential difference $\langle V \rangle \propto \langle \dot{\phi} \rangle$. The fictitious particle accelerates as it receives energy from the bias current.

2.1.1 RCSJ model

In this section, we introduce a simple model to account for dissipation and charging of the electrodes of the junction. The resistively and capacitively shunted junction (RCSJ) model provides a useful picture of the dynamics of a real Josephson junction [41]. Eqs. (2.15, 2.16) describe an "ideal" Josephson junction. Two pieces of physics missing from this picture are that at finite temperature, a dissipative quasiparticle current may flow between the electrodes, and furthermore that they may charge as in a capacitor. We incorporate these effects as three parallel current paths between the electrodes, as depicted in Fig. 2.3(a). We write the total current through the junction

as

$$I_{\text{bias}} = I_{c,0} \sin\phi + \frac{V}{R} + C\frac{\partial V}{\partial t}, \tag{2.17}$$

in which V is the potential difference across the junction, R is the effective circuit resistance arising from quasiparticle tunnelling, and C is the circuit capacitance of the junction. Making use of Eq. (2.12) to replace the potential difference V, we find that the dynamics of ϕ obey

$$I_{\text{bias}} = I_{c,0} \sin\phi + \frac{\hbar}{2eR}\frac{\partial\phi}{\partial t} + \frac{\hbar C}{2e}\frac{\partial^2\phi}{\partial t^2}. \tag{2.18}$$

We extract two timescales from this: the Josephson plasma frequency $\omega_{p,0} = \sqrt{2eI_{c,0}/\hbar C}$ and the McCumber parameter $\beta_c = (\omega_{p,0}RC)^2$ [51]. This equation describes a nonlinear oscillator[4]. We can understand its behaviour from its trajectories in phase space, considering the coordinates $(\phi, \dot{\phi})$, as depicted in Fig. 2.3(b). There are two qualitative behaviours of this oscillator. The first can be seen via linearisation of the $\sin\phi$ term, and corresponds to small oscillations about an equilibrium phase $\bar{\phi}$. In this state, the time-averaged potential difference $\langle V\rangle = \frac{\hbar}{2e}\langle\partial_t\phi\rangle = 0$; this is known as the superconducting junction state. The other distinct state is one in which $|\langle\partial_t\phi\rangle| > 0$ and the Josephson phase ϕ continually winds up. Since there is a finite time-averaged potential difference, resistive quasi-particle tunnelling also occurs leading to dissipation and heating. This is known as the resistive state.

When there is a finite bias current I_{bias}, the equilibrium Josephson phase ϕ_0 shifts to $\sin\phi_0 = I_{\text{bias}}/I_{c,0}$, and the effective Josephson frequency is reduced according to

$$\begin{aligned}\omega_p^2 &= \omega_{p,0}^2 \cos\phi_0 \\ &= \omega_{p,0}^2\sqrt{1-(I_{\text{bias}}/I_{c,0})^2}.\end{aligned} \tag{2.19}$$

When $I_{\text{bias}} \to I_{c,0}$, $\omega_p \to 0$.

2.2 High-T_c superconductors

The discovery of superconductivity in $(\text{LaBa})_2\text{CuO}_4$ in 1986 by Bednorz and Müller [6] was the first of a series of high-T_c superconductors, so-called since their values of T_c commonly exceed the ~ 30 K limit imposed by BCS theory. This class of superconductors,

[4]The dynamics described by Eq. (2.18) are analogous to a particle of mass $(\hbar/2e)^2C$ moving in a potential $U(\phi) = -(\hbar I_{c,0}/2e)(\cos\phi + \frac{I_{\text{bias}}}{I_{c,0}}\phi)$ [41]. This is commonly known as the "tilted-washboard potential" of a Josephson junction.

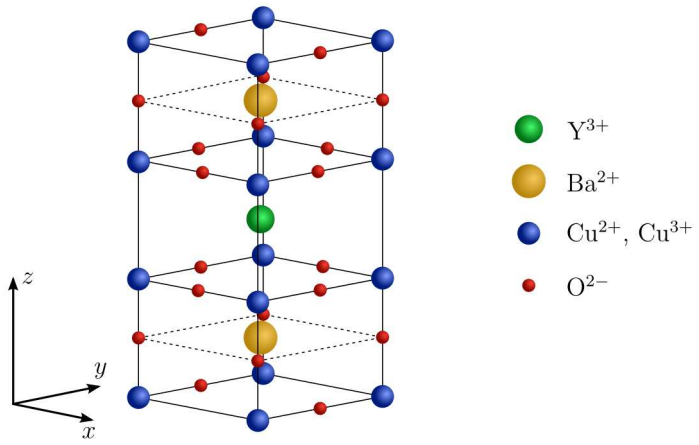

Figure 2.4: Structure of the high-temperature superconductor $YBa_2Cu_3O_{7-x}$ (YBCO-123). Cu and O atoms form quasi-two-dimensional sheets in the xy plane.

referred to as cuprates due to the common feature of Cu-O planes in their structure, demonstrates transition temperatures currently up to 140 K (for the mercury-based compound $Hg_{0.8}Tl_{0.2}Ba_2Ca_2Cu_3O_{8+\delta}$[5] [8]). Some materials from the cuprate class are of particular relevance for industry, especially $(Bi,Pb)_2Sr_2Ca_2Cu_3O_{8+x}$, $Bi_2Sr_2CaCu_2O_{8+x}$ and $YBa_2Cu_3O_7$ [52], enabling comparatively cheap applications of superconductivity owing to their T_c exceeding the boiling point of nitrogen. In general, however, applications at 77 K have proved to be more complicated than at lower temperatures [52, 53]. The enhanced thermal fluctuations in cuprates restricts the useful region of the temperature-magnetic field phase diagram, while current-limiting grain boundaries necessitate the use of complex manufacturing techniques such as coated-conductor technology [54].

The atomic structure of a common high-temperature superconductor, $YBa_2Cu_3O_{7-x}$ (YBCO-123) is sketched in Fig. 2.4. Early measurements of the magnetic flux quantisation [55] have demonstrated that electron pairs are also responsible for the superconducting state, although the microscopic details of the pairing mechanism remain unresolved [56]. Nevertheless, phenomenological theories based on Ginzburg-Landau theory provide a working description of the physics of these systems. The Lawrence-Doniach model is an anisotropic Ginzburg-Landau theory, in which the superconducting order

[5]Higher values of T_c can be achieved by cuprates under pressure to distort the lattice.

parameter ψ minimises the free energy[6] [41]

$$F = \sum_n \int dV \Bigg\{ a(T)|\psi_n|^2 + \tfrac{1}{2} b(T)|\psi_n|^4 + \frac{\hbar^2}{2m_{ab}} \left(\left| \frac{\partial \psi_n}{\partial x} \right|^2 + \left| \frac{\partial \psi_n}{\partial y} \right|^2 \right) + \frac{\hbar^2}{2m_c D^2} |\psi_n - \psi_{n-1}|^2 \Bigg\}, \quad (2.20)$$

in analogy with Eq. (2.1), but where the z-derivative has become discrete to address the cuprates' layered structure. The interlayer separation is D. With differing effective masses m_{ab} and m_c[7], the coherence length ξ_i becomes anisotropic,

$$\xi_i^2(T) = \frac{\hbar^2}{2m_i|a(T)|}. \quad (2.21)$$

A descriptive parameter for layered superconductors is the temperature-dependent anisotropy $\varsigma = \xi_{ab}/\xi_c$. $Bi_2Sr_2CaCu_2O_8$ (BSCCO) is particularly anisotropic, with $\varsigma \sim 10^3$, while YBCO is less so with $\varsigma \sim 5$ [57]. In the limit of $\varsigma \gg 1$, the cuprate is best described as consisting of two-dimensional superconducting sheets with weak interlayer coupling arising from the c-axis coherence length ξ_c. Notice in particular that the coherence lengths $\xi_i(T)$ diverge as $|T - T_c|^{-1/2}$ as $T \to T_c$. Considering ξ_c, sufficiently close to T_c the layered nature of the cuprate becomes less relevant and a continuum anisotropic Ginzburg-Landau model becomes more appropriate. In other words, the lengthscale of variation of ψ can substantially exceed the 2D layer spacing and a continuous three-dimensional description is more suitable. The crossover temperature varies according to the material, for example YBCO behaves as a layered material up to ~ 80 K ($T_c = 93$ K) while in the case of BSCCO this behaviour persists until 0.1 K below T_c.

In addition to the differences with BCS superconductors already described, there are fundamental differences in the nature of the transition at T_c. A BCS superconductor becomes a normal metal above T_c, while the cuprates enter a pseudo-gap phase in which there is spectroscopic evidence for pairing to exist up to a temperature T^* which can be 100 K above T_c [58–60]. Furthermore, the approach to T_c from below is somewhat different from that in BCS materials. As Emery and Kivelson [11, 61]

[6] Additional terms are required in the presence of electromagnetic fields [41].

[7] In crystallography, the x, y and z axes are commonly labelled a, b and c. We will frequently refer to the "ab plane" for the xy plane containing Cu-O sheets, and the c axis running perpendicular to the cuprates' layered structure.

highlight, in the cuprates the carrier density is low and electrostatic screening is poor. A low carrier density n_s is directly related to a low phase stiffness implying a greater susceptibility to classical phase fluctuations. Additionally, phase coherence in these materials must correspond to large quantum fluctuations in the superconducting carrier density through phase-number uncertainty. Without good screening, the electrostatic energy associated with these number fluctuations will increase the state energy. In this thesis we focus entirely on the former, on classical phase fluctuations.

There are entire theories of high-T_c materials based around the Josephson interlayer tunnelling [12, 13, 62–64]. In light of their somewhat controversial nature, we do not interpret these literally as complete descriptions of high-T_c materials. However, we do acknowledge that there is substantial evidence in favour of phase fluctuations driving the phase transition at T_c. Additional physics is almost certainly required to describe the entire phase diagram in this region, but for the application of cooling we should be able to focus on the dominant physics around T_c. Thus we pose the question of whether and how such phase fluctuations may be suppressed, and realistically expect this to have an influence on the superconducting transition.

2.2.1 Josephson stack electrodynamics

In this section we will describe the common models for describing Josephson dynamics in cuprates. With sufficient anisotropy, the cuprates behave as quasi-two-dimensional superconductors with the weak c-axis coupling giving rise to Josephson physics. These models arise from the THz generation literature, where the goal is to exploit the natural THz frequencies of intrinsic Josephson oscillators as coherent sources of THz radiation.

Initially, Kleiner et al. [65] proposed a conceptual model for BSCCO consisting of discrete two-dimensional superconducting sheets (the Cu-O planes) separated by insulating regions. They performed experiments on BSCCO single crystals of dimension 30 μm $\times$ 30 μm $\times$ 3 μm, stacks of $\sim$ 2000 junctions and found hundreds of branches on the current-voltage (I-V) characteristic curves, indicative of many individual junctions, with branches differing in the number of resistive junctions in the stack. Additionally they observed the Fraunhofer critical current dependence on magnetic field B. Similar behaviour has been found in other cuprates, and with other phenomena such as Fiske resonances [66–68] and Shapiro steps [69–71][8].

[8] Assuming a voltage bias of $V = V_0 + V_1 \cos \omega_1 t$, whenever $V_0 = n\hbar\omega_1/2e$ there is a DC contribution

Mathematically, such stacks of junctions may be modelled either via the Lawrence-Doniach theory [72, 73], or with a classical electrodynamical theory (e.g. [74]). Both routes lead to similar models, with the main differences arising from how the screening is approximated, whether the capacitive coupling is included, and so forth. We focus on the approach using classical electrodynamical theory as it gives a clearer physical picture. Here we show how the Josephson electrodynamics gives rise to a coupled sine-Gordon description for the Josephson phase. A more detailed derivation will be given in Chapter 4 when we consider the microscopic details when subject to nonlinear THz-frequency driving.

In Ginzburg-Landau theory, the supercurrent may be written as

$$\vec{J} = \frac{1}{\mu_0 \lambda_L^2} \left[\frac{\Phi_0}{2\pi} \nabla\chi - \vec{A} \right],$$

in which λ_L is the London penetration depth, χ is the complex phase of the superconducting order parameter and $\Phi_0 = h/2e$ is the magnetic flux quantum. Applying this to the region around a Josephson junction, we can relate gradients in the (gauge-invariant) Josephson phase ϕ_l in the xy plane to the currents $\vec{J}_l$ flowing above $(l+1)$ and below (l) the junction, and the magnetic field B_l threading that area, according to

$$\nabla_{xy}\phi_l = \frac{2\pi}{\Phi_0}\mu_0\lambda_{ab}^2(\vec{J}_{l+1} - \vec{J}_l) + \frac{2\pi D}{\Phi_0}\vec{B}_l \times \vec{z}, \tag{2.22}$$

where ∇_{xy} denotes the gradient operator in the xy plane. The junction thickness is denoted by D. We write λ_{ab} since the penetration depth is anisotropic, and the ab component is the relevant orientation here[9]. Making the simplifying assumption that there is no induced finite charge density[10] ρ, we may express charge conservation as $\nabla \cdot \vec{J} = 0$. Taking an additional finite difference in z this may be written as

$$\partial_x(J_{l+1}^x - J_l^x) + \partial_y(J_{l+1}^y - J_l^y) = -\frac{1}{D}\Delta_d J_l^z, \tag{2.23}$$

to the Josephson supercurrent. These DC contributions accumulate as the radio-frequency voltage V_1 is increased. Shapiro steps are then the discrete jumps in the I-V characteristic as V_1 is increased.

Meanwhile, Fiske resonances occur only in long Josephson junctions. Such long junctions behave as open-ended transmission lines, supporting self-resonant modes. When a finite voltage is applied across the junction, the junction is driven at frequency $\omega = 2eV/\hbar$, which may interact with the self-resonant modes which in turn interact with the Josephson current. When the frequency ω matches the frequency of an intrinsic cavity mode, this produces a a DC current component observed as a Fiske resonance in the I-V characteristic.

[9]The penetration depth λ_{ab} describes the screening by supercurrents flowing in the ab plane.

[10]Due to the mobile charge carriers provided by the Cu-O planes, it is not expected that any localised charge density should accumulate.

where Δ_d is the discrete second derivative $\Delta_d Q_l = Q_{l+1} - 2Q_l + Q_{l-1}$. Combining the above with the Maxwell equation

$$\nabla \cdot \vec{E} = \frac{\rho}{\epsilon\epsilon_0},$$

where ϵ_0 is the vacuum permittivity, we reach

$$(\partial_x^2 + \partial_y^2)\phi_l = \left(1 - \frac{\lambda_{ab}^2}{D^2}\Delta_d\right)\left(\frac{2\pi D}{\Phi_0}\mu_0 J_l^z + \frac{2\pi D}{\Phi_0}\frac{\epsilon}{c^2}\partial_t E_l^z\right). \tag{2.24}$$

Using the Josephson relations and expressing the current density $J_l^z = \sigma E_l^z + J_c \sin\phi_l$, where σ is a conductivity, we reach a dynamical equation for ϕ only,

$$(\partial_x^2 + \partial_y^2)\phi_l = (1 - \zeta\Delta_d)(\sin\phi_l + \beta\partial_t\phi_l + \partial_t^2\phi_l - j_{\text{bias}}), \tag{2.25}$$

which now describes the Josephson dynamics through coupled sine-Gordon equations, where β has been introduced as the damping constant $\beta = (\Phi_0/2\pi)\sigma/J_{c,0}D$. The quantity j_{bias} is the external current bias, normalised by the critical current density as $j_{\text{bias}} = I_{\text{bias}}/I_c$. Here $\zeta = (\lambda_{ab}/D)^2$ is a measure of the inductive coupling strength [74]. This derivation has been simplified and does not contain any capacitive coupling term, which is important for purely c-axis phase oscillations. The discussion of this will be delayed until the more complete model is presented in Chapter 4.

We can understand the dynamics of Eq. (2.25) by considering several limiting cases. In the absence of in-plane fluctuations and without inductive coupling ($\zeta = 0$), each pair of Cu-O planes behaves as a single Josephson junction with dynamics described precisely by the RCSJ model, as should be expected since there is no coupling between junctions in this limit. Including the in-plane dynamics with the $(\partial_x^2 + \partial_y^2)$ term, each pair of planes now behaves as a long junction described by the sine-Gordon equation

$$(\partial_x^2 + \partial_y^2)\phi_l = (\sin\phi_l + \beta\partial_t\phi_l + \partial_t^2\phi_l - j_{\text{bias}}).$$

With finite inductive coupling $\zeta > 0$ the dynamics of the intrinsic junctions become coupled. To see this more clearly, we can rearrange Eq. (2.25) to give

$$\partial_t^2\phi_l + \beta\partial_t\phi_l + \sin\phi_l - j_{\text{bias}} = \sum_k \left([1 - \zeta\Delta_d]^{-1}\right)_{lk}\left(\partial_x^2 + \partial_y^2\right)\phi_k.$$

When $\zeta = 0$, the matrix $\left([1 - \zeta\Delta_d]^{-1}\right)$ is diagonal and the RHS only contains terms having index l. When $\zeta > 0$, $\left([1 - \zeta\Delta_d]^{-1}\right)$ is no longer diagonal and inter-junction

coupling occurs. An additional point is that in this particular model, there is no coupling between modes having k_x, $k_y = 0$ since inductive coupling acts only through gradients in the phase. Specifically, if (k_x, $k_y = 0$), the RHS is also zero preventing inter-junction coupling. In the case of capacitive coupling, as in Chapter 4, additional terms cause a finite coupling even when $k_x, k_y = 0$.

2.2.2 In-plane dynamics

In addition to excitations of the Josephson phase, it is possible for thermal fluctuations to induce vortex formation in the 2D superfluid. Due to the higher in-plane phase stiffness, this is associated with higher energies than the Josephson fluctuations. In a superfluid described by a macroscopic wavefunction, as in Eq. (2.3), the superfluid velocity $\vec{v}$ is given by

$$\vec{v} = \frac{\hbar}{m_{\text{eff}}} \nabla \chi, \tag{2.26}$$

providing an irrotational flow. However, the phase is defined modulo 2π and a vortex is a localised region in which the line integral

$$\oint \chi dl = 2\pi \; n$$

around a closed loop is finite, with integer n. The wavefunction itself must be continuous, thus at the vortex core $\psi \to 0$ and the local pair density is depleted. This is a point (or line in 3D), and the phase winding causes flow round this point (line), hence the name "vortex".

As temperature is increased, the proliferation of these vortices ultimately destroys long-range phase order, and in strictly two dimensions is known as the Berezinsky-Kosterlitz-Thouless (BKT) transition. The XY model is often studied as the toy model of this universality class [11, 61, 75, 76]. In cuprates, the predictions of the XY model manifest as behaviour of the I-V characteristic [77], the frequency dependent conductivity [78], the Nernst signal [79], the nonlinear magnetisation [80] and the resistance [81]. With that said, the XY model predicts a universal jump in the superfluid density at T_c which experiments have failed to detect [82–86]. Strict 2D BKT behaviour only arises in the limit $\varsigma = \xi_{ab}/\xi_c \to \infty$. Additionally, in the cuprates, the true thermodynamic limit is never reached, since the correlation length ξ is bounded. For example, it can never exceed the physical dimensions of the sample. While the XY model may

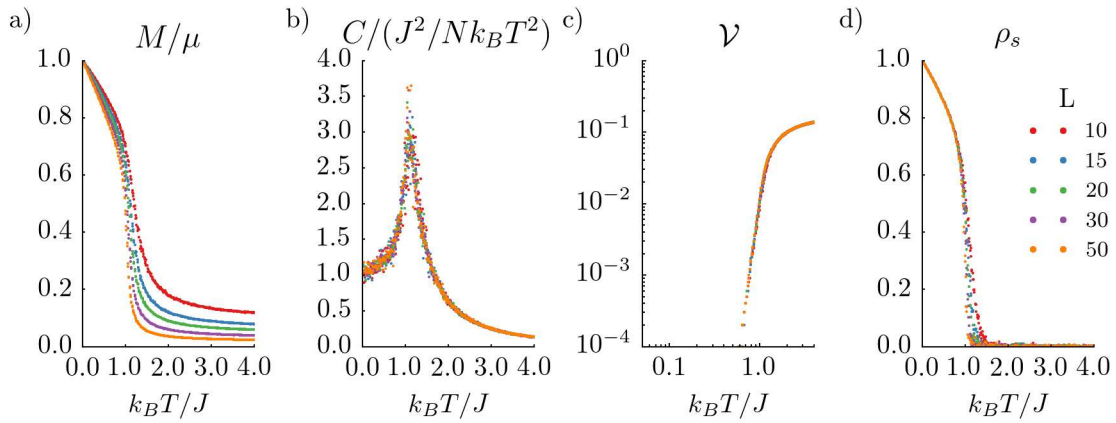

Figure 2.5: Behaviour of the 2D XY model Eq. (2.27), as calculated by the method of Gibbs sampling [89]. Quantities were computed on lattices with dimensions from $N = L^2 = 10 \times 10$ to 50×50 to indicate the scaling behaviour and the thermodynamic limit. Quantities were sampled every 100 Gibbs steps, include 5000 configurations, and exclude the initial burn-in period. (a) Magnetisation $M = (M_x^2 + M_y^2)^{1/2}$. As $L \to \infty$, we observe $M \to 0$ for $T > 0$. However, in the vicinity of $T = 0$, $M = 1 - \frac{k_BT}{8\pi J} \ln 2L^2$ [89], giving very slow convergence to the thermodynamic limit. (b) The specific heat C (defined in Eq. (2.29) shows a peak around $k_BT/J \sim 1$. (c) The vorticity $\mathcal{V}$ as defined in Eq. (2.31) becomes finite above the transition temperature T_{BKT}. (d) The superfluid density, as calculated by Eq. (2.30), approaches 0 near the transition. In the thermodynamic limit, this transition is sharp in 2D.

contain the correct universal features of the transition, its prediction of non-universal quantities can be improved by considering various modifications to the basic model. For example, Coulomb interactions can improve the agreement with c-axis superfluidity measurements [87], while increasing the vortex core energy can increase the temperature at which vortex-antivortex unbinding occurs to above that of 2D BKT predictions, in closer agreement with experimental measurements [88]. We take the view that the classical XY model captures the essential physics of the phase transition driven by (order parameter) phase fluctuations.

The classical XY model is described by the Hamiltonian

$$H_{\mathrm{XY}} = -J \sum_{\langle i,j \rangle} \cos(\chi_i - \chi_j), \tag{2.27}$$

where χ_i is the phase variable on site i, J is the coupling strength, and the sum runs over all pairs of nearest neighbours in a square lattice. In introducing this model we follow Ref. [89] where further details may be found. The anisotropic 3D extension to the XY model is then

$$H_{\mathrm{XY}}^{(3\mathrm{D})} = -\sum_{\langle i,j \rangle} J_{ij} \cos(\chi_i - \chi_j), \tag{2.28}$$

where J_{ij} is now direction- and potentially layer-dependent. Fig. 2.5 presents the key thermodynamic properties of the 2D XY model, calculated by Gibbs sampling [89]. In 2D, the domain consists of a lattice of phase angles $\{\chi_i\}$ with periodic boundary conditions. The magnetisation is defined as

$$M = \sqrt{M_x^2 + M_y^2},$$

with $M_x = \mu\langle \cos\chi_i \rangle$, $M_y = \mu\langle \sin\chi_i \rangle$, where μ is the relevant magnetic moment on each site. There is also the total energy, $E = \langle H \rangle$, the specific heat

$$C = \frac{1}{N k_B T^2}\Big(\langle H^2 \rangle - \langle H \rangle^2 \Big), \tag{2.29}$$

and the magnetic susceptibility

$$\mathcal{M} = \frac{N}{k_B T}\Big(\langle M^2 \rangle - \langle M \rangle^2 \Big),$$

in which $N = L^2$, the total number of spins. When studying the formation of vortices in the XY model, the superfluid density ρ_s and the vorticity $\mathcal{V}$ are extremely useful. It may be shown [89] that the free energies with and without a vortex are related according to

$$F_{\mathrm{vortex}} \approx F + \frac{N}{2}\rho_s m_{\mathrm{eff}} v^2,$$

for small superfluid velocities v (defined in Eq. (2.26)). This is a definition of the superfluid density ρ_s as the free energy cost of a vortex, and may be generalised to anisotropic models as

$$F_{\mathrm{vortex}} \approx F + \frac{N}{2} m_{\mathrm{eff}} (\rho_s^{(x)} v_x^2 + \rho_s^{(y)} v_y^2 + \rho_s^{(z)} v_z^2).$$

From this, we may express the components of ρ_s directly as e.g.

$$\rho_s^{(x)} = \frac{1}{N m_{\mathrm{eff}}} \frac{\partial^2}{\partial v_x^2} F_{\mathrm{vortex}}.$$

Starting from the partition function Z derived from Eq. (2.27), one may evaluate the above expression to reach [89]

$$\rho_s^{(x)} = \frac{J}{Nk_BT}\left[\left\langle\sum\sin(\chi_i-\chi_j)\right\rangle^2 - \left\langle\left(\sum\sin(\chi_i-\chi_j)\right)^2\right\rangle\right] + \frac{1}{N}\left\langle\sum\cos(\chi_i-\chi_j)\right\rangle. \tag{2.30}$$

All sums are performed over nearest-neighbours (i,j) along the x-direction[11]. The superfluid density ρ_s provides direct information on the difference in free energy between configurations with and without a vortex: if $\rho_s \to 0$, then vortices can form at no cost. The superfluid density also has components $\rho_s^{(y)}$ and (in 3D models) $\rho_s^{(z)}$, which allows for vortices of different orientations to have different energy costs. Finally, there is the vorticity $\mathcal{V}$, which we define as the mean number of vortices per plaquette as follows,

$$\mathcal{V} = \frac{1}{N}\sum_{i_1\ldots i_4}\Big(\|\chi_{i_1}-\chi_{i_2}\| + \|\chi_{i_2}-\chi_{i_3}\| + \|\chi_{i_3}-\chi_{i_4}\| + \|\chi_{i_4}-\chi_{i_1}\|\Big), \tag{2.31}$$

where the sites $i_1 \ldots i_4$ are ordered clockwise around a square plaquette. We define the notation $\|\Delta\chi\| = \mod(\Delta\chi+\pi, 2\pi)-\pi$, i.e. $\Delta\chi$ has a suitable multiple of 2π added such that it falls in the range $-\pi \le \|\Delta\chi\| < \pi$.

In Fig. 2.5, the quantities M, C, $\mathcal{V}$ and ρ_s are presented for a range of temperatures $0 \le T \le 4J$. The magnetisation $M \to 0$ as the lattice size $L \to \infty$ for $T > 0$. Below T_{BKT} the convergence is slow, with $M = 1 - \frac{T}{8\pi}\ln 2L^2$ in the vicinity of $T = 0$. There is also a peak in the heat capacity C near $k_BT/J = 1$, indicative of a phase transition there. Subfigures (c) and (d) more clearly explain the situation: passing T_{BKT}, the vorticity $\mathcal{V}$ becomes finite and rapidly levels off. Related to this, in (d) the superfluid density ρ_s is finite below T_{BKT} (indicating that the cost of vortex formation is finite) and tends to zero above T_{BKT} (vortices are now free to form). In Fig. 2.6 some example configurations at temperatures $k_BT/J = 0.1, 0.5, 1.5, 10.0$ are displayed on a 20×20 lattice. At $k_BT/J = 0.1$, the spins appear to be ordered. This is because the algebraically-decaying spin-spin correlations are not apparent on such a small lattice. At temperatures below but approaching T_{BKT}, occasional vortices occur as shown in the second panel. At higher temperatures, vortices occur freely and disrupt the spin-spin correlations over very short lengthscales.

[11] These differences in the spins along x only have arisen from the discrete x derivative taken for $\rho_s^{(x)}$.

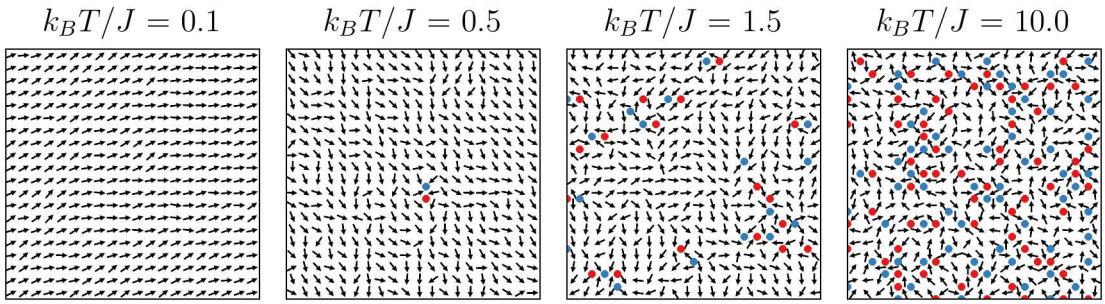

Figure 2.6: Individual configurations from the Gibbs sampling method used to produce the thermodynamic quantities of Fig. 2.5. These consider a periodic 20×20 lattice at temperatures in the range $k_BT = 0.1J \rightarrow 10.0J$, for the Hamiltonian Eq. (2.27). These are representative of the typical configurations of this system, being well after the burn-in period has expired. The cores of vortices and antivortices are marked in red and blue respectively. At the lowest temperatures, the phase is ordered over short lengthscales but decays algebraically giving $M = 0$ in the thermodynamic limit. At higher temperatures but still below T_{BKT}, bound vortex-antivortex pairs appear, but moderate-length correlations remain. Once above T_{BKT}, the proliferation of vortices annihilates phase coherence on all but the very shortest of lengthscales.

2.3 Coupling between the Josephson phase and electromagnetic fields

Treatments of the Josephson junction invariably make the assumption of a closed system, with no account for energy radiated due to oscillating electromagnetic fields. This approach is well-justified, since the severity of the impedance mismatch between the Josephson phase and external EM modes prevents any significant radiation from occurring. Damping is then dominated by internal quasiparticle tunnelling. However, several approaches have been taken in the literature to study the coupling of a Josephson junction, array of junctions, or cuprate crystal to electromagnetic modes, principally with an interest in developing a coherent THz source. In this section we provide a brief overview of these approaches, which will motivate the FEM calculations of Chapter 5.

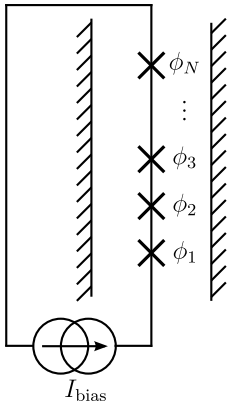

Figure 2.7: Schematic of the physical system studied in Almaas and Stroud [91]. There are N ideal Josephson junctions, indicated by crosses, each with a gauge-invariant phase difference ϕ_j. There are then $N+1$ superconducting islands connecting them. A current I_{bias} is driven through the array, which sits inside a cavity supporting a single mode of frequency Ω_c.

2.3.1 Junction array in a cavity

There is a series of papers [90–96] studying the placement of artificial Josephson junction arrays within cavity resonators, and the consequent physical phenomena. Of these papers, Ref. [91] provides the most useful discussion of the underlying model, as far as this thesis is concerned. We describe this model in detail to understand the precise assumptions upon which it is based. We take care to highlight all assumptions and approximations made.

The physical system under consideration is that shown in Fig. 2.7: an array of N Josephson junctions, each with a gauge-invariant phase ϕ_j, placed inside a single-mode cavity of frequency Ω_c. There are no further explicit assumptions regarding the arrangement of the Josephson array inside the cavity.

We start with the assumption that the full system (cavity plus Josephson junction) is described by the Hamiltonian

$$\hat{H} = \hat{H}_{\text{photon}} + \hat{H}_J + \hat{H}_C + \hat{H}_{\text{curr}} + \hat{H}_{\text{diss}}. \tag{2.32}$$

$\hat{H}_{\text{photon}}$ is the usual Hamiltonian for a single cavity mode,

$$\hat{H}_{\text{photon}} = \hbar\Omega_c \left(\hat{a}^\dagger \hat{a} + \frac{1}{2} \right), \tag{2.33}$$

with $\left[\hat{a}, \hat{a}^\dagger\right] = 1$. The ladder operators $\hat{a}$ and $\hat{a}^\dagger$ annihilate and create a photon in the cavity mode, respectively. $\hat{H}_J$ is the Josephson Hamiltonian, assumed[12] to take the form

$$\hat{H}_J = -\sum_{j=1}^{N} E_{Jj} \cos \hat{\phi}_j, \tag{2.34}$$

where E_{Jj} is the Josephson energy of the jth junction, and the operator $\hat{\phi}_j$ is the gauge-invariant phase difference across the jth junction, to be defined more precisely later (in Eq. (2.38)). The Josephson energy E_{Jj} is related to the junction's critical current I_{cj} via $E_{Jj} = \hbar I_{cj}/2e$.

The Hamiltonian $\hat{H}_C$ is the capacitive energy of the N junctions, which they approximate as

$$\hat{H}_C = \sum_{j=1}^{N} E_{Cj} \hat{n}_j^2, \tag{2.35}$$

where $E_{Cj} = (2e)^2/2C_j$ is the capacitive energy of the jth junction, C_j is its capacitance, and the operator $\hat{n}_j$ is the difference in number of Cooper pairs between the jth and $(j+1)$th superconducting island. The Hamiltonian $\hat{H}_{\text{curr}}$ incorporates a driving current,

$$\hat{H}_{\text{curr}} = -\frac{\hbar I_{\text{bias}}}{2e} \sum_{i=1}^{N} \hat{\phi}_j, \tag{2.36}$$

in which I is the external bias current. Thus the combination $\hat{H}_J + \hat{H}_C + \hat{H}_{\text{curr}}$ is conventionally referred to as the "Josephson Hamiltonian", as it accounts for the dynamics of the junction variables $\hat{\phi}_j$ and $\hat{n}_j$ when the junction is in isolation. Finally, $\hat{H}_{\text{diss}}$ incorporates dissipation in the Josephson array and is defined as

$$\hat{H}_{\text{diss}} = \sum_{\alpha} \left[f_{\alpha,j} \hat{\phi}_j \hat{u}_{\alpha,j} + \frac{\hat{p}_{\alpha,j}^2}{2m_{\alpha,j}} + \frac{1}{2} m_{\alpha,j} \omega_{\alpha,j}^2 \hat{u}_{\alpha,j}^2 + \frac{(f_{\alpha,j})^2}{2m_{\alpha,j}\omega_{\alpha,j}^2} (f_{\alpha,j})^2 \right]. \tag{2.37}$$

Here, each gauge-invariant phase difference $\hat{\phi}_j$ is coupled to a collection of harmonic oscillators: the variables $\hat{u}_{\alpha,j}$ and $\hat{p}_{\alpha,j}$ describe the αth oscillator in the jth junction and are canonically conjugate, satisfying the commutation relation $[\hat{u}_{\alpha,j}, \hat{p}_{\alpha',k}] = i\hbar\delta_{\alpha,\alpha'}\delta_{j,k}$.

[12] This assumption appears to be well-justified, as the Hamiltonian $\hat{H}_J + \hat{H}_C$ is that which results from directly quantising a single short junction. The resulting Heisenberg equations of motion for the expectation values are in agreement with the classical dynamics of this system. Furthermore, the use of the gauge-invariant phase is appropriate, since in the presence of electromagnetic fields, physically measurable quantities (such as the supercurrent through the junction) can only depend on gauge-invariant quantities such as $\hat{\phi}_j$.

The symbol $\delta_{j,k}$ is the Kronecker delta, and $f_{\alpha,j}$ gives the coupling strength between the the jth junction and the (α, j)th oscillator. The (constant) rightmost term is added to prevent this coupling shifting the potential of the jth junction. The effect of $\hat{H}_{\text{diss}}$ is to provide thermalisation for the junction variables $\hat{\phi}_j$ and $\hat{n}_j$. The harmonic oscillators are initialised in a thermal state, traced out, and the reduced system consisting of only Josephson and cavity coordinates is evolved in time. Over sufficient timescales, the Josephson coordinates behave as though thermalised.

Returning to the gauge-invariant phase, this is defined as

$$\phi_j = \Delta\chi_j - \frac{2\pi}{\Phi_0}\int_j \vec{A}\cdot\vec{dl} \equiv \Delta\chi_j - A_j, \tag{2.38}$$

in which $\Delta\chi_j$ is the phase difference across junction j in a particular gauge, $\vec{A}$ is the vector potential, $\Phi_0 = h/2e$ is the flux quantum, and the line integral is taken across the junction j. When considering Josephson junctions in the presence of electromagnetic fields, we should use the gauge-invariant phase ϕ_j throughout and only make use of $\Delta\chi_j$ if it offers a calculational convenience.

It is assumed that $\vec{A}$ arises due to the electromagnetic field of the cavity mode[13], and $\vec{A}$ may be written as[14]

$$\vec{A}(\vec{x},t) = \sqrt{\frac{h}{4\pi\epsilon_0\Omega_c}}\left(\hat{a}(t) + \hat{a}^\dagger(t)\right)\vec{\Psi}(\vec{x}). \tag{2.39}$$

The operators $\hat{a}(t)$ and $\hat{a}^\dagger(t)$ are the standard creation and annihilation operators for a quantum harmonic oscillator in the Heisenberg picture. The quantity $\vec{\Psi}(\vec{x})$ is proportional to the local electric field of the mode[15], normalised such that

$$\int_{\text{cav}} d^3x |\vec{\Psi}(\vec{x})|^2 = 1. \tag{2.40}$$

This form of $\vec{A}$ allows us to write $A_j = \sqrt{g_j}\left(\hat{a} + \hat{a}^\dagger\right)$, defining the coupling constant g_j as

$$g_j = \frac{\hbar c^2}{\Omega_c}\frac{2\pi^2\mu_0}{\Phi_0^2}\left(\int_j \vec{\Psi}\cdot\vec{dl}\right)^2,$$

[13]It is not possible to determine whether this assumption is justified without a more general treatment of the problem. Inside the junction, the electromagnetic fields (and thus vector potential) are due to both the cavity mode and the phase dynamics of the junction itself. Provided the junction is in the superconducting state, the electric fields associated with its dynamics should be minute and so the cavity contribution should dominate. However, this implicit division into "contributions" is not strictly valid and this assumption requires further investigation.

[14]This quantisation of the $\vec{A}$ field requires that we work in the Coulomb gauge: $\nabla\cdot\vec{A} = 0$.

[15]In Ref. [91], the quantity we call $\vec{\Psi}$ is confusingly labelled $\vec{E}$ (it is the normalised mode amplitude, rather than an electric field).

where the line integral is taken across the jth Josephson junction.

The full Hamiltonian has been specified, and the model is completed with the specification of the operator commutation relations. The Josephson operators for junctions j and k (in the absence of a cavity mode) $\Delta\hat{\chi}_j$ and $\hat{n}_k$ satisfy $[\Delta\hat{\chi}_j, \hat{n}_k] = i\delta_{jk}$, where δ_{jk} is the Kronecker delta. The phase $\Delta\hat{\chi}_j$ is position-like, and the number difference is momentum-like[16]. Additionally, due to the junction and the cavity being separate systems, we should write

$$\left[\{\hat{a}, \hat{a}^\dagger\}, \{\Delta\hat{\chi}, \hat{n}\}\right] = 0, \tag{2.41}$$

by which we mean that operators from the set $\{\hat{a}, \hat{a}^\dagger\}$ should commute with operators from the set $\{\Delta\hat{\chi}, \hat{n}\}$. Following Ref. [91], when the cavity mode is included we should keep these commutation relations and derive a commutation relation between the gauge-invariant phase $\hat{\phi}_j$ and the cavity operators $\hat{a}$, $\hat{a}^\dagger$. They define

$$\begin{aligned} \hat{a} &= \hat{a}_R + i\hat{a}_I, \\ \hat{a}^\dagger &= \hat{a}_R - i\hat{a}_I, \end{aligned} \tag{2.42}$$

in order that the gauge-invariant phase difference can be written as

$$\hat{\phi}_j = \Delta\hat{\chi}_j - 2\sqrt{g_j}\hat{a}_R \tag{2.43}$$

and the non-zero commutators between the junction and cavity operators are

$$\begin{aligned} \left[\hat{\phi}_j, \hat{a}_R\right] &= 0, \\ \left[\hat{\phi}_j, \hat{a}_I\right] &= -i\sqrt{g_j}. \end{aligned} \tag{2.44}$$

We now convert the Hamiltonian of this system into a form that explicitly gives the coupling between the cavity mode $\hat{a}$ and Josephson phases $\hat{\phi}_j$. Starting with

$$\hat{H} = \hbar\Omega_c\left(\hat{a}^\dagger\hat{a} + \tfrac{1}{2}\right) + \sum_j \left(-E_{Jj}\cos\hat{\phi}_j + E_{Cj}\hat{n}_j^2 - \frac{\hbar I_{\text{bias}}}{2e}\hat{\phi}_j\right), \tag{2.45}$$

we must separate this expression into commuting terms to describe the cavity and Josephson parts. Doing this yields $\hat{H} = \hat{H}_{\text{photon}} + \hat{H}_{\text{JJ}} + \hat{H}_{\text{int}}$, with

$$\begin{aligned} \hat{H}_{\text{photon}} &= \hbar\Omega_c\left(\hat{a}^\dagger\hat{a} + \tfrac{1}{2}\right), \\ \hat{H}_{\text{JJ}} &= \sum_j \left(-E_{Jj}\cos\Delta\hat{\chi}_j + E_{Cj}\hat{n}_j^2 - \frac{\hbar I_{\text{bias}}}{2e}\Delta\hat{\chi}_j\right), \\ \hat{H}_{\text{int}} &= \sum_j \left(E_{Jj}(\cos\Delta\hat{\chi}_j - \cos\hat{\phi}_j) + \frac{\hbar I_{\text{bias}}}{2e}(\Delta\hat{\chi}_j - \hat{\phi}_j)\right). \end{aligned} \tag{2.46}$$

[16]These commutators arise from canonical quantisation, and when taken with the Hamiltonian yield equations of motion for the operators which are consistent with the known classical model.

To linearise, we expand the Josephson phase as $\Delta\hat{\chi}_j = \Delta\chi_{j,0} + \delta\hat{\chi}_j$. The mean value $\Delta\chi_{j,0}$ corresponds to the steady-state Josephson phase which produces a supercurrent matching the applied bias, i.e. $\sin\Delta\chi_{j,0} = I_{\rm bias}/I_c$. We may then diagonalise $H_{\rm JJ}$ by introducing the operators $\hat{b}_j$ and $\hat{b}_j^\dagger$ defined by

$$\begin{aligned}\hat{b}_j &= \sqrt{\frac{E_{Jj}\cos\Delta\chi_{j,0}}{2\hbar\omega_p'}}\;\delta\hat{\chi}_j + i\sqrt{\frac{\hbar\omega_p'}{2E_{Jj}\cos\Delta\chi_{j,0}}}\;\hat{n},\\ \hat{b}_j^\dagger &= \sqrt{\frac{E_{Jj}\cos\Delta\chi_{j,0}}{2\hbar\omega_p'}}\;\delta\hat{\chi}_j - i\sqrt{\frac{\hbar\omega_p'}{2E_{Jj}\cos\Delta\chi_{j,0}}}\;\hat{n},\end{aligned} \tag{2.47}$$

where ω_p' is the effective (biased) Josephson plasma frequency given by $\hbar\omega_p' = (2E_{Cj}\times E_{Jj}\cos\Delta\chi_{j,0})^{1/2}$. The operators $\hat{b}_j$ and $\hat{b}_j^\dagger$ satisfy the commutation relation $\left[\hat{b}_j, \hat{b}_j^\dagger\right] = 1$. This yields

$$\begin{aligned}\hat{H}_{\rm JJ} &= \sum_j \hbar\omega_p'\left(\hat{b}_j^\dagger\hat{b}_j + \tfrac{1}{2}\right),\\ \hat{H}_{\rm int} &= -\tfrac{1}{2}\sum_j \sqrt{\hbar\omega_p'\; g_j E_{Jj}\cos\Delta\chi_{j,0}}\;\left(\hat{a}+\hat{a}^\dagger\right)\left(\hat{b}_j+\hat{b}_j^\dagger\right).\end{aligned} \tag{2.48}$$

This interaction $\hat{H}_{\rm int}$ depends on the cavity frequency Ω_c through $g_j \propto 1/\Omega_c$, and on the cavity mode volume implicitly via the normalisation Eq. (2.40).

We now discuss the model presented above, with regard to its suitability for modelling the coupling of the Josephson phase in cuprates to the external electromagnetic field. We should first note that this model is derived explicitly for an artificial Josephson junction array inserted into a cavity resonator. This has two important consequences, the first of which is that the Josephson junctions are independent and not directly coupled (as they would be in a cuprate). Secondly, the Josephson phase is coupled to the cavity mode with a strength independent of the junction dimensions, since the junction is implicitly assumed to be much smaller than the London penetration depth. External cavity fields may penetrate the junction completely and thus the coupling is independent of the physical dimensions, with all other parameters held constant.

The principal positive aspect of this model is its simple Hamiltonian form, allowing the use of the usual analytical and numerical machinery. However, the two shortcomings above must be rectified to produce a good model of a *cuprate* inserted in a cavity, particularly as the intrinsic Josephson junctions in a cuprate are always coupled. One could do this by adding ad-hoc terms to include the desired effects, however additional parameters will be introduced and must be assigned physical values. This

naturally leads on to the next section, in which we introduce a microscopic model for the Josephson junction and cuprate electrodynamics, including an explicit treatment of the junction edge where the coupling between the cavity mode and the Josephson phase occurs.

2.3.2 Electrodynamical approach

In contrast to the top-down approach of the previous section, Bulaevskii and Koshelev [36, 97, 98] take an alternative approach which directly addresses the issue of the coupling strength between an electromagnetic mode and the Josephson phase. At the heart of their calculation is the physical mechanism by which the coupling occurs: incident electromagnetic waves penetrate the superconductor, on the lengthscale of the penetration length. The electric component then drives the Josephson phase in the boundary region, which propagates along the junction.

In a single junction, the phase $\phi(x)$ is driven by local screening currents $J_{x\pm}$ and the magnetic field B_y, according to

$$\partial_x \phi = \frac{2\pi}{\Phi_0}\lambda_{ab}^2 \mu_0 \left[J_{x+} - J_{x-}\right] - \frac{2\pi D}{\Phi_0} B_y. \tag{2.49}$$

In turn, the magnetic field (in frequency-domain) obeys a Helmholtz equation,

$$\left(\partial_x^2 + \partial_y^2\right) B_y(\omega) - \frac{B_y(\omega)}{\lambda_\omega^2} = \frac{\Phi_0}{2\pi\lambda_{ab}^2}\frac{\partial\phi(x,\omega)}{\partial x}\delta(z), \tag{2.50}$$

where $\lambda_\omega^{-2} = 1/\lambda_{ab}^2 - \epsilon_s\omega^2/c^2 - i\omega\sigma_q/\epsilon_0 c^2$, λ_{ab} is the ab-plane London penetration depth, ϵ_s is an effective dielectric constant of the superconductor, and σ_q is the contribution to the conductivity due to dissipative currents in the superconductor. From the right-hand side, we note that the magnetic field near the junction is driven by gradients in the phase $\phi(x,\omega)$. By eliminating the magnetic field, we can derive a (non-local) equation for the phase dynamics, as

$$\left(\frac{\omega^2}{\omega_p^2} + \alpha_t\frac{i\omega}{\omega_p}\right)\phi(x) + \frac{\lambda_J^2}{\pi\lambda_{ab}}\int_{-\infty}^{0} dx'\ \partial_x\left[K_0\left(\frac{x-x'}{\lambda_\omega}\right) + K_0\left(\frac{x+x'}{\lambda_\omega}\right)\right]\partial_{x'}\phi(x') - \frac{1}{\mu_0 J_c}\partial_x B_b(x,0) = s_\omega(x), \tag{2.51}$$

in which $\alpha_t = (\Phi_0/2\pi)(\omega_p\sigma_t/J_c D)$ is the dissipation due to quasiparticle tunnelling, $\lambda_J^2 = \Phi_0/2\pi\mu_0 J_c(2\lambda_{ab} + D)$ is the Josephson lengthscale, $K_0(x)$ is the modified Bessel

function, $B_b(x,0)$ is the magnetic field at the edge of the junction ($x = 0$) and $s_\omega(x)$ is the amplitude of the Josephson current in the Fourier domain, as $\mathrm{Re}(s_\omega(x)e^{-i\omega t}) = \sin\phi(x,t)$. The nonlocality in the Josephson phase dynamics has arisen from the elimination of the magnetic field; the physical description in terms of electromagnetic fields and the Josephson phase is of course local.

Their analysis proceeds to derive an expression for the boundary condition, connecting the phase inside the junction with the magnetic field B_y just outside. They reach

$$\partial_x\phi(0) \approx -\frac{\lambda_{ab}}{\lambda_\omega}\frac{4\pi\lambda_{ab}}{\Phi_0}B_y(\omega, \vec{x} = 0). \tag{2.52}$$

By making further assumptions about the boundary conditions on the electromagnetic field far from the junction, they are able to derive expressions for the impedance mismatch between the junction and free space, and for the power radiated by Josephson oscillations. Conversely, it is possible to reverse this approach and ask what phase oscillations will be induced due to external driving. By construction, the geometries considered are sufficiently simple for an analytical solution. We, on the other hand, are more interested in less geometrically trivial THz cavity configurations designed specifically to minimise the cavity mode volume, and thus maximise the coupling. The approach of Bulaevskii and Koshelev inspires our work in Chapter 5, where the finite element method is brought to bear on this problem, in order that we may numerically estimate coupling strengths and develop an effective two-oscillator model for the coupled Josephson-cavity system.

2.4 Summary

This chapter has covered the background material on superconductivity and Josephson junctions. This included the Ginzburg-Landau and Bardeen-Cooper-Schrieffer theories of conventional superconductors, using the Ginzburg-Landau theory description to understand the core physics of the Josephson effect. High-temperature superconductors were introduced through anisotropic Ginzburg-Landau descriptions, in particular the cuprates. We introduced the effective model of these materials as stacked Josephson junctions, and finally reviewed the two main treatments in the literature of the coupling between the Josephson phase in cuprates and external electromagnetic modes. The Josephson stack model is central to our work on parametric cooling presented in

Chapter 4. Finally, in Chapter 5 we will extend the results of Bulaevskii and Koshelev [36] and infer Josephson-cavity coupling strengths for more realistic geometries.

3

Laser cooling methods

The field of laser cooling is vast, with the broad goal of lowering the temperature of systems (typically simple or small) by the application of laser radiation. To date, the classes of systems to which laser cooling has been successfully applied include ions [99], neutral atoms [100, 101], molecules [101], optomechanical systems [102, 103] and now more complex systems such as specifically engineered solids [20] and semiconductors [104]. In each case, a process is identified and engineered such that when driven by high-intensity radiation, quanta may be pumped out of the system. This chapter covers the necessary background on laser cooling as relevant for its possible application to cuprates. Sec. 3.1 begins with a cooling scheme for an optomechanical oscillator. This emphasises the physics of cooling, and furthermore the Hamiltonian description of this system is similar to that used by Hammer, Aprili, and Petković [34] for cooling an artificial Josephson junction, outlined in Sec. 3.2. In Sec. 3.3 we describe the basis of the parametric cooling scheme, which in Chapter 4 will be implemented in a bilayer cuprate. The reviews [17, 105–109] provide a more thorough background of the experiments and theory.

3.1 Cavity cooling of an optomechanical oscillator

As an introduction to the physics of laser cooling, in this section we discuss the physical mechanism of cavity cooling of an optomechanical oscillator. Optomechanical laser cooling was first demonstrated in the microwave [110] and subsequently optical regimes [111]. Also, other systems such as embedded quantum dots [112] and Josephson qubits [113] have been exploited to play the role of the cavity, and enable the ground state

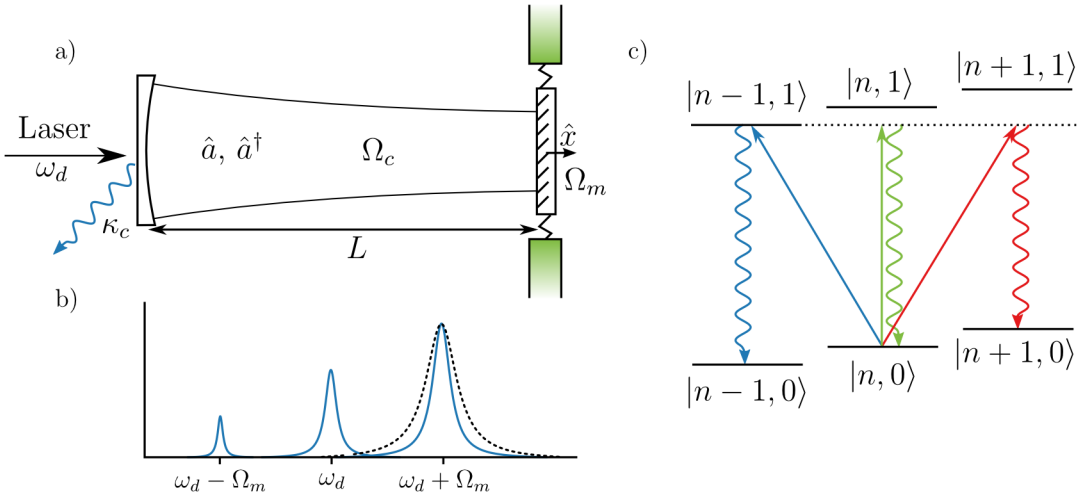

Figure 3.1: (a) Schematic of a simple optomechanical system consisting of a single-mode cavity with frequency Ω_c in which one mirror is mounted on a spring having frequency Ω_m. The cavity is driven by a laser at frequency ω_d. (b) In addition to the response at ω_d, the mirror motion creates sidebands due to the Doppler effect at $\omega_d \pm \Omega_m$ inside the cavity. Here, the cavity frequency Ω_c is on resonance with the upper sideband. The interaction enables photons at ω_d and phonons at Ω_m to jointly excite the cavity, which then decays through the fixed mirror at rate κ_c. (c) Energy level diagram in which the state $|n,m\rangle$ has n quanta in the mechanical motion and m in the cavity. The figure depicts three scattering processes which can occur when driving at the frequency $\omega_d = \Omega_c - \Omega_m$ (as in (b)). The transition $|n,0\rangle \rightarrow |n-1,1\rangle$ is resonant and proceeds at the greatest rate, while the other transitions are off-resonant, indicated in green and red. A vertical transition occurs when the cavity emits a photon. The system repeatedly transitions downwards along this ladder, cooling the oscillator.

cooling of nanomechanical oscillators. Regarding cavity schemes, the resolved sideband regime was first achieved experimentally by Schliesser et al. [114]. This latter system provides a simple model for cooling a single oscillator[1], and is thus relevant conceptually for the laser cooling of the Josephson phase as developed in this thesis. Additionally, there is a direct mathematical analogy with the Josephson sideband scheme [34], to be discussed in the next section.

[1]Compare this with Doppler cooling, in which the kinetic energy of particles is reduced by the scattering of light. The particle provides a scattering coupling between a single mode (that of the driving laser) and the continuum of free space modes, with each scattering event on average reducing the particle's energy.

A simple optomechanical setup is depicted in Fig. 3.1(a), in which two mirrors form an optical cavity, with one mirror being mounted on a spring and so having a motional degree of freedom. Let the optical cavity have frequency Ω_c, decay rate κ_c and length L_c. The optical cavity mode creation and annihilation operators $\hat{a}^\dagger$ and $\hat{a}$ satisfy the commutation relation $\left[\hat{a}, \hat{a}^\dagger\right] = 1$, and describe the processes of creating and annihilating a photon in the cavity, respectively. The mirror has a displacement $\hat{x}$ from equilibrium, momentum $\hat{p}$, frequency Ω_m, damping Γ_m and mass m. These degrees of freedom are coupled; the radiation pressure in the cavity exerts a force $(\hbar\Omega_c/L_c)\hat{a}^\dagger\hat{a}$ on the mirror, whose motion alters the cavity length L_c and thus the mode structure. Rigorously quantising this system is not trivial owing to the dynamic boundary conditions of the electromagnetic mode. This problem is addressed in detail by Law [115]; physical intuition leads to the same theoretical description. It suffices to describe the system with the Hamiltonian

$$\hat{H} = \hbar\omega(\hat{x})\hat{a}^\dagger\hat{a} + \frac{\hat{p}^2}{2m} + \tfrac{1}{2}m\Omega_m^2\hat{x}^2. \tag{3.1}$$

This Hamiltonian is non-trivial, since the cavity frequency ω depends on the oscillator coordinate $\hat{x}$. The cavity round-trip time $2L_c/c \ll 1/\Omega_m$, indicating that the cavity mode should adiabatically follow the mirror motion. With this approximation, the cavity frequency $\omega(\hat{x})$ is given by

$$\omega(\hat{x}) = \Omega_c\left(1 - \frac{\hat{x}}{L_c}\right), \tag{3.2}$$

for $\langle\hat{x}\rangle/L_c \ll 1$. Then we can write

$$\hat{H} = \hbar\Omega_c\hat{a}^\dagger\hat{a} + \frac{\hat{p}^2}{2m} + \tfrac{1}{2}m\Omega_m^2\hat{x}^2 - \hbar g_0\hat{a}^\dagger\hat{a}\left(\hat{b} + \hat{b}^\dagger\right), \tag{3.3}$$

with the intrinsic coupling strength $g_0 = \sqrt{\hbar/2m\Omega_m}(\Omega_c/L_c)$, and $\hat{b} = \sqrt{m\Omega_m/2\hbar}\,(\hat{x} + i\hat{p}/m\Omega_m)$ having been introduced as the annihilation operator for the mechanical mode. The operators $\hat{b}$ and $\hat{b}^\dagger$ satisfy the commutation relation $\left[\hat{b}, \hat{b}^\dagger\right] = 1$ and represent the annihilation and creation of a phonon in the mechanical mode, respectively. From this point onwards, there is nothing "unusual" about the ladder operators $\hat{a}$ and $\hat{b}$.

Thermodynamically, energy must be provided to drive a cooling process and so we add the cavity driving term

$$\hat{H}_{\mathrm{dr}} = i\hbar\sqrt{\kappa_{\mathrm{ex}}}\left(\alpha_{\mathrm{in}}^*\hat{a}e^{i\omega_d t} + \alpha_{\mathrm{in}}\hat{a}^\dagger e^{-i\omega_d t}\right),$$

where $\alpha_{\rm in}$ has been introduced as the driving strength, $\kappa_{\rm ex}$ is a loss rate associated with the input coupling, and t is the time variable. The steady state of a driven, damped harmonic oscillator is a coherent state. We can remove the time dependence of the driving term by moving to a rotating frame at ω_d, this is achieved by transforming $\hat{H}$ with the unitary $\hat{U} = \exp\left(i\omega_d t\ \hat{a}^\dagger\hat{a}\right)$ which yields the transformed Hamiltonian $\tilde{H}$, given by

$$\tilde{H} = -\hbar\Delta_c\hat{a}^\dagger\hat{a} + \frac{\hat{p}^2}{2m} + \tfrac{1}{2}m\Omega_m^2\hat{x}^2 - \hbar g_0\hat{a}^\dagger\hat{a}\left(\hat{b}+\hat{b}^\dagger\right) + i\hbar\sqrt{\kappa_{\rm ex}}\left(\alpha_{\rm in}^*\hat{a} + \alpha_{\rm in}\hat{a}^\dagger\right), \quad (3.4)$$

in which the detuning Δ_c is given by $\Delta_c = \omega_d - \Omega_c$ (i.e. the detuning of the driving relative to the cavity resonance). The form of the radiation pressure coupling, $\hat{a}^\dagger\hat{a}(\hat{b}+\hat{b}^\dagger)$ prevents the transformation by $\hat{U}$ introducing time dependence on this term. To consider fluctuations about this driven equilibrium, we denote the mean $\bar{\alpha} = \langle\hat{a}\rangle$ and write

$$\hat{a} = \bar{\alpha} + \delta\hat{a}. \quad (3.5)$$

We use this to linearise Eq. (3.4), neglecting terms $\mathcal{O}(\delta\hat{a}^2)$ in the interaction. These are the lowest order terms in $|\bar{\alpha}|^{-1} \ll 1$. We drop two constant terms in $\tilde{H}$, and additionally the linear terms in $(\delta\hat{a} + \delta\hat{a}^\dagger)$ cancel when the steady state $\bar{\alpha}$ satisfies $\bar{\alpha}\Delta_c = i\hbar\sqrt{\kappa_{\rm ex}}\alpha_{\rm in}$. This yields

$$\tilde{H} = -\hbar\Delta_c\delta\hat{a}^\dagger\delta\hat{a} + \hbar\Omega_m\hat{b}^\dagger\hat{b} - \hbar g_0\bar{\alpha}\left(\delta\hat{a}^\dagger + \delta\hat{a}\right)\left(\hat{b}+\hat{b}^\dagger\right), \quad (3.6)$$

where $\bar{\alpha}$ is taken to be real for convenience. In this rotating frame, we have reached a pair of harmonic oscillators with linear coupling of strength $g = g_0\bar{\alpha}$. These effective oscillators will be brought to resonance if the detuning $\Delta_c = -\Omega_m$. The interaction term enables energy transfer between the oscillators, and may be enhanced by increased occupation $\bar{\alpha} = \sqrt{\langle\hat{a}^\dagger\hat{a}\rangle}$ of the (original) cavity mode. It is essential to appreciate that the $\delta\hat{a}$ mode represents the fluctuations about the cavity coherent state, in a frame rotating at ω_d. As such, in the full description it is coupled to a thermal bath at optical frequencies near ω_d, and can be considered as unpopulated at relevant temperatures.

We can understand the dynamics of the system better by reverting to the classical regime. This will give a picture of the sideband structure, and the role played by the cavity. Dynamically, the mirror obeys a classical equation of motion

$$m\ddot{x}(t) + m\Gamma_m\dot{x}(t) + m\Omega_m^2 x(t) = F_{\rm rad}(t), \quad (3.7)$$

where it is driven by the radiation pressure force $F_{\rm rad} = \hbar\Omega_c|\bar{\alpha}^2|/L_c$. In a frame rotating at ω_d, the classical mode amplitude $\alpha(t) = \langle\hat{a}\rangle$ has dynamics [17]

$$\dot{\alpha}(t) = -\frac{\kappa_c}{2}\alpha + i(\Delta_c + \Omega_c x/L_c)\alpha + \sqrt{\kappa_{\rm ex}}\alpha_{\rm in}. \tag{3.8}$$

The term $\sqrt{\kappa_{\rm ex}}\alpha_{\rm in}$ describes the external driving, and the balance with the decay $-\frac{1}{2}\kappa_c\alpha$ determines the steady state. The phase drifts due to the detuning Δ_c as well as any instantaneous phase shift arising from the mirror position x. The steady (driven) state with $\dot{x} = 0$ is described by

$$\alpha(t) = \bar{\alpha} = \frac{\sqrt{\kappa_{\rm ex}}}{-i(\Delta_c + \Omega_c\bar{x}/L_c) + \frac{\kappa_c}{2}}\alpha_{\rm in}. \tag{3.9}$$

As expected, the cavity response $|\alpha|^2$ is a Lorentzian about the zero detuning $(\Delta_c + \Omega_c\bar{x}/L_c) = 0$ (in subsequent equations we redefine $\Delta_c + \Omega_c\bar{x}/L_c \to \Delta_c$ such that Δ_c gives the "true" detuning.) However, when the mirror is assumed to oscillate as $x(t) = \bar{x} + \delta x\cos(\Omega_m t)$, the cavity follows [109]

$$\alpha(t) = \bar{\alpha} + \frac{i\Omega_c}{2L_c}\bar{\alpha}\delta x\left(\frac{\exp(i\Omega_m t)}{-i(\Delta_c - \Omega_m) + \frac{\kappa_c}{2}} + \frac{\exp(-i\Omega_m t)}{-i(\Delta_c + \Omega_m) + \frac{\kappa_c}{2}}\right). \tag{3.10}$$

Thus the mirror motion creates a pair of sidebands at $\omega_d \pm \Omega_m$ which in analogy with Raman spectroscopy (and in a quantum picture) are known as Stokes and anti-Stokes processes. The process at $\omega_d \approx \Omega_c - \Omega_m$ corresponds to a photon at ω_d combining with a phonon of the oscillator to excite the cavity at Ω_c. Likewise, the process at $\omega_d \approx \Omega_c + \Omega_m$ corresponds to the cavity and mechanical mode being simultaneously excited. In Fig. 3.1(c) these processes are depicted, with the driving detuned to favour the cooling process. As Eq. (3.10) shows, with sufficiently low cavity damping κ_c and appropriate detuning, it is possible for one sideband to be substantially stronger than the other. This is precisely the manner in which the presence of the cavity strongly enhances the process, and enables the cooling (or heating) to proceed at a significant rate.

We observe that in this system, the nonlinearity of the original interaction Eq. (3.3) is essential for the existence of the sidebands. It is also convenient in that it provides a means to enhance the linearised coupling strength, which assists the cooling rate. At a more abstract level, the nonlinearity in Eq. (3.3) provides a route by which phonons at Ω_m may be dissipated into the bath of the optical mode at Ω_c. This is achieved via upconversion of the phonons, and is in general a necessary component of

any cooling scheme. In the absence of driving, the fluctuations in the mirror mode are in thermal equilibrium with their environment at temperature T. The upconversion process connects these fluctuations with a bath at Ω_c, a much higher frequency, and in the case of optical frequencies the bath modes are virtually unexcited. Quanta may then be transferred into the bath modes with no reheating back to the oscillator.

This particular optomechanical scheme operates in the *resolved sideband* regime[2], in which ground state cooling may be attained [17]. Another way of understanding the process is to observe that the cavity frequency $\Omega_c \gg \Omega_m$, and so the mode amplitude $\alpha(t)$ can track the mirror motion adiabatically. In the resolved sideband regime $\kappa_c \ll \Omega_m$, the cavity decay rate is such that the cavity mode intensity can no longer track the mirror and lags behind. In fact, this cavity "memory" is a general mechanism by which cooling may be achieved [116]. As an example, consider a test particle following a trajectory $X(t)$. A force $F(x, v, X(t))$ which depends on a particle's position x, velocity v and trajectory $X(t)$ is assumed to take the form

$$F(x, v, X(t)) = \int_0^\infty F(x, 0, X(t - t'))M(t')dt', \tag{3.11}$$

i.e. the force only depends explicitly on the particle's position, but at all times into its past weighted by the memory kernel $M(t)$. Expanding the force about t in powers of t', we find

$$\begin{aligned} F(x, 0, X(t - t')) &= F(x, 0, X(t)) + (X(t - t') - X(t)) \left.\frac{\partial F}{\partial X}\right|_{X=X(t)} + \mathcal{O}(t'^2) \\ &= F(x, 0, X(t)) - t'v(t) \left.\frac{\partial F}{\partial X}\right|_{X=X(t)} + \mathcal{O}(t'^2), \end{aligned}$$

in which we have identified the velocity $v(t) = \left.\frac{\partial X(\tau)}{\partial \tau}\right|_{\tau=t}$. In making this expansion we are assuming that the kernel $M(t)$ decays sufficiently rapidly with increasing t. We may write the original v-dependent form as

$$F(x, v, X(t)) = F(x, 0, X(t)) - v(t)T \left.\frac{\partial}{\partial X} F(x, 0, X)\right|_{X=X(t)}. \tag{3.12}$$

in which we have simplified by normalising the memory function as $\int_0^\infty dt M(t) = 1$, and identifying the memory timescale $T = \int_0^\infty dt'\ t'M(t')$. We see that a manifestly

[2]Intuitively, the resolved sideband regime corresponds to choosing parameters such that the sidebands in Fig. 3.1 may be individually resolved as opposed to comprising a single, broad peak. The sideband width is predominantly set by the cavity decay rate κ_c, while the separation is given by the mechanical frequency Ω_m. The resolved sideband regime is then achieved if $\kappa_c \ll \Omega_m$.

x-dependent force having memory of the particle's trajectory may be re-expressed as a memoryless but velocity-dependent force, with the v-dependent term growing the further back in time the memory extends (when the distribution of $M(t)$ is shifted to higher values of t). This can then be considered as a driving-induced friction, but without the corresponding stochastic forcing term. Consequently there is an additional dissipation channel. In the context of the optomechanical system, a lower decay rate κ_c enhances the cavity's memory of the mirror trajectory and increases the cooling rate[3].

3.2 Josephson sideband scheme

Turning to the system of an artificial Josephson junction, Hammer, Aprili, and Petković [34] argue that two intrinsic modes form a system analogous to the optomechanical system described in the previous section. They experimentally demonstrate that such laser cooling techniques may be successfully applied to reduce the Josephson fluctuations of a Nb/Al/Al_2O_3/PdNi/Nb junction, observed as a 0.3% increase in the mean switching current when the apparatus is cooled to ~ 2 K. In this section we discuss their theory and the analogy with the optomechanical system, and introduce the switching current measurement used to characterise the temperature of the Josephson phase.

The dynamics of the Josephson phase $\phi(x,t)$ in a long junction of length L may be formulated with the Hamiltonian [117]

$$H = E_J \int_0^L \frac{dx}{L}\left[\frac{1}{2\omega_{p,0}^2}(\partial_t\phi)^2 + \frac{\lambda_J^2}{2}(\partial_x\phi)^2 + 1 - \cos\phi - j_{\text{bias}}\phi\right], \tag{3.13}$$

in which E_J is the Josephson energy scale $\hbar I_c/2e$, λ_J is the Josephson penetration depth, $j_{\text{bias}} = I_{\text{bias}}/I_c$, $\omega_{p,0}$ is the plasmon frequency, I_c is the critical current and I_{bias} is the applied bias current. This gives the dynamics of the Josephson phase alone since the electric and magnetic field dynamics have been integrated out. The field $\phi(x,t)$ is expanded via the ansatz

$$\phi(x,t) = \chi(t) + \sum_n Q_n(t)\cos k_n x, \tag{3.14}$$

which satisfies Neumann boundary conditions [98]. In the experiment [34], the Josephson plasmon is at 550 MHz and the first harmonic Q_1 is at 7 GHz. Since the experiment

[3]Note that this is the first-order effect. The cooling mechanism relies on the cavity having a finite decay rate κ_c in order to dissipate energy, and so we should expect there to be an optimum κ_{opt} for cooling, with the cooling tending to zero once κ_c is decreased below κ_{opt}.

is performed at 2 K where $k_B T/h \sim 40$ GHz, we can make the approximation that the frequencies of the modes $Q_n(t)$ are high enough that none are significantly thermally populated[4], i.e. $\langle Q_n^2 \rangle \sim 0$. We will only consider the dynamics of the lowest mode Q_1 and obtain its coupling with the centre-of-mass mode χ. Then Eq. (3.13) becomes

$$H = E_J \left[\frac{1}{2\omega_{p,0}^2} \dot{\chi}^2 + \frac{1}{4\omega_{p,0}^2} \dot{Q}_1^2 + \frac{\lambda_J^2 k_1^2}{4} Q_1^2 - \left(1 - \frac{1}{4} Q_1^2\right) \cos\chi - j_{\text{bias}} \chi \right], \tag{3.15}$$

after expanding to quadratic order in Q_1. The normalised bias current j_{bias} requires a non-zero time-averaged Josephson phase which we will denote as $\bar{\chi}$, and which satisfies $\sin\bar{\chi} = j_{\text{bias}}$ in the absence of the Q_1 mode. If we also expand in $\delta\chi = \chi - \bar{\chi}$ to quadratic order, we can separate the Hamiltonian into $H = H_\chi + H_{Q_1} + H_{\text{int}}$, where

$$\begin{aligned} H_\chi &= E_J \left(\frac{1}{2\omega_{p,0}^2} \dot{\chi}^2 + \tfrac{1}{2} \cos\bar{\chi}\ \delta\chi^2 \right), \\ H_{Q_1} &= E_J \left(\frac{1}{4\omega_{p,0}^2} \dot{Q}_1^2 + \frac{\lambda_J^2 k_1^2 + \cos\bar{\chi}}{4} Q_1^2 \right), \\ H_{\text{int}} &= \tfrac{1}{4} j_{\text{bias}} E_J \delta\chi Q_1^2 - \tfrac{1}{8} E_J \delta\chi^2 Q_1^2. \end{aligned} \tag{3.16}$$

In the presence of bias, we have $\delta\chi Q_1^2$ coupling which is essentially identical to the $\hat{a}^\dagger \hat{a}(\hat{b} + \hat{b}^\dagger)$ coupling of Eq. (3.3). We can identify the centre-of-mass mode χ with the optomechanical displacement $\hat{x}$, and the first harmonic Q_1 with the cavity mode $\hat{a}$. The same theoretical analysis applies, and the Stokes and anti-Stokes sidebands are clearly observed in this system. The ansatz coordinates Eq. (3.14) are linearised normal modes of the system, and so the anharmonicity of the washboard potential induces a coupling term between them. This can be compared with the optomechanical case. The magnitude of Q_1 is limited by the restriction on ϕ, namely that the variation in ϕ, $\sqrt{\langle\phi^2\rangle - \langle\phi\rangle^2} \lesssim 2\pi$ in the superconducting state and so Q_1 cannot be driven arbitrarily in contrast to the cavity occupation α. The lowest-order coupling term requires finite bias j_{bias}, but this is also restricted as $|j_{\text{bias}}| \leq 1$. These two considerations restrict the strength of the coupling term. Additionally, it is harder to reach a scenario in which the cavity modes are accessible but also not thermally occupied. The Q_1 mode frequencies are set by the sample dimensions, with the experiment [34] making use of a $(740\ \mu\text{m})^2$ junction. Smaller junctions give higher frequencies, but are potentially more challenging experimentally. In the context of cuprates, the superconducting gap energy scale sets an upper limit on the frequencies available.

[4] At $T = 2$ K, a 550 MHz oscillator has population $n \sim 75$, while a 7 GHz oscillator has only $n \sim 5$. While this approximation neglects the small thermal population in the Q_1 mode, this has only a small quantitative effect on the χ mode dynamics.

In order to demonstrate that the Josephson phase has been cooled, the authors of Ref. [34] make use of the switching current distribution. The effect of thermal fluctuations is to cause the Josephson phase to slip down the washboard potential at a lower bias current than the theoretical maximum. In the washboard picture, the particle oscillates in the well at a frequency

$$\omega_p(j_{\text{bias}}) = \omega_{p,0}\left(1 - j_{\text{bias}}^2\right)^{1/4}.$$

On each oscillation, it has a probability $P = \exp\left[-\Delta U(j_{\text{bias}})/k_B T\right]$ of escaping the well and switching the junction state. The barrier height can be well approximated by [41]

$$\Delta U(j_{\text{bias}}) \approx 2E_J\left(1 - j_{\text{bias}}\right)^{3/2}.$$

The resulting suppression of the effective critical current is [41]

$$\langle I_c(T)\rangle = I_c(T=0)\left\{1 - \left[\frac{k_B T}{2E_J}\ln\frac{\omega_{p,0}\Delta t}{2\pi}\right]^{2/3}\right\}. \tag{3.17}$$

The bias sweep time Δt should be large enough that $\omega_{p,0}\Delta t \gg 1$, so that the dependence of the distribution on Δt becomes weak.

Experimentally, a measurement of the switching current entails starting at zero bias with the junction in the superconducting state ($V = 0$). The bias current is linearly ramped in a time Δt until a finite voltage V is detected across the junction, corresponding to the resistive phase-slipping state. The time (and therefore current) at which the slip occurred is recorded, and the bias current is then immediately reset to zero to prevent heating of the junction. This procedure is automatically repeated several thousand times to reconstruct the switching current distribution. In the experiment, this procedure is slightly simplified by the use of a 77 Hz sawtooth ramp for the bias. This is because at their temperatures the slipping distribution is concentrated close to $j_{\text{bias}} \sim 1$, and so negligible heating will occur between the phase slip and the current reset. The slipping distributions of the thermal and driven scenarios may then be compared. The driven scenario entails applying an additional AC bias term resonant with the Q_1 mode or its sidebands.

To conclude this section, the experiment of Hammer, Aprili, and Petković [34] employs a cooling scheme formally equivalent to that of resolved sideband cooling in optomechanical systems, yet there are a number of differences. The mechanical oscillators span Hz – GHz frequencies, potentially comparable with the Josephson resonance,

however the optical cavity is $\sim 10^{15}$ Hz, far higher than the 7 GHz Q_1 mode. In superconducting systems there is an upper bound on the frequencies available as radiation above the superconducting gap will break pairs and degrade the superconducting state. The dissipation route also differs, as the optical cavity is external to the mechanical oscillator. The Q_1 mode is part of an ansatz for the long junction and shares a thermal bath with the χ mode. Thus energy dissipated from the Q_1 mode does not leave the material, and in the absence of cryogenic cooling would gradually heat the χ mode.

3.3 Parametric cooling

In this final section, we introduce parametric cooling. We will see that this is mathematically equivalent to the previous schemes (after linearisation), but relies on different properties of the coupling. Historically, parametric cooling appears to be first proposed for cooling the slow, circular magnetron motion of a charged particle in a Penning trap [118]. The magnetron motion refers to the radius at which the particle orbits the centre of the trap, and should be minimised for precision spectroscopy. The magnetron and axial motions are linearly coupled, with the axial motion spring stiffness being set by trap parameters and therefore may be varied[5].

We consider a system of two harmonic oscillators l and h, having ladder operators $\hat{a}$ and $\hat{b}$ and with a time-dependent coupling $\kappa(t)$,

$$\hat{H} = \hbar\omega_l \hat{a}^\dagger \hat{a} + \hbar\omega_h \hat{b}^\dagger \hat{b} + \hbar\left[\kappa(t)\hat{a}\hat{b}^\dagger + \kappa^*(t)\hat{a}^\dagger \hat{b}\right]. \tag{3.18}$$

The coupling $\kappa(t)$ is assumed to have the form $\kappa(t) = \kappa_0 \exp(i\omega_d t)$, and the rotating wave approximation has been made. We first note that there is a simple and relevant thermodynamic cooling limit due to Wineland and Itano [14]. When this system absorbs a quantum of energy $\hbar(\omega_h - \omega_l)$ from the parametric modulation, a heat $\Delta Q_h = \hbar\omega_h$ is added to the h mode, and likewise a heat $\Delta Q_l = -\hbar\omega_l$ is added to the l mode. The total entropy change occurring with this process is $\Delta S = \frac{\Delta Q_l}{T_l} + \frac{\Delta Q_h}{T_h}$. Assuming cooling proceeds and encounters no other limits, it will do so until a reversible cycle is reached with $\Delta S = 0$. This implies the relationship

$$\frac{T_l}{T_h} = \frac{\omega_l}{\omega_h} \tag{3.19}$$

[5] An interesting aside is that in this system, the centre of the Penning trap is in fact a potential maximum for the particle. The blue sideband must be targeted to pump energy into this mode to localise the particle at the trap centre. The decay time is far greater than the oscillation periods, allowing this configuration to be stable over experimental timescales.

as a thermodynamic cooling limit for this process. In the optomechanical case, the ratio ω_l/ω_h may be in the range 10^{-5} to 10^{-14} [17], and usually other physical processes provide a higher limit before this is reached. As we will see, in our parametric cooling scheme the frequencies tend to be less distinct and this fundamentally restricts the maximum cooling achievable. We should note, however, that while most cooling schemes are concerned with reaching the quantum ground state, our goal is to inhibit phase slipping only, and a reduction in the fluctuations of order 50 % would be sufficient for our needs.

We now solve this system to determine the steady state and cooling rate. Damping and noise are incorporated by coupling each oscillator to its own Markovian reservoir. The relaxation times are γ_l^{-1} and γ_h^{-1} for the l and h modes respectively, and their equilibrium occupation numbers are ν_l and ν_h. In particular, this differs from many theoretical descriptions of cooling processes in that we include the reheating of the l mode by having it coupled to its own heat bath. The dissipative system dynamics are described by a master equation for the density matrix [119],

$$\begin{aligned}\frac{\partial\hat{\rho}}{\partial t} =&\gamma_l(1+\nu_l)(-\tfrac{1}{2}\hat{a}^\dagger\hat{a}\hat{\rho} + \hat{a}\hat{\rho}\hat{a}^\dagger - \tfrac{1}{2}\hat{\rho}\hat{a}^\dagger\hat{a}) + \gamma_l\nu_l(-\tfrac{1}{2}\hat{a}\hat{a}^\dagger\hat{\rho} + \hat{a}^\dagger\hat{\rho}\hat{a} - \tfrac{1}{2}\hat{\rho}\hat{a}\hat{a}^\dagger)\\ &\gamma_h(1+\nu_h)(-\tfrac{1}{2}\hat{b}^\dagger\hat{b}\hat{\rho} + \hat{b}\hat{\rho}\hat{b}^\dagger - \tfrac{1}{2}\hat{\rho}\hat{b}^\dagger\hat{b}) + \gamma_h\nu_h(-\tfrac{1}{2}\hat{b}\hat{b}^\dagger\hat{\rho} + \hat{b}^\dagger\hat{\rho}\hat{b} - \tfrac{1}{2}\hat{\rho}\hat{b}\hat{b}^\dagger)\\ &+\frac{1}{i\hbar}\left[\hat{H},\hat{\rho}\right]. \end{aligned} \tag{3.20}$$

This system can be solved for the steady state, yielding the expected occupation of the oscillators [120]. A simple approach is to derive Heisenberg equations of motion for all ten second-order moments $\{\langle\hat{a}^2\rangle, \langle\hat{a}\hat{b}\rangle, \langle\hat{a}^\dagger\hat{a}\rangle, \dots\}$. Importantly, these form a closed system and may be solved by setting all t-derivatives to zero. Due to the form of Eq. (3.18) the moments $\{\langle\hat{a}^\dagger\hat{a}\rangle, \langle\hat{b}^\dagger\hat{b}\rangle, \langle\hat{a}^\dagger\hat{b}\rangle, \langle\hat{a}\hat{b}^\dagger\rangle\}$ form a closed system by themselves. From Eq. (3.20) we produce a set of equations for the time evolution of the second-order moments

$$\frac{d}{dt}\vec{u} = \mathbf{M}\vec{u} + \vec{v}, \tag{3.21}$$

with $\vec{u} = \left(\langle\hat{a}^\dagger\hat{a}\rangle, \langle\hat{b}^\dagger\hat{b}\rangle, \langle\hat{a}^\dagger\hat{b}\rangle, \langle\hat{a}\hat{b}^\dagger\rangle\right)^T$, $\vec{v} = (\gamma_l\nu_l, \gamma_h\nu_h, 0, 0)^T$, and

$$\mathbf{M} = \begin{pmatrix} -\gamma_l & 0 & i\kappa_0 e^{-i\omega_d t} & -i\kappa_0 e^{i\omega_d t} \\ 0 & -\gamma_h & -i\kappa_0 e^{-i\omega_d t} & i\kappa_0 e^{i\omega_d t} \\ i\kappa_0 e^{i\omega_d t} & -i\kappa_0 e^{i\omega_d t} & -\frac{1}{2}(\gamma_l+\gamma_h) + i(\omega_h-\omega_l) & 0 \\ -i\kappa_0 e^{-i\omega_d t} & i\kappa_0 e^{-i\omega_d t} & 0 & -\frac{1}{2}(\gamma_l+\gamma_h) - i(\omega_h-\omega_l) \end{pmatrix}.$$

We transform (e.g.) $\hat{b} \to \hat{b}\, e^{i\omega_d t}$, and reach

$$\frac{d}{dt}\vec{u} = \mathbf{M}'\vec{u} + \vec{v}, \tag{3.22}$$

now with

$$\mathbf{M}' = \begin{pmatrix} -\gamma_l & 0 & i\kappa_0 & -i\kappa_0 \\ 0 & -\gamma_h & -i\kappa_0 & i\kappa_0 \\ i\kappa_0 & -i\kappa_0 & -\frac{1}{2}(\gamma_l+\gamma_h) - i\Delta\omega & 0 \\ -i\kappa_0 & i\kappa_0 & 0 & -\frac{1}{2}(\gamma_l+\gamma_h) + i\Delta\omega \end{pmatrix}, \tag{3.23}$$

with the detuning $\Delta\omega = \omega_d - (\omega_h - \omega_l)$. Formally, $\vec{u} = -\mathbf{M}'^{-1}\vec{v}$ yields the driven steady-state. This is the key result of this derivation, and for the l mode, this is

$$\langle \hat{a}^\dagger \hat{a} \rangle_{\rm ss} = \nu_l - \mathcal{S}(\nu_l - \nu_h), \tag{3.24}$$

where the scale factor $0 \leq \mathcal{S} \leq 1$ is given by $\mathcal{S} = \zeta/\gamma_l\chi$, and

$$\begin{aligned} \zeta &= \frac{\kappa_0^2(\gamma_l+\gamma_h)}{\Delta\omega^2 + (\gamma_l+\gamma_h)^2}, \\ \chi &= 1 + \frac{\zeta(\gamma_l+\gamma_h)}{\gamma_l\gamma_h}, \\ \Delta\omega &= \omega_d - (\omega_h - \omega_l). \end{aligned}$$

When $\mathcal{S} = 0$, there is no cooling. When $\mathcal{S} \to 1$, the cooling is maximal and the l mode contains on average ν_h quanta, i.e. it has been cooled to the temperature $(\omega_l/\omega_h)T$. The level of cooling achieved can be understood as a competition between several rates: the rate γ_l describing the reheating of the l mode, κ_0 describing the rate at which quanta may be transferred between the two modes, and the rate γ_h describing the rate of dissipation from the h mode. In the limit $\gamma_l \to 0$, $\mathcal{S} \to 1$ which can be interpreted as the coupling of the l mode to its reservoir becoming so low that the cooling process is able to achieve the theoretical limit Eq. (3.19). When $\gamma_h \to 0$, no dissipation is possible and $\mathcal{S} \to 0$. At the opposite limit, when $\gamma_h \to \infty$, $\mathcal{S} \to 0$ since the strength of the h mode-thermal bath coupling prevents the excitation of the h mode, as an instance of the quantum Zeno effect[6]. There is thus an optimal rate γ_h for cooling: in

[6]The quantum Zeno effect refers to the situation in which a quantum system, by means of continuous measurement, has its unitary time evolution suppressed and if excited is prevented from decay. There is the classical analogue in which the large damping rate γ_h results in an extremely broad resonance of the h mode, preventing strong excitation and hindering energy transfer to the h mode bath.

the special case $\Delta\omega = 0$, $\gamma_h^{(\mathrm{opt})} = \kappa_0$, implying the h mode decay rate should match the upconversion rate κ_0. Considering the coupling κ_0 between the oscillators, there is the trivial limit that $\mathcal{S} \to 0$ as $\kappa_0 \to 0$, namely that no cooling can be achieved as the oscillators are decoupled. The cooling then monotonically increases with κ_0. Finally, as the driving frequency ω_d is varied, the cooling displays a Lorentzian profile about detuning $\Delta\omega = 0$.

To extract the cooling rate, we examine the eigenvalues of the matrix $\mathbf{M}'$. This is trivial numerically, but we gain insight from analysing the perturbation of the eigenvalues of $\mathbf{M}'$ with κ_0. In particular, in the limit $\kappa_0 \ll (\gamma_l, \gamma_h)$ we can use second-order perturbation theory to estimate the rate. We decompose $\mathbf{M}' = \mathbf{M}_0 + \delta\mathbf{M}$, with $\mathbf{M}_0 = \mathrm{diag}[-\gamma_l, -\gamma_h, -\frac{1}{2}(\gamma_l + \gamma_h), -\frac{1}{2}(\gamma_l + \gamma_h)]$ and

$$\delta\mathbf{M} = \frac{i\kappa_0}{2}\begin{pmatrix} 0 & 0 & +1 & -1 \\ 0 & 0 & -1 & +1 \\ +1 & -1 & 0 & 0 \\ -1 & +1 & 0 & 0 \end{pmatrix}.$$

Applying standard perturbation theory results in a second order correction to the slowest eigenmode,

$$\gamma_{\mathrm{dr}} = \gamma_l + \frac{\kappa_0^2}{\gamma_h - \gamma_l} + \mathcal{O}(\kappa_0^3). \tag{3.25}$$

In the parametric cooling scheme of Chapter 4, we will be in the regime $\gamma_l < \gamma_h$, where we see that the cooling rate is determined by the thermalisation timescale of the l mode, somewhat accelerated by the driving term. This analysis depends on the decay rates γ_l and γ_h differing sufficiently that degenerate perturbation theory is not required. In practice this requirement is often satisfied, unless there is a physical basis for the decay rates to be related.

Finally, we can make the connection with Eq. (3.6) and the optomechanical scheme. If we transform Eq. (3.18) into a rotating frame with unitary $\hat{U} = \exp\left(i\omega_d t\ \hat{a}^\dagger\hat{a}\right)$, we arrive at

$$\hat{H} = \hbar(\omega_h + \Delta\omega)\hat{a}^\dagger\hat{a} + \hbar\omega_h\hat{b}^\dagger\hat{b} + \hbar\left(\kappa_0\hat{a}^\dagger\hat{b} + \kappa_0^*\hat{a}\hat{b}^\dagger\right).$$

Up to the rotating wave approximation, this is identical to Eq. (3.6). Note also that the transformation $\hat{U}$ will not affect the noise processes. Thus parametric modulation allows resonant energy exchange between the oscillators via down- and up-conversion of quanta.

3.4 Summary

In this chapter, the resolved sideband regime of laser-cooled optomechanical oscillators provided a vehicle for the discussion of the core physics of driven cooling processes. The specific form of the interaction Eq. (3.3) allowed for quanta in the mechanical mode to be upconverted to an optical mode from which they are dissipated. A cavity with a high quality factor then strongly enhances this process, enabling efficient cooling of the mechanical oscillator. In Sec. 3.2, the theory underlying a sideband cooling scheme for the Josephson phase was presented. This scheme is closely related, but hindered by the requirement of a moderate bias current to produce the coupling, and an intrinsic limit on the strength at which the Q_1 mode may be driven. Finally, we introduced the parametric cooling scheme in Sec. 3.3, in which the sidebands and thus upconversion instead arise from a direct modulation of the coupling strength. Otherwise, this is yet again the same model for the reduced two-oscillator system. We computed the key quantities of the cooling limit Eq. (3.24) and rate Eq. (3.25), which will be of importance for our predictions in Chapter 4.

4

Parametric cooling in short junctions

In this chapter, we make an initial proposal for cooling fluctuations of the superconducting order parameter in cuprates. The material of this chapter is based on the publication Denny et al. [35] for which I was lead author, having developed the theoretical analysis, performed all numerical simulations, and produced the initial draft of the manuscript.

For now, the challenges of achieving strong coupling to a cavity are being sidestepped[1] by exploiting bilayer cuprates where we may make use of the intralayer (high frequency) plasmon modes to cool the interlayer (low frequency) Josephson phase fluctuations. While a sideband scheme related to that of Hammer, Aprili, and Petković [34] could be used, this places strict requirements on the crystal dimensions[2]. Additionally, the bias current required for sideband schemes complicates any feasible experimental geometry. As an alternative route, we take inspiration from recent experiments [26, 27] in which infrared-active phonon modes are strongly driven, resulting in the observation of superconducting fluctuations up to 300 K.

We can consider the consequence of such a phonon driving by making a comparison with nonlinear optics. In a centrosymmetric nonlinear optical crystal, the polarisation

[1] We will return to this question in Chapter 5.

[2] Specifically, the effective junction length must be such that the $k = 1$ Josephson mode is high enough in frequency to be thermally unoccupied, but not so high that the radiation driving the transition will be capable of breaking pairs (Sec. 3.2).

density $P(t)$ may be expressed as a power series in the electric field,

$$P(t) = \epsilon_0 \chi^{(1)} E(t) + \epsilon_0 \chi^{(3)} E^3(t) + \dots$$

In a pump-probe formalism[3] we can write $E(t) \sim E_{\text{pump}} \cos \omega_d t + E_{\text{probe}} \cos \omega t$, and find the polarisation response to E_{probe} is given by

$$P(t) = \epsilon_0 \left(\chi^{(1)} + 3\chi^{(3)} E^2_{\text{pump}}(t) \right) E_{\text{probe}}(t) + \dots$$

The pump field thus provides an effective time-dependent susceptibility $\chi_{\text{eff}}(t) = \left(\chi^{(1)} + 3\chi^{(3)} E^2_{\text{pump}}(t) \right)$ of the medium for the probe field. In the cuprate, the driven phonon modes are IR-active and therefore have a finite dipole moment. The vibration has a direct influence on the crystal electrodynamics and can play the role of the pump field by providing a time-dependent susceptibility $\chi_{\text{eff}}(t)$. The Josephson dynamics have an associated electric field which may experience the modulated susceptibility. Note that this dependence is quadratic in E_{pump}, consistent with a qQ^2 coupling as observed in experiments [121]. This parametric modulation has the potential to be developed into a parametric cooling scheme, with the goal of upconverting fluctuations from the interlayer plasmon to the intralayer mode where their disruption to the superconducting state may be minimised.

In this chapter, we will study the potential of such a parametric scheme for cooling c-axis fluctuations, restricting to junctions in the short limit. We will first explore a toy two-junction model numerically in Sec. 4.2 and analytically in Sec. 4.2.2. In Sec. 4.3 we extend the numerics to a 100-junction stack, to more realistically simulate a small single crystal, and conclude by interpreting our numerical results as a guide to possible experiments and materials. We begin this chapter by developing a semi-microscopic model of the cuprate stack into a simple dynamical model for the Josephson phase.

4.1 Model derivation

A successful approach to modelling the electrodynamics of a superconducting stack was developed by Machida and Sakai [122]. Here, the superconducting order parameter is

[3] In a pump-probe formalism, we decompose the electric field E into a strong, driven component E_{pump} and a much weaker component E_{probe}. The component E_{pump} models the external driving, assumed to be strong enough to induce a nonlinear response in the medium. The weaker component E_{probe} models the fields associated with the Josephson electrodynamics, and allows us to determine their response to the strong driving E_{pump}.

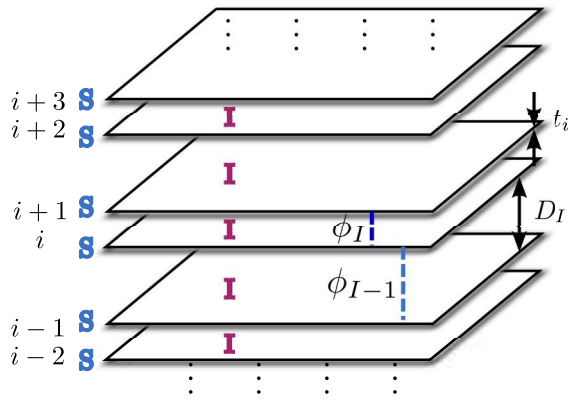

Figure 4.1: Schematic of the bilayer cuprate for the electrodynamical model. Superconducting sheets of finite thickness t_i are separated by insulating regions of thickness D_I. The Josephson effect provides coupling between the superconducting sheets.

treated as a classical field, with dynamics arising from the Josephson effect and classical electromagnetism. In particular, this approach pays attention to the penetration of the electric field into the finite-thickness superconducting sheets, which is necessary to correctly treat the capacitive coupling between adjacent junctions. In the short junction regime at low temperature, this coupling term is dominant. The key contribution of this section is to incorporate an effective time-dependent permittivity arising from the phonon driving.

First we define our notation. We will use the lowercase labels $\{i\}$ for all properties relating to the superconducting layers. For the Josephson junction formed with the insulator between superconducting layers $(i, i-1)$ we instead use the uppercase label I. The framework of Machida and Sakai [122] is semi-microscopic since it is based on the Schrödinger equation for the macroscopic superfluid wavefunction and derives the electric field coupling from the wavefunction dynamics. This culminates in the equation

$$\frac{\Phi_0}{2\pi}\partial_t\phi_I = -\frac{{\lambda_{c,i}^{(D)}}^2}{\epsilon_i^s}\rho_i + \frac{{\lambda_{c,i-1}^{(D)}}^2}{\epsilon_{i-1}^s}\rho_{i-1} + \int_{z_{i-1}}^{z_i} E_z dz. \tag{4.1}$$

for the Josephson phase dynamics of the gauge invariant phase ϕ_I between superconducting layers i and $i-1$, where Φ_0 is the flux quantum. This generalises the conventional Josephson relation, given by the last term in Eq. (4.1), to include the contribution arising from the superconducting layer charge densities ρ_i, given the su-

perconducting layers have a dielectric constant ϵ_i^s and a c-axis Debye length[4] $\lambda_{c,i}^{(D)}$. By considering the variation of the scalar, chemical and electrochemical potentials across a junction leads to the relation [122]

$$\rho_i = -\frac{\epsilon_i^s}{\lambda_{c,i}^{(D)^2}} \left(\Theta_i + \frac{\Phi_0}{2\pi} \frac{\partial \phi_I}{\partial t} \right), \tag{4.2}$$

where Θ_i is the scalar potential in the i^{th} superconducting layer. This, together with Eq. (4.1) and Gauss' law

$$\partial_z E_z = \frac{\rho_i}{\epsilon_i^s},$$

gives rise to an intuitive screening equation for the electric field inside the superconducting sheets,

$$\partial_z^2 E_{z,i} = \frac{1}{\lambda_{c,i}^{(D)^2}} E_{z,i}. \tag{4.3}$$

This acts in addition to the well-established London screening relation for the magnetic field inside the superconducting layers,

$$\partial_z^2 B_{y,i} = \frac{1}{\lambda_{ab,i}^2} B_{y,i}, \tag{4.4}$$

where $\lambda_{ab,i}$ is the effective London penetration depth for the i^{th} superconducting layer. For simplicity we will assume that ϕ_I is independent on y in the plane and so only consider x spatial phase variations.

For given E and B fields in the insulating layers, we now solve these equations to relate the electric field with the charge on the layer, and likewise the magnetic field with the screening currents. The derivation now diverges from that of Machida and Sakai [122]. In particular we model the effect of the driven c-axis phonon mode on the Josephson dynamics as a time-dependent modulation of the permittivity $\epsilon_I(t)$ about its equilibrium value ϵ_I for the insulator between the superconducting layers i and $i-1$. We will assume the time-dependence of the permittivity to follow $\epsilon_I(t) = \epsilon_I(t)(1 + \eta_I \sin^2 \omega_d t)$. Consequently we now deal with the boundary conditions at the superconductor/insulator interface to properly take account of this effect.

[4]The Debye length is the characteristic lengthscale of the electric potential, accounting for mobile charge density and mobility. In this particular scenario, if $t_i \gg \lambda_{c,i}^{(D)}$, the superconducting sheets can provide perfect electrostatic screening. The opposite regime where $t_i \ll \lambda_{c_i}^{(D)}$ describes a situation in which the sheets' screening is negligible.

For a superconducting layer of thickness t_i, with boundary conditions of $E = \{E_d,\ E_u\}$ for its *downside* (d) and *upside* (u), corresponding to $z - z_0 = \{0,\ t_i\}$ respectively, we find that the electric field inside is given by

$$E_{z,i}(z - z_0) = E_d \cosh\left(\frac{z - z_0}{\lambda_{c,i}^{(D)}}\right) + \frac{E_u - E_d \cosh(t_i/\lambda_{c,i}^{(D)})}{\sinh(t_i/\lambda_{c,i}^{(D)})} \sinh\left(\frac{z - z_0}{\lambda_{c,i}^{(D)}}\right).$$

There is a jump in the electric field between the insulator and the superconducting layer

$$E_I = \frac{\epsilon_i^s}{\epsilon_I(t)} E_d^i,$$

which arises from the boundary condition for the electric field at the interface between two media. We assume there is no sheet charge at the surface so instead screening occurs due to a charge distribution over the Debye length scale. This leads to

$$\rho_i^d = \frac{\epsilon_{I+1}(t) E_{I+1} - \epsilon_I(t) \cosh(t_i/\lambda_{c,i}^{(D)}) E_I}{\lambda_{c,i}^{(D)} \sinh(t_i/\lambda_{c,i}^{(D)})}, \tag{4.5a}$$

$$\rho_i^u = \frac{\epsilon_{I+1}(t) \cosh(t_i/\lambda_{c,i}^{(D)}) E_{I+1} - \epsilon_I(t) E_I}{\lambda_{c,i}^{(D)} \sinh(t_i/\lambda_{c,i}^{(D)})}, \tag{4.5b}$$

for the charge densities on the downside and upside of the i^{th} superconducting layer.

We now go back to the general Josephson relation Eq. (4.1) and substitute for the charge densities evaluated in Eq. (4.5) yielding

$$\frac{\Phi_0}{2\pi} \partial_t \phi_I = s_{I,I-1}^{C,d} E_{I-1} + D_I^C E_I + s_{I+1,I}^{C,u} E_{I+1}, \tag{4.6}$$

where the diagonal D^C and off-diagonal s^C capacitive couplings are

$$\begin{aligned} D_I^C(t) &= D_I + \frac{\epsilon_I(t)}{\epsilon_i^s} \lambda_{c,i}^{(D)} \coth\left(\frac{t_i}{\lambda_{c,i}^{(D)}}\right) + \frac{\epsilon_I(t)}{\epsilon_{i-1}^s} \lambda_{c,i-1} \coth\left(\frac{t_{i-1}}{\lambda_{c,i-1}}\right), \\ s_{I+1,I}^{C,u}(t) &= -\frac{\epsilon_{I+1}(t)}{\epsilon_i^s} \frac{\lambda_{c,i}^{(D)}}{\sinh(t_i/\lambda_{c,i}^{(D)})}, \\ s_{I,I-1}^{C,d}(t) &= -\frac{\epsilon_{I-1}(t)}{\epsilon_{i-1}^s} \frac{\lambda_{c,i-1}}{\sinh(t_i/\lambda_{c,i-1})}. \end{aligned} \tag{4.7}$$

Here D_I is the thickness of the insulator for the I^{th} junction. A similar equation relating the phase gradient to the magnetic field may be derived by solving for and eliminating the screening currents in the superconducting layer, giving

$$\frac{\Phi_0}{2\pi} \partial_x \phi_I = s_{I,I-1}^{L} B_{I-1} + D_I^L B_I + s_{I+1,I}^{L} B_{I+1}, \tag{4.8}$$

where the diagonal D^L and off-diagonal s^L inductive couplings are

$$D_I^L = D_I + \lambda_{ab,i} \coth\left(\frac{t_i}{\lambda_{ab,i}}\right) + \lambda_{ab,i-1} \coth\left(\frac{t_{i-1}}{\lambda_{ab,i-1}}\right),$$
$$s_{I+1,I}^L = -\frac{\lambda_{ab,i}}{\sinh(t_i/\lambda_{ab,i})}.$$

We now summarise Eq. (4.6) and Eq. (4.8) in matrix form as

$$\frac{\Phi_0}{2\pi}\partial_t\vec{\phi} = \mathbf{C}(t)\vec{E}, \tag{4.9}$$
$$\frac{\Phi_0}{2\pi}\partial_x\vec{\phi} = \mathbf{L}\vec{B}, \tag{4.10}$$

where $\mathbf{C}(t)$ and $\mathbf{L}$ contain the capacitive and inductive couplings, respectively, and with the former being time-dependent owing to $\epsilon_I(t)$.

Considering the insulating layers and applying Maxwell's equations gives

$$\partial_x B_I^y = \frac{\epsilon_I(t)}{c^2}\partial_t E_I^z + \mu_0 J_I^z, \tag{4.11}$$

where $J_I^z = J_I^c \sin\phi_I + \sigma E_I^z$ is the c-axis current through the junction, composed of the Josephson supercurrent, quantified by its critical current J_I^c and the quasi-particle current, quantified by its conductivity σ. Substituting Eq. (4.9) and Eq. (4.10) into Eq. (4.11) we reach a closed equation concerning just the phase dynamics,

$$\frac{\Phi_0}{2\pi}\sum_J \left[\mathbf{L}^{-1}\right]_{IJ}\partial_x^2\phi_J = \frac{\Phi_0}{2\pi}\frac{\epsilon_I(t)}{c^2}\sum_J \left[\mathbf{C}^{-1}(t)\right]_{IJ}\partial_t^2\phi_J + \mu_0 J_I^c \sin(\phi_I) + \frac{\Phi_0}{2\pi c^2}\sum_J \left\{\epsilon_I(t)\left[\partial_t\mathbf{C}^{-1}(t)\right]_{IJ} + \frac{\sigma}{\epsilon_0}\left[\mathbf{C}^{-1}(t)\right]_{IJ}\right\}\partial_t\phi_J. \tag{4.12}$$

Aside from the assumptions of the layered stack and a time-dependent $\epsilon_I(t)$ within the insulating layers, this equation provides a general description of Josephson phase dynamics in the cuprates. In particular each term in Eq. (4.12) has an intuitive interpretation. The $\sin(\phi_I)$ term describes supercurrents, the $\partial_x^2\phi_J$ accounts for inductive coupling, the $\partial_t^2\phi_J$ accounts for capacitive coupling, and the $\partial_t\phi_J$ terms describes quasi-particle current between layers. We focus on short junctions where we can assume ϕ_I is x-independent.[5] For the moment we also drop the incoherent quasiparticle current terms since its damping contribution to the dynamics are accounted for in Sec. 4.2 when we move to a Langevin description. For a given junction I we are left with

$$\partial_t^2\phi_I + \frac{2\pi}{\Phi_0}\sum_J \frac{C_{IJ}(t)J_J^c}{\epsilon_0\epsilon_J(t)}\sin(\phi_J) = 0. \tag{4.13}$$

[5]In sufficiently short junctions, in-plane fluctuations are energetically prohibited.

Writing out the individual terms in the sum we obtain

$$\partial_t^2\phi_I+\frac{2\pi}{\Phi_0\epsilon_0}\left[J^c_{I-1}\frac{s^{C,d}_{I,I-1}(t)}{\epsilon_{I-1}(t)}\sin(\phi_{I-1})+J^c_I\frac{D^C_I(t)}{\epsilon_I(t)}\sin(\phi_I)+J^c_{I+1}\frac{s^{C,u}_{I+1,I}(t)}{\epsilon_{I+1}(t)}\sin(\phi_{I+1})\right]=0.$$

Note that from Eq. (4.7) the ratios $s^{C,d}_{I,I-1}(t)/\epsilon_{I-1}(t)$ and $s^{C,u}_{I+1,I}(t)/\epsilon_{I+1}(t)$ describing off-diagonal capacitive couplings are in fact time-independent. Moreover in the diagonal coupling $D^C_I(t)/\epsilon_I(t)$ only the first term $D_I/\epsilon_I(t)$ retains the time-dependence and so it alone accounts for the modulation by the phonon.

We now make the assumption that all superconducting layers are identical (i.e. $\epsilon^s_i = \epsilon^s_{i+1} = \epsilon^s$, $t_i = t_{i+1}$, $\lambda^{(D)}_{c,i} = \lambda^{(D)}_{c,i+1} = \lambda^{(D)}_c$), and first consider the equilibrium case in which the permittivity is time-independent. We define a dimensionless coupling parameter α according to

$$\frac{\alpha^2}{(2\alpha+1)^2}=\frac{s^{C,d}_{I,I-1}s^{C,d}_{I+1,I}}{D^C_I D^C_{I+1}}.$$

We can then define a frequency associated with the junction I as

$$\varpi_I^2=\frac{1}{2\alpha+1}\frac{2\pi}{\Phi_0}\frac{J^c_I D^C_I}{\epsilon_0\epsilon_I},$$

which enables us to rewrite the equation of motion Eq. (4.13) as

$$\partial_t^2\phi_I+\alpha\varpi^2_{I-1}\sin(\phi_{I-1})-(2\alpha+1)\varpi^2_I\sin(\phi_I)+\alpha\varpi^2_{I+1}\sin(\phi_{I+1})=0. \tag{4.14}$$

The result is that the microscopic material parameters have been expressed as phenomenological frequencies ϖ_I and a capacitive coupling constant α. Regarding notation, here we have chosen to use ϖ to denote a junction's frequency, in contrast with ω_p as used up until now. The reason is that here our interest is principally in the junction stack, where the observed resonances are in fact the normal modes of the coordinates $\{\phi_I\}$, and we wish to reserve the symbol ω for the frequencies of the physical resonances. The form Eq. (4.14) is particularly useful, since it coincides with that of the well-known Koyama-Tachiki model [123]. There are two limiting cases here, the first being the limit of $\alpha \to 0$, corresponding to extremely thick superconducting layers and uncoupled junctions. The opposite limit, $\alpha \to \infty$, corresponds to the limit $t_i \to 0$ where the superconducting sheets become infinitesimally thin. Experimentally the coupling strength α has been determined to take values in the range $0.1 \to 5$ [124].

Moving to the driven case with time-dependent permittivity, we reconsider Eq. (4.13), finding that the equation of motion is modified by the introduction of a relative driving

strength

$$\begin{aligned}\eta_I(t) &= (2\alpha+1)\frac{D_I}{D_I^C}\left(\frac{\epsilon_I}{\epsilon_I(t)}-1\right)\\ &\approx \eta_I \sin^2(\omega_d t),\end{aligned} \tag{4.15}$$

where we have taken a Taylor expansion of $\epsilon_I(t)$ about 1, allowing Eq. (4.13) to be expressed as

$$\partial_t^2\phi_I + \alpha\varpi_{I-1}^2\sin(\phi_{I-1}) - [2\alpha+1+\eta_I(t)]\varpi_I^2\sin(\phi_I) + \alpha\varpi_{I+1}^2\sin(\phi_{I+1}) = 0, \tag{4.16}$$

again using α and ϖ_I as defined above. This captures the deterministic dynamics of our model: the Josephson dynamics, nearest-neighbour capacitive coupling, and the parametric modulation arising from the nonlinear phonon driving, explicitly assumed to arise from a q^2 coupling in Eq. (4.15). It is notable that the modulation $\eta_I(t)$ only appears in the diagonal term of Eq. (4.16), suggesting that the coupling between adjacent junctions is highly constrained.

4.2 Toy model: Two junctions

Josephson junction dynamics are known to display a complex interplay between coherent and dissipative contributions [125]. This includes quasiparticle currents (as in the preceding section) as well as long-wavelength phonon modes and other microscopic degrees of freedom. The predominant effect of these couplings is to provide a source of continuous rethermalisation of the Josephson phase degrees of freedom. In our model, we account for this by adopting a classical Langevin framework. Here we examine the special case of two junctions to expose the key physics of this system, and later generalise to a stack of junctions.

We linearise Eq. (4.16) and move to the normal mode frame[6] with $\eta_I(t)$ replaced by its time-average $\frac{1}{2}\eta_I$. The additional Langevin terms give

$$\begin{aligned}\partial_t^2\varphi_l - \gamma_l\partial_t\varphi_l + \omega_l^2(t)\varphi_l + \Delta_h(t)\varphi_h &= \xi_l(t),\\ \partial_t^2\varphi_h - \gamma_h\partial_t\varphi_h + \omega_h^2(t)\varphi_h + \Delta_l(t)\varphi_l &= \xi_h(t),\end{aligned} \tag{4.17}$$

[6]The relatively strong coupling between adjacent junctions means that if we apply thermalising Langevin terms locally, the steady state of the system is not guaranteed to be thermal as evidenced by the statistics of $\{\phi_I, p_I\}$. This is of practical relevance for the simulation of the resulting model.

where $\varphi_{l,h}$ are the normal mode phase coordinates. Importantly the driving introduces a time-dependent off-diagonal coupling

$$\Delta_{l,h}(t) = \Delta_{l,h}\cos(2\omega_d t),$$

where

$$\Delta_l = -\frac{\alpha^2}{2(2\alpha+1)^2}\eta_h\varpi_l^2,$$
$$\Delta_h = -\tfrac{1}{2}\eta_h\varpi_h^2,$$

to lowest order in $r = \varpi_l/\varpi_h$. Similarly the driving also induces a modulation of the normal mode frequencies

$$\omega_{l,h}^2(t) = \omega_{l,h}^2 - \tfrac{1}{2}A_{l,h}^2\cos(2\omega_d t),$$

with $A_l^2 = [\eta_l + \frac{\alpha^2}{(2\alpha+1)^2}\eta_h]\varpi_l^2$ and $A_h^2 = \eta_h\varpi_h^2$. The quadratic nature of the driving shifts the normal mode frequencies $\omega_{l,h}$, in line with experimental observations [26, 27]. We approximate the noise $\xi_{l,h}(t)$ as independent, white and Gaussian, as described by

$$\langle\xi_{l,h}(t)\xi_{l,h}(t')\rangle = \Gamma_{l,h}\delta(t-t'),$$

and it is related to the damping by the fluctuation-dissipation theorem as

$$\Gamma_l = 2\gamma_l\omega_l^2(T/T_0), \quad \text{and}$$
$$\Gamma_h = 2\gamma_h\omega_l^2(\omega_l/\omega_h)^2(T/T_0),$$

where T_0 is a system dependent temperature scale set by the capacitive energy associated to the mode φ_l[7]. In the absence of driving the damping and noise will thermalise the system at a temperature T. In contrast to well isolated quantum optical/atomic systems, their continued presence during the driving we consider here accounts for persistent reheating expected in a solid-state system.

4.2.1 Numerical results

This section presents results arising from the numerical integration of the model presented, in the simple case of two junctions. This is valuable, as an analytical estimate of cooling limits and rates can be made (Sec. 4.2.2) and compared with these numerical

[7]We will discuss the physical significance of the temperature scale T_0 in Sec. 4.3.1, however this depends on a numerical treatment and so we must first introduce the numerical methods to be used.

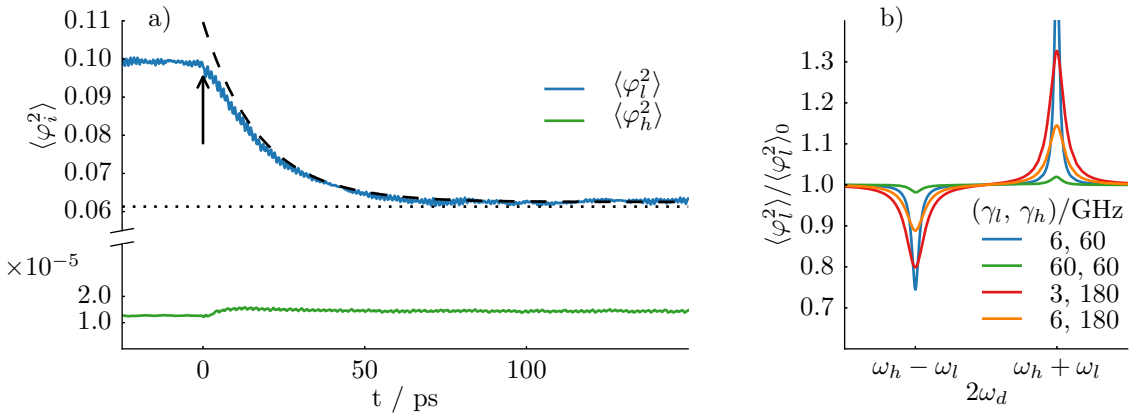

Figure 4.2: Parametric cooling in a two-junction unit cell with (undriven) normal modes $\omega_l = 2\pi \times 1$ THz, $\omega_h = 2\pi \times 10$ THz, $\gamma_l = 0.19$ THz, $\gamma_h = 3.63$ THz, $\alpha = 1$, $\eta_l = 0$ and $\eta_h = 0.1$. (a) We simulate 500 trajectories of the system Eq. (4.17) and average the phase and conjugate momentum quadratures $\langle\varphi_i^2\rangle$ of the inter- and intrabilayer modes across these trajectories. The system is allowed to thermalise until $t = 0$ (indicated) where $T_{\text{initial}}/T_0 = 0.1$, then parametric driving is applied, after which fluctuations on both quadratures of the inter- (intra-) bilayer mode are cooled to $0.6T_{\text{initial}}$ (heated to $1.2T_{\text{initial}}$). The statistical error in these quantities is of the order of the jitter on the plot. Analytic predictions of steady state (dotted line) and asymptotic cooling rate (dashed line) are also shown. (b) A plot of the driven steady state of the quadrature $\langle\varphi_l^2\rangle$ as a function of driving frequency ω_d. The cooling/heating sidebands of the interbilayer mode are observed as the driving frequency ω_d is varied for a selection of damping rates.

calculations. We may then more confidently advance to the general case of a stack of junctions, where the analytic approach is no longer feasible. We integrate the stochastic differential equations Eq. (4.17) with a quasi-symplectic velocity Verlet propagator [126]. We refer to Appendix A for further details of the numerical integration procedure. In Fig. 4.2 we display system dynamics for a representative set of relevant parameters for bilayer cuprates when driving at the difference frequency $\omega_d = \frac{1}{2}(\omega_h - \omega_l)$. Since the intrabilayer junction is typically more highly damped we have taken $\gamma_h > \gamma_l$. As shown in Fig. 4.2(a), once the driving is switched on the phase fluctuations of the interbilayer mode φ_l are strongly suppressed. Up-conversion correspondingly causes fluctuations to increase on the intrabilayer mode φ_h, however fluctuations remain small. Fluctuations

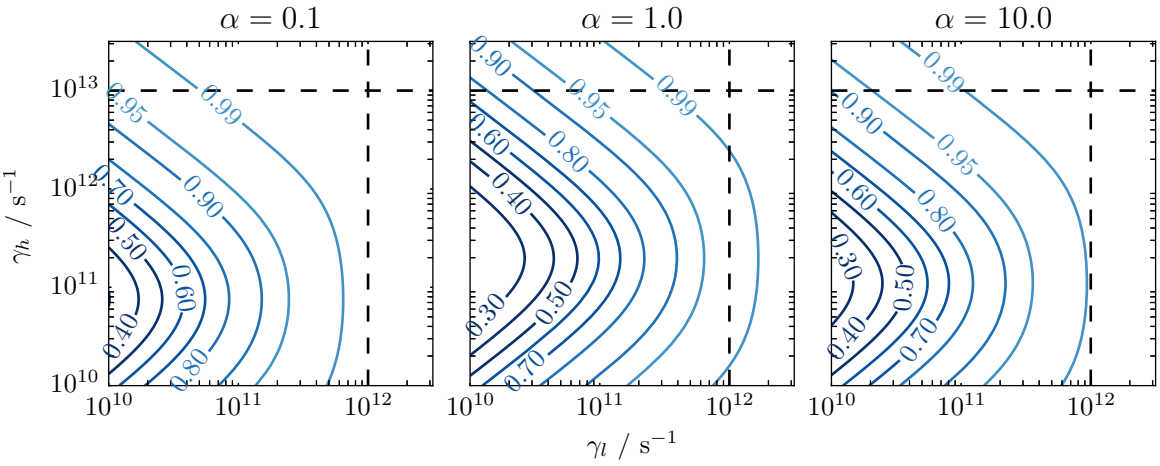

Figure 4.3: For the two-junction unit cell, relative temperature reduction $T/T_0 = \langle\varphi_l^2\rangle/\langle\varphi_{l,0}^2\rangle$ as a function of damping rates γ_l and γ_h, and the capacitive interlayer coupling α, as predicted by Eq. (4.23). Dashed lines indicate the frequencies of the two oscillators, indicating that cooling tends to be optimised into the underdamped regime. Note however that there is an optimal dissipation rate for the high-frequency mode.

in the conjugate momentum (not shown) for the two modes behave similarly. Although the resulting steady state is non-thermal the level of fluctuations is consistent with φ_l being substantially cooled, and φ_h being heated. The ω_d dependence of the effect is shown in Fig. 4.2(b) where cooling (red) and heating (blue) sidebands are observed at $\omega_d = \frac{1}{2}(\omega_h - \omega_l)$ and $\omega_d = \frac{1}{2}(\omega_h + \omega_l)$, respectively.

4.2.2 Theory for cooling

The simple theory developed by Vyatchanin [120] can be applied to understand the cooling process as an implementation of parametric cooling in the normal modes frame of the oscillators. The relevant general theory has been set out in Sec. 3.3; here we focus on its application.

We will analyse the two junction model described by Eq. (4.17). We estimate the key properties of the cooling process, such as the final temperature and cooling rate, by neglecting the modulation of the normal mode frequencies $\omega_m(t)$, and retaining only the modulation of the couplings $\Delta_m(t)$. Our approximation is that we neglect the time-dependence of $\omega_i(t)$, and assume that only the modulated coupling terms in this

frame give rise to cooling. The Hamiltonian producing the dynamics Eq. (4.17) under this approximation is given by

$$H = \frac{p_l^2}{2\Delta_l} + \frac{p_h^2}{2\Delta_h} + \tfrac{1}{2}\Delta_l\omega_l^2\varphi_l^2 + \tfrac{1}{2}\Delta_h\omega_h^2\varphi_h^2 + \cos(2\omega_d t)\Delta_l\Delta_h\varphi_l\varphi_h. \tag{4.18}$$

The quantity $p_{l,h}$ is the conjugate momentum[8] to $\varphi_{l,h}$. To exploit the parametric cooling results of Vyatchanin [120] we quantise and apply a rotating wave approximation. This amounts to promoting the phase normal coordinates φ_i and their conjugate momenta p_i to operator status, $(\varphi_i, p_i) \to (\hat{\varphi}_i, \hat{p}_i)$, and defining ladder operators according to

$$\begin{aligned}
\hat{a} &= \sqrt{\frac{\Delta_l\omega_l}{2\hbar}}\left(\hat{\varphi}_l + \frac{i}{\Delta_l\omega_l}\hat{p}_l\right),\\
\hat{a}^\dagger &= \sqrt{\frac{\Delta_l\omega_l}{2\hbar}}\left(\hat{\varphi}_l - \frac{i}{\Delta_l\omega_l}\hat{p}_l\right),\\
\hat{b} &= \sqrt{\frac{\Delta_h\omega_h}{2\hbar}}\left(\hat{\varphi}_h + \frac{i}{\Delta_h\omega_h}\hat{p}_h\right),\\
\hat{b}^\dagger &= \sqrt{\frac{\Delta_h\omega_h}{2\hbar}}\left(\hat{\varphi}_h - \frac{i}{\Delta_h\omega_h}\hat{p}_h\right),
\end{aligned}$$

which after dropping the zero-point terms yields

$$\hat{H} = \hbar\omega_l\hat{a}^\dagger\hat{a} + \hbar\omega_h\hat{b}^\dagger\hat{b} + \hbar\sqrt{\frac{\Delta_l\Delta_h}{\omega_l\omega_h}}\cos(2\omega_d t)\left(\hat{a} + \hat{a}^\dagger\right)\left(\hat{b} + \hat{b}^\dagger\right). \tag{4.19}$$

We make the rotating wave approximation, i.e. neglect the counter-rotating terms $\hat{a}\hat{b}$ and $\hat{a}^\dagger\hat{b}^\dagger$, giving the Hamiltonian

$$\hat{H} = \hbar\omega_l\hat{a}^\dagger\hat{a} + \hbar\omega_h\hat{b}^\dagger\hat{b} + \hbar\left[\kappa(t)\hat{a}\hat{b}^\dagger + \kappa^*(t)\hat{a}^\dagger\hat{b}\right]. \tag{4.20}$$

In this approximation we reach a coupling modulated according to $\kappa(t) = \kappa_0\exp(2i\omega_d t)$, and $\omega_d \approx \frac{1}{2}(\omega_h - \omega_l)$, $\kappa_0 \ll \omega_l$. More explicitly the magnitude of the coupling κ_0 is

$$\kappa_0^2 = (\Delta_h\Delta_l)/(\omega_l\omega_h) = \frac{1}{4}(\eta_h^2\omega_h^2)g(\alpha)\,r + \mathcal{O}(r^3), \tag{4.21}$$

with $g(\alpha) = \alpha^2/(2\alpha+1)^2\sqrt{3\alpha^2+4\alpha+1}$, and is maximised at $\alpha = \alpha_0 \approx 1.07$, where $g(\alpha_0) \approx 0.04$. The asymptotic cooling rate is

$$\gamma_{\mathrm{dr}} = \gamma_l + \frac{\kappa_0^2}{\gamma_h - \gamma_l} + \mathcal{O}(\kappa_0^3), \tag{4.22}$$

[8] As the canonical momentum p_i is conjugate to a normal mode of the gauge-invariant phase difference of the junction, there is no convenient physical interpretation to be made regarding this quantity. In particular, it is not simply related to number differences between the superconducting sheets.

and the steady state fluctuations for the interbilayer mode are

$$\frac{\langle\varphi_l^2\rangle}{\langle\varphi_l^2\rangle_0} = 1 - \mathcal{S}\left(1 - \frac{\omega_l}{\omega_h}\right), \tag{4.23}$$

where the scale factor $0 \leq \mathcal{S} \leq 1$ is given by $\mathcal{S} = \zeta/\gamma_l\chi$, with $\zeta = \kappa_0^2(\gamma_l + \gamma_h)/[\Delta\omega^2 + (\gamma_l+\gamma_h)^2]$, $\chi = 1+\zeta(\gamma_l+\gamma_h)/\gamma_l\gamma_h$, and $\Delta\omega = 2\omega_d-(\omega_h-\omega_l)$. Note that $\mathcal{S} = 0$, indicating no cooling, occurs if either $\gamma_h = 0$ or $\kappa_0 = 0$, while for an undamped interbilayer mode $\gamma_l = 0$ with $\gamma_h, \kappa_0 > 0$, we have $\mathcal{S} = 1$ giving the maximum suppression of fluctuations. With increasing $\gamma_l > 0$, $\mathcal{S}$ decreases monotonically implying the interbilayer should be underdamped, and $\mathcal{S}$ displays the expected resonance around $\Delta\omega = 0$. The prediction Eq. (4.23) is plotted in Fig. 4.3 for a range of values of γ_l, γ_h and α. Across these parameters, we note that a minimising γ_l is preferable. By contrast, there is an optimal value of γ_h which depends on α. When γ_h is too low, there is not enough dissipation to remove the upconverted excitations. When γ_h is too high, the bath coupling hinders excitation of the h mode as an instance of the quantum Zeno effect. Regarding the capacitive coupling α, around $\alpha = 1.0$ the coupling between the l and h modes is maximised and the optimum value of γ_h takes its highest value. The parameter α determines how rapidly quanta may be upconverted to the h mode, and a higher optimum value of γ_h is needed to provide sufficient dissipation.

The predictions of this analysis are included in Fig. 4.2(a), and over a wide parameter regime we find they agree with the numerical solution to within a few percent. Since the φ_h mode is more massive by a ratio $(\omega_h/\omega_l)^2$, perturbing its bare frequency has a more significant effect on the instantaneous normal modes of the system. Consequently κ_0 depends only on η_h to leading order in r, so modulation of the intrabilayer insulator is predicted to be most effective.

4.2.3 Quantum regime

The classical Langevin framework, used above, neglects quantum fluctuations of the Josephson phase. However, even at 300 K we have a mean occupation of the intralayer plasmon of $n = [\exp(\hbar\omega_h/k_BT) - 1]^{-1} \sim 0.25$ at 10 THz, and so it cannot be assumed that the quantum noise on this oscillator will be insignificant. In this section, we examine this approximation for the two junction system and find that the expressions

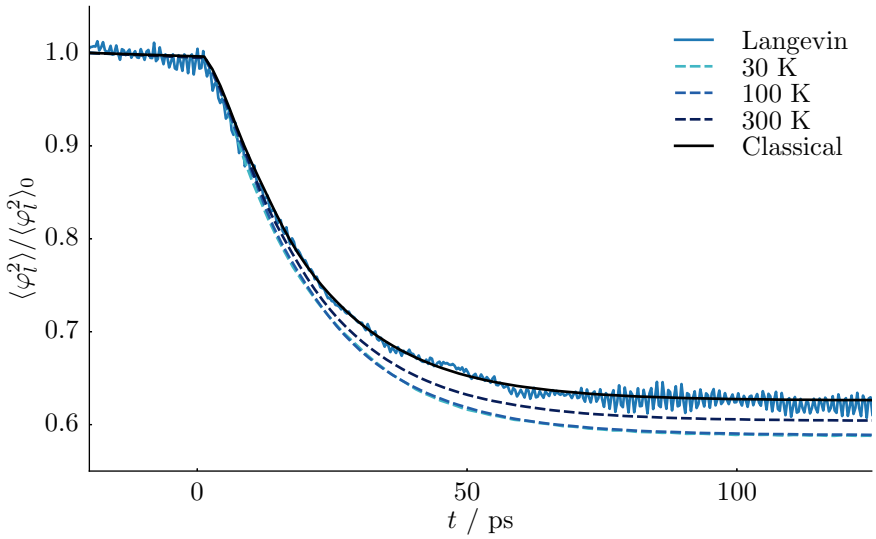

Figure 4.4: (a) Comparison of the quantum calculation of Sec. 4.2.3 with the classical Langevin results presented in Fig. 4.2. 'Langevin' is a reproduction of the statistics from classical Langevin trajectories. The dotted curves present quantum master equation predictions for $\langle\varphi_l^2\rangle$ for varying temperature T. The quantity plotted is $(\langle\varphi_l^2\rangle - \langle\varphi_l^2\rangle_{\rm qu})/(\langle\varphi_l^2\rangle_0 - \langle\varphi_l^2\rangle_{\rm qu,0})$, namely the cooling of the *classical fluctuations* of the interlayer plasmon. We find the classical Langevin approach gives an accurate description of the cooling of the thermal fluctuations over the entire relevant temperature range.

Eqs. (4.22–4.23) for the cooling limit and rate accurately predict the cooling of the *classical* component[9] of the phase fluctuations down to the lowest temperatures.

We take Eq. (4.19) and keep the time-dependence of the oscillator frequencies $\omega_i(t)$ such that $\hat{H}_l(= \hbar\omega_l\hat{a}^\dagger\hat{a})$ and $\hat{H}_h(= \hbar\omega_h\hat{b}^\dagger\hat{b})$ become time-dependent. We evolve the system of equations for $\langle\hat{a}^2\rangle$, $\langle\hat{a}^\dagger\hat{a}\rangle$, ... that result from the master equation Eq. (3.20), via

$$\partial_t\langle\hat{O}\rangle = \mathrm{Tr}\left(\hat{O}\,\partial_t\hat{\rho}\right). \tag{4.24}$$

This is more general than the calculation by Vyatchanin since it (i) retains counter-rotating terms, and (ii) keeps the time-dependence of the oscillator frequencies.

We are concerned with the cooling of *thermal* fluctuations of the interbilayer mode, and so we consider the figure of merit to be the fluctuations of the φ_l- and p_l-quadratures once the *quantum* component has been subtracted. We write this as $(\langle\varphi_l^2\rangle - \langle\varphi_l^2\rangle_{\rm qu})$,

[9]Note that this is the *only* component of the phase fluctuations which may be cooled.

where $\langle\varphi_l^2\rangle$ is the fluctuations of the φ_l quadrature, and $\langle\varphi_{\rm qu}^2\rangle$ is the fluctuations corresponding to the oscillator ground state. We then consider the ratio of $(\langle\varphi_l^2\rangle - \langle\varphi_l^2\rangle_{\rm qu})$ under parametric cooling to its thermal value. In Fig. 4.4, we plot the evolution of this ratio, $(\langle\varphi_l^2\rangle - \langle\varphi_l^2\rangle_{\rm qu})/(\langle\varphi_l^2\rangle_0 - \langle\varphi_l^2\rangle_{\rm qu,0})$, for a range of temperatures T spanning a region around occupation numbers $n_l \sim 1$. Despite slight technical differences in the thermalisation processes[10], there is excellent agreement between the classical Langevin calculation and the quantum master equation. The curve labelled 'Classical' in Fig. 4.4 is the (non-physical[11]) high-temperature limit of the quantum master equation calculation, and as expected shows that the two approaches converge once both oscillators are in the limit of containing many quanta. The classical Langevin calculation thus accurately captures the cooling of the thermal fluctuations allowing the analysis to use classical methods for the non-linear regime of the stack.

4.3 Multilayered stack

We now consider the full nonlinear dynamics of a stack of 100 junctions described by Eq. (4.16) using the classical Langevin treatment outlined. To recapitulate, Eq. (4.16) gives the coupled nonlinear dynamics of the Josephson phase variables on the individual junctions. We then linearised about the stable equilibrium and transformed to the normal modes picture where we added Langevin noise. As shown in Fig. 4.5(a)(inset) the linearised normal modes of the stack now form bands, $\varphi_{l,i}$ and $\varphi_{h,i}$, of low and high frequency plasmons which we take as being uniformly damped at rates γ_l and γ_h, respectively. We then applied the scheme at temperature $T \approx 0.7\,T_c$ and show the fluctuations of the modes $\varphi_{l,i}$ in Fig. 4.5(a) for the case where the driving ω_d is tuned to twice the difference frequency near the lower edge of the bands (indicated). As with the two junction case a suppression of phase fluctuations is observed for nearby modes. The steady-state driven fluctuations of $\varphi_{l,i}$ when ω_d targets different regions of the interbilayer band are shown in Fig. 4.5(b). Also plotted is the response for coloured driving equally superposing three different values of ω_d showing that broadband driving

[10]The common factor in both thermalisation processes is that operationally, both drive to the appropriate thermal state, either quantum or classical.

[11]The curve labelled 'Classical' corresponds to a technically non-physical scenario, since in the limit of arbitrarily many quanta in the interlayer plasmon, the harmonic approximation of the washboard potential no longer holds. Still, it does give the classical limit in which the zero-point fluctuations have become negligible and thus is the appropriate limit to compare with the Langevin result.

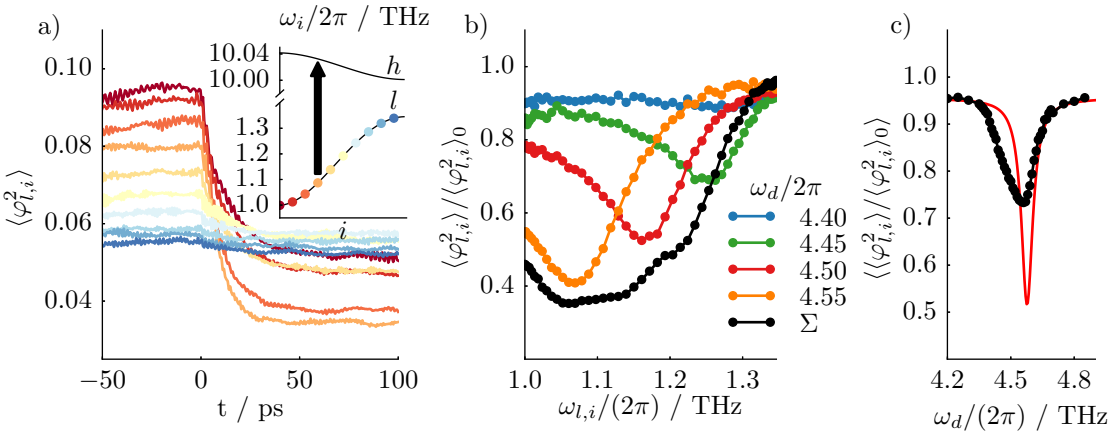

Figure 4.5: (a) Langevin simulation of a 100-junction stack as described by the multi-mode generalisation of Eq. (4.17). 500 independent realisations of the noise process were simulated, with the quadratures $\langle\varphi^2_{l,i}\rangle$ being averaged across these trajectories. A selection of 10 modes have been displayed across the interbilayer band as shown in the inset. The system is allowed to thermalise until $t = 0$ when the parametric driving term is turned on, resulting in a selective reduction of $\varphi_{l,i}$ fluctuations, where a steady state of $T/T_c \approx 0.7$ is reached. (b) In the steady-state the relative fluctuations $\langle\varphi^2_{l,i}\rangle/\langle\varphi^2_{l,i}\rangle_0$ for each mode in the interbilayer band is plotted for a selection of driving frequencies ω_d. Modes more closely resonant with the driving display a greater degree of cooling. Additionally, the curve labelled 'Σ' is the sum of the three terms at 4.45, 4.5 and 4.55 THz, and displays cooling across a broader range of frequencies. (c) Cooling sideband for the stack (black, dotted) as compared with the cooling sideband for a bilayer unit cell (red) with identical physical parameters as used in (a) and (b), and monochromatic driving. The increased bandwidth of the transition manifests as a broader and less sharp resonance. For the stack, the value of $\langle\varphi^2_i\rangle/\langle\varphi^2_i\rangle_0$ is averaged over all modes in the l band.

can induce suppression over a wide range of the band. In Fig. 4.5(c) we plot the red sideband (black, dotted) for the stack of junctions, as calculated by taking the mean suppression of fluctuations across the band. For comparison we plot the single junction sideband for identical parameters. As should be expected, the band has broadened the resonance.

A complementary characterisation of the stack is given by the c-axis superconducting transport properties quantified by the switching current distribution. To obtain

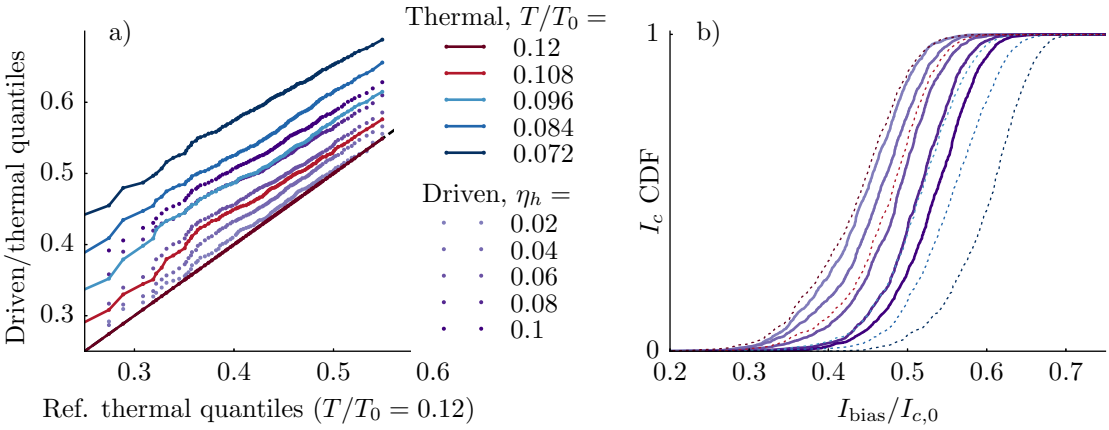

Figure 4.6: Results on the switching current distribution of the 100-junction stack, as simulated by the Langevin dynamical approach. The system is allowed to thermalise for 100 ps, after which a linear ramp of the bias current from 0 to $I_{c,0}$ is performed in a time Δt =1 ns. Due to thermal fluctuations, the effective junctions will switch from their superconducting behaviour to a resistive behaviour at a current $I_c < I_{c,0}$. (a) A quantile-quantile plot (see footnote 12) of switching current distributions for driving strengths $\eta_h = 0 \to 0.1$, at $T/T_0 = 0.12$ ($T/T_c \approx 0.7$). Thermal curves are relative to this temperature. The solid lowest line indicates the initial thermal distribution. (b) Numerically computed CDF of switching current at $\alpha = 1$ with a sweep time $\Delta t = 1$ ns. Solid lines are the driven stack with different driving strengths as in (a) while the dotted lines correspond to thermal benchmarks. Lower temperatures push the switching current distribution up to higher critical currents, as does an increased driving strength η_h. Comparison of the two enables an estimate of the effective temperature to be made.

this, the bias current $I_{\mathrm{bias}}(t)$ was linearly ramped from zero up to the critical current I_c in a time Δt. The tilt of the washboard potential of every junction in the stack increases until a phase slip event occurs, at which point the potential difference across the stack becomes finite. Experimentally, performing a ramp in 1 ns would be extremely fast, however it is in the appropriate regime (much longer than the oscillation and damping rates $\mathcal{O}(\mathrm{THz})$) and is numerically preferable by avoiding extremely long integrations in time. Furthermore, for a single junction, such switching current situations are well-studied, and provided the rate $1/\Delta t$ is low enough, the distribution of

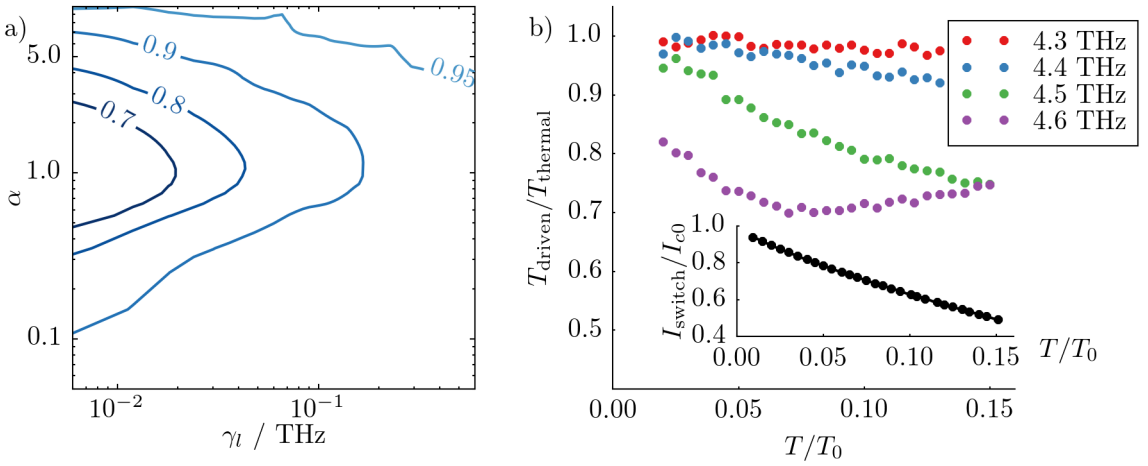

Figure 4.7: (a) A parameter sweep of the cooling ratio achieved as the parameters α (capacitive coupling) and γ_l (l mode damping) are varied. The system is simulated using the Langevin dynamical method, and the steady state under parametric driving is obtained. For the steady state, we plot the contours of $\langle \sin^2 \varphi_{l,i} \rangle / \langle \sin^2 \varphi_{l,i} \rangle_0$ averaged across the interbilayer band. Here we have taken $\gamma_h = 0.1\omega_h$, $\omega_l/\omega_h = 10$. This emphasises the optimality of low damping γ_l, and an intermediate $\alpha \sim 1$. (b) The temperature dependence of the cooling efficiency, as measured for the 100 junction stack using switching current measurements. Switching current measurements were taken as in Fig. 4.6 for initial temperatures in the range $0.01T_0 \leq T_{\text{initial}} \leq 0.15T_0$. For each temperature, the distribution mean is estimated and a temperature inferred by comparing with thermal switching current measurements. This relationship is displayed in the inset. At lower temperatures, the switching distribution shifts to higher bias currents where the Josephson plasmon frequency is reduced as in Eq. (2.19). As such, the optimal driving frequency at low temperature is *greater* than that at moderate temperature, since the interbilayer plasmon frequency is reduced while the intrabilayer plasmon is essentially unaffected.

I_{switch} is largely independent of Δt [41]. In Fig. 4.6(a) the Q-Q plot[12] for the computed statistics of this process are reported. This compares the quantiles of the original thermal distribution to those of the stack subjected to different driving strengths η_h. The curves indicate a shift in the mean of the switching distribution and a reduction in its

[12] A quantile-quantile (or Q-Q) plot allows two distributions to be compared in a non-parametric manner by plotting the quantiles of one against the other. This has the property that if the two distributions are related by a linear transformation of the random variables, the Q-Q plot will display a straight line.

spread, both of which are expected for a switching distribution at a lower temperature [41, pp. 207–209].

This tendency is confirmed is Fig. 4.6(b) where the cumulative distribution function[13] (CDF) for the switching current is plotted for the same set of drivings. The distribution is shifted to higher values of the bias current with increasing driving, analogous to the shift that is observed for thermal curves with lowering temperature. The suppression of phase fluctuations in the interbilayer band thus corresponds to a measurable cooling effect on an experimentally relevant figure of merit.

Turning now to the systematic variation of the cooling with physical parameters, in Fig. 4.7(a) the relative phase fluctuations averaged over all modes in the interbilayer band are plotted as a function of α and γ_l for fixed γ_h. This indicates that optimal cooling occurs with a moderate coupling and weak intrinsic damping of the interbilayer plasmon. This conclusion qualitatively agrees with the picture of Fig. 4.3, there considering a single pair of linearised junctions.

Finally, we discuss the efficiency of cooling as a function of initial temperature, T_{initial}/T_0. At the lowest temperatures, the Josephson phase is confined to the harmonic region of the washboard potential. This is the region on which Sec. 4.2.2 was focussed. At higher temperatures when phase slipping becomes significant, a physically reasonable approach to measuring cooling efficiency is to compare the switching current distribution with the nearest thermal distribution. In particular, we have chosen to focus on comparing the means of the distributions. This is displayed in Fig. 4.7(b). In the inset, the relationship between the mean I_{switch} and the temperature T/T_0 is displayed for thermal stacks of 100 junctions. Then, in Fig. 4.7(b) we have taken driven systems with $\eta_h = 0.1$ at initial temperatures $\{T_{\text{thermal}}\}$, measured their switching current distribution mean and converted this into a temperature T_{driven} of the corresponding thermal state. The cooling ratio $T_{\text{driven}}/T_{\text{thermal}}$ is then evaluated and presented as a function of initial temperature. This slowly increases as T is reduced, consistent with the driving becoming increasingly off-resonant with the plasmon frequency difference around the typical switching current I_{switch}. In particular, there is no drop-off in cooling efficiency as the transition around $T \sim 0.15T_0$ is approached.

[13] If a random variable X has a probability distribution $P(X)$, then the cumulative distribution function $F_X(x)$ gives the probability that X takes a value of x or less, i.e. $F_X(x) = P(X \leq x)$.

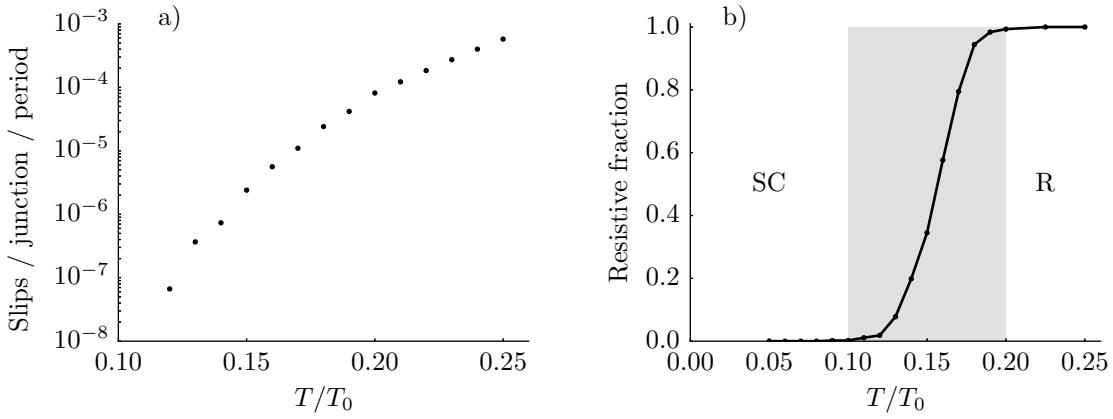

Figure 4.8: Temperature dependence of Josephson stack dynamics, in the absence of current bias. (a) A stack of 100 junctions is evolved in time for a total of 10^{-2} s (in parallel). The figure displays the count of the number of phase slips in a 100-junction unbiased Josephson stack, normalised by the number of junctions and Josephson plasma timescale. The phase slips are detected by the heuristic as discussed in the main text, Sec. 4.3.1. As the temperature is lowered, the number of spontaneous thermal phase slips decreases rapidly. (b) For the same simulation as in (a), the figure displays the fraction of trajectories that become resistive within a simulation time of 5 ns. To the left of the shaded region all trajectories remain superconducting (SC), while to its right, all trajectories rapidly become resistive (R). This is suggestive of a transition on these timescales between stable superconducting and spontaneous resistive behaviour as temperature is varied.

4.3.1 Temperature scale T_0

As a final section, we discuss the physical significance of the temperature scale T_0. Up till this point, T_0 has been defined in terms of the magnitude of the fluctuations $\langle\varphi_i^2\rangle$ ($\langle\varphi_i\rangle = 0$ in the unbiased case). Here we relate this temperature scale T_0 to the critical temperature of a stack. At sufficiently low temperature, the thermal fluctuations of the Josephson stack explore only the harmonic region of the washboard potential, while at higher temperatures there is sufficient energy for spontaneous thermal phase slips to occur. If in addition the stack is current-biased, the phase will continue to slip and the stack acquires a finite potential difference, becoming resistive.

In Fig. 4.8(a) we consider a stack of 100 junctions. The parameters used were

$\alpha = 1.0$, with the bottom of the two bands at 1 THz and 10 THz. The damping $\gamma_l = 0.05 \min(\omega_{l,i})$, $\gamma_h = 0.1 \min(\omega_{h,i})$. Across the temperature range $0.1 \leq T/T_0 \leq 0.25$, after the thermalisation burn-in we count the number of phase slips occurring in the stack, and normalise by the junction count and the Josephson period. Below $T/T_0 = 0.12$, zero phase slips occurred in the simulation time of 5 ns, across 2000 trajectories in parallel.

In Fig. 4.8(b) we apply a small bias $I_{\text{bias}}/I_c = 0.1$ and record the fraction of trajectories which have become resistive after a simulation time of 5 ns (comparable to the switching current calculations to be presented in Fig. 4.6, of $\Delta t = 1$ ns). We classify trajectories as superconducting or resistive by comparing whether the centre-of-mass phase is more than $\Delta\phi = 4\pi$ away from its value $\Delta t = 20$ ps ago. This simple heuristic is capable of capturing the resistive state effectively, and is not sensitive to modest variation of the parameters $\Delta\phi$ and Δt used. A region around $T/T_0 \sim 0.15$ is identified, which marks the onset of substantial thermal phase slipping behaviour. Thus by simulating our proposed scheme at $T/T_0 = 0.1$, we remain below this transitional range, but should also be at a sufficiently high temperature that a full quantum treatment of the dynamics is unnecessary.

4.4 Summary

We have investigated a scheme for cooling c-axis phase fluctuations in a bilayer cuprate, exploiting a variable inter-plasmon coupling to implement parametric cooling. We find that substantial cooling in the 40% region is theoretically possible, providing that the reheating rate of the Josephson phase is sufficiently low. Crucially, both oscillators must be underdamped for this mechanism to provide cooling at a rate competitive with reheating. We have studied a "toy" two-junction model, yielding good predictions of the numerics, and providing insight to the underlying mechanism: standard parametric cooling, but operating in the normal modes frame. Finally, we numerically studied a large system consisting of one hundred junctions, and have demonstrated that the cooling efficiency is similar to the toy model case, in the 30% region. The analysis and numerics indicate that the cooling process is optimised when the capacitive coupling strength $\alpha \sim 1$, suggesting that materials such as YBCO and the thallium-based bilayer cuprate TBCCO-2201 are likely to be optimal for experiments. Both contain IR-active phonon modes which are in the THz region and involve motion of the atoms around

the thin insulating layer found to be more effective for the parametric scheme. In YBCO these have been better explored experimentally. In comparison, the bilayer BSCCO-2212 has $\alpha \sim 0.1$, which is likely too weak for this effect to be observed.

This chapter has entirely focussed on the development of a cooling scheme in which thermal fluctuations are redistributed between the interlayer and intralayer modes. In the next chapter, we will examine the interaction between the Josephson phase and external electromagnetic fields with a view to the development of cooling schemes in which the thermal fluctuations of the Josephson phase are actively removed from the material.

5

Coupling the Josephson phase with a microcavity

In contrast to the previous chapter, in which our concern was upconversion and cooling with processes internal to the cuprate crystal, in this chapter we address the coupling between the Josephson phase and an external cavity mode. In Chapter 2 we reviewed the literature concerning this coupling. We concluded that the work of Bulaevskii and Koshelev [36] takes the most rigorous treatment, starting with the Josephson and Maxwell relations for the electrodynamics, however their restriction to analytic solutions severely limits the possible cavity geometries that they may consider. In this chapter we instead take a numerical approach, solving for the electrodynamics of the junction-cavity system, and from this we infer an effective coupled-oscillator model.

This chapter is structured as follows. We begin with an introduction to the finite element method (FEM) in the frequency domain, in the context of solving a travelling wave problem. In Sec. 5.1 we calculate the resonances of the microcavity array geometry introduced in Ref. [33]. In particular, the goal of these sections is to focus on the embellishments required in this class of problems (as opposed to typical first introductions which often solve the Laplace equation.)

In Sec. 5.2, we then convert the calculation of Refs. [36, 97] into a suitable form for the finite element method, enabling a detailed electromagnetic description of the coupling at the junction interface. We first perform a FEM calculation of a single junction and compare the resultant fields with the analytic results of Ref. [36]. We then move to the microcavity array geometry and examine the response of this system using the 'effective dielectric' model proposed by Laplace et al. [33]. In Sec. 5.3.2 we fit

a coupled-oscillator model to the FEM spectra and find evidence for a strong coupling with $g \sim 2.6$ THz.

5.1 Introduction to the finite element method

There is a large class of problems that fall into the category of computational electromagnetics (CEM). These mostly span engineering problems, concerning waveguides, antennae, resonant structures, and generally any problem requiring the numerical solution of Maxwell's equations in a non-trivial geometry. The text of Davidson [127] provides an introduction to this field, comparing the strengths and weaknesses of several methods for multiple problem classes. Those which make no physical approximations are termed "full-wave" techniques[1]. These include the finite-difference time domain (FDTD) approach, the method of moments, and the finite element method (FEM). Each approach has its unique strengths and weaknesses. Briefly, the FDTD approach samples the solution on a regular lattice, which is staggered for the electric and magnetic fields. This proves to be remarkably stable numerically, not suffering from the so-called "spurious modes" that plague naïve electromagnetic FEM calculations. However, the regular grid is inefficient for geometries that have features with lengthscales spanning multiple orders of magnitude (as in our case). The method of moments, also known as the boundary element method, maps the problem to an integral equation for surface currents over the boundaries (which must then be meshed). This is an excellent tool for scattering problems, naturally imposing the correct far-field boundary conditions. However, electromagnetically penetrable materials are problematic for this method, since equivalent volumetric currents must be used, negating the intended dimensionality reduction of this method.

In this section we introduce the finite element method and apply it to a simple travelling-wave problem in the frequency domain. This method provides a general and powerful approach to solving partial differential equations (PDEs) in up to three dimensions. A linear PDE is transformed into a large but sparse linear system which may be efficiently solved by standard methods. The discretisation of the domain is not as a regular grid, but as an arbitrary mesh allowing complex domains to be addressed.

[1] As a contrasting example, the method of geometric optics is not a full-wave technique, rather it is classed as an "asymptotic" technique in that approximations are made at the level of Maxwell's equations. Such methods based on physical approximations are often effective, but are only applicable in the region of validity of the underlying approximations.

The process of producing a suitable mesh concerns the field of computational geometry, and there are now several high-quality tools available such as Triangle [128], Gmsh [129], CUBIT [130] and others, many of which are commercial codes. In two dimensions, meshes are commonly constructed from triangles or quadrilaterals.

This section begins with a formulation of the toy problem, and introduces FEM in steps as required for this problem. In addition to Davidson [127], Pelosi, Coccioli, and Selleri [131] gives an alternative introductory view, while Jin [132] gives a more advanced treatment. The text of Hughes [133] is not specialised towards electromagnetic applications, but provides a detailed and extensive discussion of the underlying machinery. The approach taken in this chapter is that appropriate for a practitioner, rather than going into the subtle details and book-keeping needed to actually implement a FEM program from scratch; for such a level of detail, texts such as Hughes [133] are valuable.

5.1.1 Formulation

We consider the illumination of empty cavities in the geometry described in the introduction, which is schematically depicted in Fig. 5.1(a). While not an entirely general electromagnetic problem, this will be sufficient to introduce many aspects of FEM required for solving problems in this class. A source (marked Γ_2) produces light with wavevector $\vec{k} = -k\vec{z}$ and shines down onto the cavity array. The polarisation is such that the electric field is aligned along the x-axis, thus the magnetic field is aligned with the y-axis. Some light from Γ_2 is absorbed by the cavity modes, but eventually everything is reflected back up towards the top of the domain. The geometry is infinitely extended in the y direction to reduce this to a two-dimensional problem, for simplicity. We keep to the conventions of the finite element literature, and refer to the domain Ω [2] having boundary $\partial\Omega$ which may be broken up into several regions denoted Γ_i. The domain Ω is divided into two regions, Ω_{vacuum} and Ω_ϵ such that $\Omega = \Omega_{\text{vacuum}} \cup \Omega_\epsilon$. Ω_ϵ contains a dielectric of relative permittivity ϵ, while Ω_{vacuum} consists of a vacuum ($\epsilon = 1$). Thus in both regions the electric field $\vec{E}(x, z)$ and magnetic field $\vec{B}(x, z)$ obey

[2] In FEM calculations, explicitly denoting the domain in this way has notational advantages. We may write the boundary of the domain Ω as $\partial\Omega$, and integrals over the domain may be written $\int_\Omega d\Omega(\ldots)$.

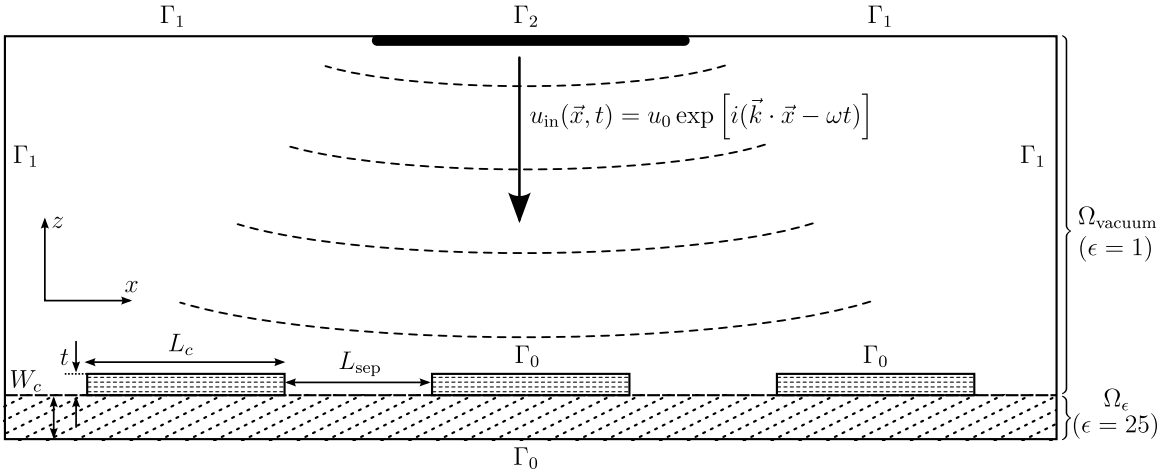

Figure 5.1: Schematic of the toy Helmholtz problem to be solved. A source region Γ_2 produces a monochromatic radiation field u_{in} from the top of the domain Ω. This has a wavevector $\vec{k}$ parallel to the (negative) z-axis, and is assumed to be polarised with the electric field aligned with the x-axis. This geometry and polarisation allows us to solve for a complex scalar field $u(\vec{x},t) := B_y(\vec{x},t)$ as the only non-zero component of the full vector magnetic field $\vec{B}$, simplifying the problem considerably. The field u_{in} is incident on an array of three metal strips sitting upon a dielectric region Ω_ϵ. These metal strips are modelled as holes in the domain, and their boundaries marked Γ_0 have the condition of zero transverse electric field. The boundary $\Gamma_1 \cup \Gamma_2$ is absorbing and intended to model a much larger domain by avoiding the reflection of waves. The regions beneath the metal strips are capable of supporting resonant modes in which a half-wavelength fits approximately the length L_c, this gives a fundamental mode at approximately $c/(2L_c\sqrt{\epsilon}) = 2.5$ THz for the parameters given.

the vector wave equation

$$\nabla^2\vec{E} - \frac{\epsilon(\vec{x})}{c^2}\frac{\partial^2}{\partial t^2}\vec{E} = \vec{0}, \quad \nabla^2\vec{B} - \frac{\epsilon(\vec{x})}{c^2}\frac{\partial^2}{\partial t^2}\vec{B} = \vec{0}, \tag{5.1}$$

and likewise for the magnetic field $\vec{B}$, where the dependence of ϵ on position is explicit. Owing to the geometry (including polarisation) chosen, we have $E_y = 0$ and $B_x = B_z = 0$. For this introductory example, we will solve the (scalar) wave equation for B_y,

$$\nabla^2 B_y - \frac{\epsilon(\vec{x})}{c^2}\frac{\partial^2}{\partial t^2}B_y = 0. \tag{5.2}$$

We could equally solve the vector equation for $\vec{E}$, or even the coupled electromagnetic system of equations arising directly from the Maxwell relations. However, solving for a

scalar field is the simplest option, both computationally and in terms of the complexity of the formulation. We will additionally rename the scalar field as u, for notational convenience.

The boundary conditions of the domain must be specified to complete the description of the problem. We treat the surfaces marked Γ_0 as perfect metals and thus the boundary condition is

$$\left.\begin{aligned} \vec{n} \times \vec{E}(\vec{x}, t) = \vec{0} \\ \vec{n} \times (\nabla \times \vec{B}(\vec{x}, t)) = \vec{0} \end{aligned}\right\} \quad \vec{x} \in \Gamma_0, \\ \text{i.e. } (\vec{n} \cdot \nabla) u = 0, \tag{5.3}$$

in which $\vec{n}$ is the outward normal on the boundary[3]. For the boundaries Γ_1, we would like these to effectively model a more extended domain which does not reflect at the perimeter. An approximation to this can be achieved with absorbing boundary conditions (ABCs) [131]. We note that a wave of the form $u_0 \exp(i(\vec{k} \cdot \vec{x} - \omega t))$ obeys the first-order equation

$$c\,(\vec{n} \cdot \nabla u) + \frac{\partial u}{\partial t} = 0, \tag{5.4}$$

provided that $\vec{n} \cdot \vec{k} = |\vec{k}|$, i.e. the wave is propagating in the direction $\vec{n}$. This is suitable for use as a boundary condition, although we should keep in mind that waves which are not normally incident will not satisfy this exactly leading to a partial reflection. We should therefore take this into account when designing the domain Ω. We can extend this boundary condition to describe our source region Γ_2, also. Here, the solution takes the form

$$u(\vec{x}, t) = u_{\text{out}} \exp\left(i(\vec{k} \cdot \vec{x} - \omega t)\right) + u_{\text{in}} \exp\left(i(-\vec{k} \cdot \vec{x} - \omega t)\right),$$

which satisfies the advection equation

$$c\,(\vec{n} \cdot \nabla u) + \frac{\partial u}{\partial t} = -2i\omega u_{\text{in}} \exp\left(i(-\vec{k} \cdot \vec{x} - \omega t)\right).$$

Finally, there is the internal boundary at the dielectric interface between Ω_{vacuum} and Ω_ϵ. The magnetic field there is continuous; nothing further needs to be done. An alternative to ABCs is to augment the physical domain with a perfectly matched layer (PML), which is a dissipative region impedance-matched such that there is no reflection

[3]The outward normal of a domain Ω always points away from its interior, and is locally perpendicular to the boundary $\partial\Omega$.

at the domain-PML interface [131]. The PML then needs to be of sufficient thickness that the reflection from the computational domain boundary is heavily attenuated before re-entering the physical domain. We do not make use of PMLs in this thesis, since ABCs are sufficient for the geometry of Chapter 5.

Since the problem is linear, it is simplest to solve in the frequency domain in which the Fourier transform $u(x,\omega) = \int dt\ u(x,t)e^{-i\omega t}$ obeys

$$\nabla^2 u(\omega) + k^2(\vec{x})u(\omega) = 0, \tag{5.5}$$

with $k(\vec{x}) = \sqrt{\epsilon(\vec{x})}\omega/c$. The boundary conditions become

$$\begin{aligned} (\vec{n}\cdot\nabla)u = 0 \qquad & x \in \Gamma_0, \\ c(\vec{n}\cdot\nabla)u - i\omega u = 0 \qquad & x \in \Gamma_1, \\ c(\vec{n}\cdot\nabla)u - i\omega u = -2i\omega u_{\text{in}} \qquad & x \in \Gamma_2. \end{aligned}$$

For the numerical solution of the problem, it is most straightforward to explicitly work with real-valued fields, and so we decompose the field $u \to v + iw$. In terms of v and w, the problem reads

$$\left.\begin{aligned} \nabla^2 v(\omega) + k^2 v(\omega) = 0, \\ \nabla^2 w(\omega) + k^2 w(\omega) = 0, \end{aligned}\right\} \ x \in \Omega, \tag{5.6}$$

$$\left.\begin{aligned} (\vec{n}\cdot\nabla)v = 0, \\ (\vec{n}\cdot\nabla)w = 0, \end{aligned}\right\} \ x \in \Gamma_0, \tag{5.7}$$

$$\left.\begin{aligned} c(\vec{n}\cdot\nabla)v + \omega w = 0, \\ c(\vec{n}\cdot\nabla)w - \omega v = 0, \end{aligned}\right\} \ x \in \Gamma_1, \tag{5.8}$$

$$\left.\begin{aligned} c(\vec{n}\cdot\nabla)v + \omega w = +2\omega\,\mathrm{Im}(u_{\text{in}}), \\ c(\vec{n}\cdot\nabla)w - \omega v = -2\omega\,\mathrm{Re}(u_{\text{in}}), \end{aligned}\right\} \ x \in \Gamma_2. \tag{5.9}$$

At this point, the mathematical problem has been fully specified. In FEM, we now discretise the domain Ω into cells over which we may express the solution as a piecewise function. Within each cell, the solution is constructed from a relatively small set of basis functions. Eq. (5.6) is known as the *strong form* of the problem; for FEM we require its *weak* or *variational* form. To reach this, we multiply the two lines of Eq. (5.6) by *test functions* $\bar{v}$ and $\bar{w}$ respectively and integrate over the domain. We

additionally integrate the $\nabla^2 v$ and $\nabla^2 w$ terms by parts[4] to reach

$$\begin{aligned} -\int_\Omega d\Omega\ \nabla\bar{v}\cdot\nabla v + \int_{\partial\Omega} d\Gamma\ \bar{v}(\vec{n}\cdot\nabla)v + \int_\Omega d\Omega\ k^2\bar{v}v = 0. \\ -\int_\Omega d\Omega\ \nabla\bar{w}\cdot\nabla w + \int_{\partial\Omega} d\Gamma\ \bar{w}(\vec{n}\cdot\nabla)w + \int_\Omega d\Omega\ k^2\bar{w}w = 0. \end{aligned} \tag{5.10}$$

In keeping with the finite element literature, we use $d\Omega$ to denote the differential volume element and $d\Gamma$ to denote the differential area element. In the weak form of the problem we solve for suitable *trial functions* $v \in V$ and $w \in W$ such that Eq. (5.10) holds for all valid choices of the test functions $\bar{v}$ and $\bar{w}$. V and W are suitable vector spaces, known as Sobolev spaces[5]. In this particular problem, the test function $\bar{v}$ should come from an identical space of functions as the trial function v.[6] In the following, we make statements about predominantly about v and $\bar{v}$; these equally apply to w and $\bar{w}$ since we will choose the same function space for v and w. This is based on the expectation that the real and imaginary parts of the solution should behave in similar ways, however in principle the spaces V and W can be chosen independently.

We now incorporate the boundary conditions in the weak form Eq. (5.10). The surface integral over $\partial\Omega$ becomes

$$\int_{\partial\Omega} d\Gamma \to \int_{\Gamma_0} d\Gamma + \int_{\Gamma_1} d\Gamma + \int_{\Gamma_2} d\Gamma,$$

each term of which may be replaced using the boundary conditions Eqs. (5.7–5.9). On the Neumann boundary Γ_0, $(\vec{n}\cdot\nabla)v = 0$ and so

$$\int_{\Gamma_0} d\Gamma\ \bar{v}(\vec{n}\cdot\nabla)v \to 0.$$

In the finite element literature, this is known as a natural boundary condition, in that it appears in the variational formulation. On the source boundary, we substitute in our expression for $(\vec{n}\cdot\nabla)v$ from Eq. (5.9) to give

$$\int_{\Gamma_2} d\Gamma\ \bar{v}(\vec{n}\cdot\nabla)v \to \int_{\Gamma_2} d\Gamma\ \bar{v}(-kw - 2ku_{\text{in}}),$$

[4]The identity $\int_\Omega d\Omega\ u\nabla^2 v = -\int_\Omega d\Omega\ \nabla u\cdot\nabla v + \int_{\partial\Omega} d\Gamma\ u(\vec{n}\cdot\nabla)v$ is a statement of Green's first identity and is exceptionally valuable in finite element derivations.

[5]In this particular example, V (and W) are instances of the Sobolev space $H^1(\Omega)$, which are intuitively described as containing functions v (and w) for which the integrals of v^2 and $|\nabla v|^2$ are finite over the domain Ω. Related to this, $H^1(\Omega)$ contains functions which are continuous, but may have discontinuous derivatives.

[6]This would not be the case if Dirichlet boundary conditions were present. There, the Dirichlet boundary conditions would be rendered homogeneous, but otherwise the function spaces would be identical.

where we have arbitrarily set the phase such that u_{in} is real. The absorbing boundary is obtained by setting $u_{\text{in}} = 0$ in the above. The entire weak form is

$$\begin{aligned} -\int_\Omega d\Omega\ \nabla\bar{v}\cdot\nabla v + \int_\Omega d\Omega\ k^2\bar{v}v - \int_{\Gamma_1\cup\Gamma_2} d\Gamma\ k\bar{v}w &= \int_{\Gamma_2} d\Gamma\ 2k\ \bar{v}u_{\text{in}}. \\ -\int_\Omega d\Omega\ \nabla\bar{w}\cdot\nabla w + \int_\Omega d\Omega\ k^2\bar{w}w + \int_{\Gamma_1\cup\Gamma_2} d\Gamma\ k\bar{w}v &= 0. \end{aligned} \tag{5.11}$$

It should be emphasised that this is a key result. In practice, once the problem is stated in this form, it can usually be directly translated into high-level FEM code, such as deal.II [134] or FEniCS [135]. However, we continue the discussion to make clear how the numerical solution of Eq. (5.11) proceeds.

Functions v and w which solve Eq. (5.11) will be exact solutions of Eq. (5.6) and satisfy the boundary conditions Eqs. (5.7–5.9). To make progress, we seek approximate solutions v_h and w_h which are constructed from basis functions

$$v_h = \sum_{j=1}^{N} V_j\bar{v}_j, \qquad w_h = \sum_{j=1}^{N} W_j\bar{w}_j, \tag{5.12}$$

weighted by the coefficients V_j, W_j. In FEM, this function basis is constructed by first discretising the domain into cells, on which local basis functions live. For this example, we will choose the set of order-q Lagrange (or continuous Galerkin) bases for simplicity, denoted as CG_q. These are simply the order-q polynomials defined on a triangle and may be characterised by the function value at $\frac{1}{2}(q+1)(q+2)$ points spaced on a grid overlapping the triangular cell. For example, for $q = 1$, there are 3 nodes coinciding with the vertices of the triangle. For $q = 2$, there are 6 nodes: the 3 vertices and the 3 edge midpoints. For third-order and higher, nodes internal to the cell are also required.

Thus each individual cell in the mesh has a local basis containing polynomials up to order q, specified implicitly by the value of the function at each of the $\frac{1}{2}(q+1)(q+2)$ points. These are the local degrees of freedom. The full space V_h is then a composition of these local spaces, where the local degrees of freedom are mapped to global degrees of freedom in V_h. At a common node between n cells, n local degrees of freedom are mapped to a single global degree of freedom. Likewise, along edges there are $2\times(q-1)$ local degrees of freedom from the two adjacent cells, which map to $(q-1)$ global degrees of freedom[7]. It is precisely this local-to-global mapping that enforces the continuity of the solution across the domain. It is a property of the CG_q finite elements we

[7]Note that this means that the global degrees of freedom live in a space whose dimension is non-

have chosen to use. In contrast, the Discontinuous Galerkin elements DG_q are only piecewise continuous and do not map the extremal local degrees of freedom onto shared global degrees of freedom. This allows for discontinuities in the solution, which can be useful for numerical stability (for example in linear advection [133]) and also for parallel solvers.

In Eq. (5.12), the symbols $\bar{v}_j$ and $\bar{w}_j$ were used for the basis functions, sharing the symbol of the test functions. This is deliberate: the test and trial functions share the same vector space, hence iterating $\bar{v}$ over the basis functions $\{\bar{v}_i\}$ ensures that Eq. (5.11) holds for all possible functions from this vector space. Explicitly,

$$\begin{aligned}\sum_{j=1}^{N} \int_\Omega d\Omega \, \Big(-\nabla\bar{v}_i \cdot \nabla\bar{v}_j + k^2 \, \bar{v}_i\bar{v}_j \Big) V_j - \sum_{j=1}^{N} \int_{\Gamma_1\cup\Gamma_2} d\Gamma \, \Big(k \, \bar{v}_i\bar{w}_j \Big) W_j \\ = \int_{\Gamma_2} d\Gamma \, 2k \, \bar{v}_i u_{\mathrm{in}}, \qquad (5.13)\\ \sum_{j=1}^{N} \int_{\Gamma_1\cup\Gamma_2} d\Gamma \, \Big(k \, \bar{w}_i\bar{v}_j \Big) V_j + \sum_{j=1}^{N} \int_\Omega d\Omega \, \Big(-\nabla\bar{w}_i \cdot \nabla\bar{w}_j + k^2 \, \bar{w}_i\bar{w}_j \Big) W_j = 0.\end{aligned}$$

By combining together the coefficients V_j and W_j as $\vec{U} = (\{V_j\}, \{W_j\})^T$, we see that the above is an instance of the linear system

$$A\vec{U} = \vec{L}, \qquad (5.14)$$

and may be solved by standard techniques. We can then calculate the solution $u(x, y)$ by evaluating Eq. (5.12), which will first involve a lookup step to identify the cell containing the point (x, y) and thus the relevant local basis functions.

To recapitulate what has been achieved here, the PDE Eq. (5.5) on a non-trivial domain has been transformed into a sparse linear system whose solution is straightforward. The key strength of the finite element method is that the matrix A is extremely sparse, as couplings between coefficients only occur on the lengthscale of the mesh

trivially set by the local basis functions *and* the choice of mesh. The product (number of mesh cells) $\times$ (local degrees of freedom per cell) gives a useful order-of-magnitude upper bound for the resulting problem size, however the exact number of global degrees of freedom very much depends on the mesh itself. For example, if at a point in the mesh n_{cells} triangular cells share a common vertex, n_{cells} local degrees of freedom will be mapped to a single global degree of freedom if CG_1 elements are used. The number n_{cells} may be arbitrarily large, precluding the possibility of writing any exact relation. The upper bound noted above is, however, extremely useful to estimate the computational expense of a particular problem.

cells. The manner in which these linear systems are solved depends on their symmetry properties. The most common case (e.g. for the Laplace equation, elasticity, fluid flow) is that the matrix A is symmetric positive definite. Direct methods such as Gaussian elimination and LU decomposition [136] are optimal for up to $N \sim 10^3$ – 10^4, however iterative methods such as preconditioned conjugate gradient solvers become more efficient for systems with $N \sim 10^5$ [8]. The latter is more commonly the case in a high-precision FEM calculation. Indeed, exploiting distributed solvers across multiple compute nodes, it is possible to solve systems with $N \sim 10^9$ [137]. This all arises because, provided that there is a finite upper bound on the number of nonzero entries in A, a matrix with N rows costs $\mathcal{O}(N)$ in storage and $\mathcal{O}(N)$ in matrix-vector multiplications.

In our particular case, A is non-symmetric preventing the use of conjugate gradient methods directly. Since our physical systems are two-dimensional, the resulting matrix problem is typically small enough to be tackled directly with sparse LU decomposition. However, there exist methods for either transforming the system into one that is symmetric (such as in CGN), or direct iterative methods such as that of generalised minimum residuals (GMRES) and those based on tridiagonal biorthogonalisation (such BCG, CGS and others). Trefethen and Bau III [136] provides a detailed introduction to these numerical algorithms.

5.1.2 Microcavity array

To complete our example, this physical problem has been solved for cavities of length $L_c = 12\ \mu$m having an approximate fundamental resonance at $\omega = \omega_1 \sim 2\pi c/(2L_c\sqrt{\epsilon}) = 2\pi \times 2.5$ THz, given that the dielectric under the cavities has relative permittivity $\epsilon = 25$. The cavity width is $W_c = 2.5\ \mu$m, and the cavities are separated by 12 μm. The mesh depicted in Fig. 5.2(a) was generated by the triangulation program Triangle [128], which offers useful features such as specification of maximum triangle area and minimum internal angles. The open-source package FEniCS [135] was used to assemble the linear system Eq. (5.13), which was then solved by the method of sparse

[8] For calculations in frequency space, the principal bottleneck is in fact memory with the largest non-distributed calculations completing on the order of minutes with modern hardware. On the other hand, the improved efficiency of iterative methods makes more of a difference in time domain problems where a FEM solution step is required for every time step, and the overall computation time can be substantially longer.

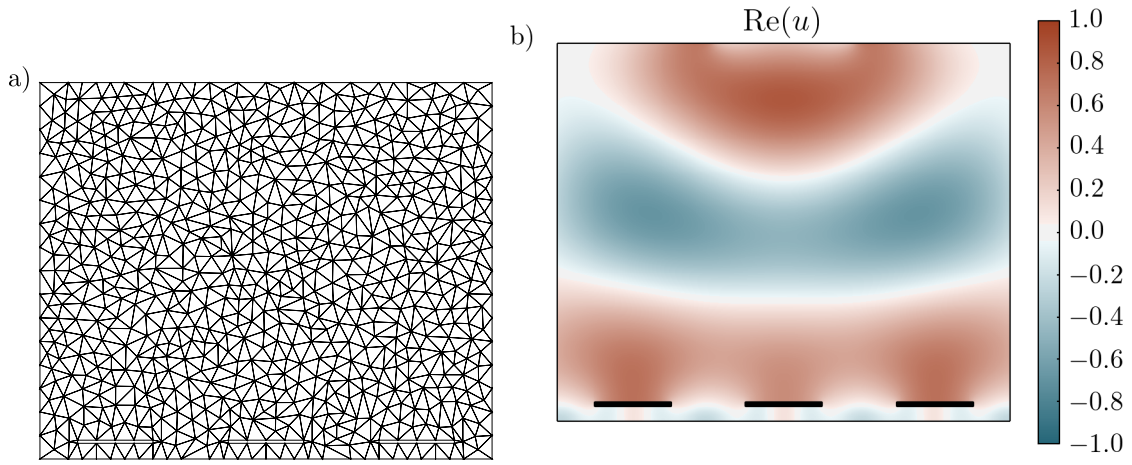

Figure 5.2: (a) An initial coarse mesh for the geometry of Fig. 5.1, containing 1363 cells and 735 vertices as generated by the program Triangle [128]. The domain is rectangular, however the metallic strips creating the cavity regions are achieved by creating *holes* in the domain. (b) FEM solution using CG_2 elements at $\omega = 2\pi \times 7$ THz, with dimensions $L_c = 12$ μm, $L_{\mathrm{sep}} = 12$ μm, $t = 0.5$ μm, $W_c = 2.5$ μm. The entire domain is 72×60 μm. This subfigure presents a contour plot of $\mathrm{Re}(u)$ to illustrate the full solution to Eq. (5.13) on a refined mesh containing 22276 cells. The linear system was solved using the sparse direct solver implementation in UMFPACK [138]. The source region at the top is clearly visible, as are the effects of diffraction and reflection from the edges, causing artefacts around the side cavities.

LU decomposition implemented in UMFPACK [138]. For larger systems, there exists the MUMPS package (MUltifrontal Massively Parallel sparse direct Solver) [139, 140]. In Fig. 5.2(b) the real part of the solution, $\mathrm{Re}(u)$, is shown for the entire domain at 7 THz, near the second harmonic of the cavities (7.5 THz). The source is clearly visible in the solution at the very top, with diffraction causing the wavefronts from the finite-size source to acquire a finite component k_x. This leads to partial reflection from the boundaries and various artefacts around the left and right cavity regions. There are at least two remedies to this problem. The first is to enlarge the domain Ω to minimise the effects of the boundaries, and the second is to extend the source to span the entire upper edge of the domain boundary $\partial\Omega$. The 'infinite' solution to this problem should be invariant under reflection about a cavity centre, and so placing a homogeneous Neumann boundary there will enforce this. Ideally, one should take both of these approaches and show that when well-constructed, the boundaries do not influence the

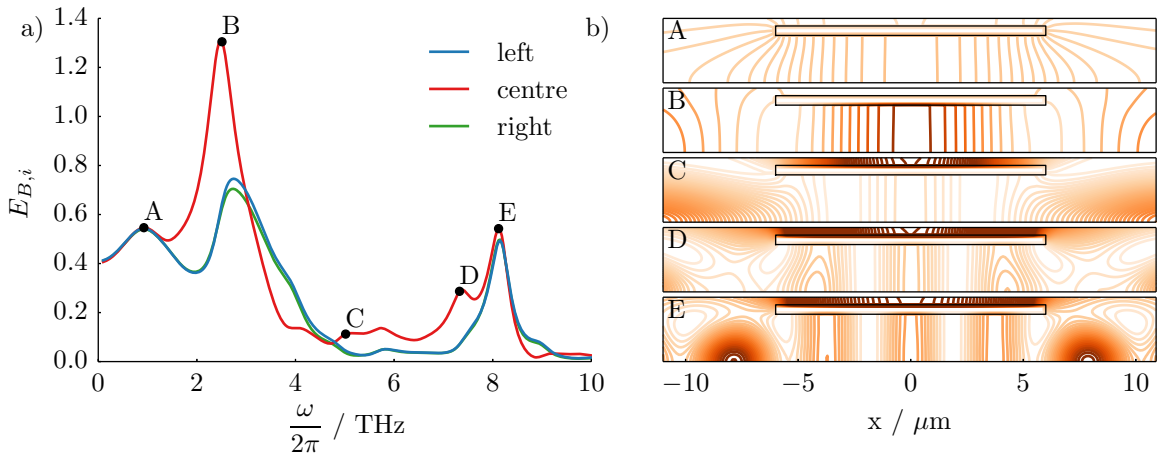

Figure 5.3: In (a), the energy density Eq. (5.15) is integrated over the cavity areas as a function of driving frequency ω, for the solution displayed in Fig. 5.2. The solution $|u|$ is displayed in (b) for the five points marked A–E. The colour scale on each subplot is the same, however the spacing of the contours is adjusted such that there are approximately ten underneath the cavity to highlight the mode structure. At the point B there is the fundamental resonance at $c/(2L_c\sqrt{\epsilon})$ = 2.5 THz. The first harmonic should be in the region of the point C, near 5 THz, but is missing due to symmetry: this mode has a π phase difference between the ends of the cavity, but this is incompatible with driving from directly above. The second harmonic is visible around the points D and E at approximately 7.5 THz. In addition to these cavity resonances, the peaks are split, most likely due to resonances *between* the cavities (visible at points C and E). In comparing the left, centre and right cavities we see differences arising from boundary effects. Additionally, the slight difference between the "left" and "right" cavities in (a) arises from the difference in meshing beneath the cavities.

solution obtained.

In Fig. 5.3, we calculate a more interesting quantity and examine the response of the cavities as a function of frequency. The frequency ω is specified as part of the matrix A, through k in Eq. (5.13). We focus on the magnetic component of the time-averaged

energy density[9], this is proportional to

$$E_{B,i} = \int_{\Omega_{\mathrm{cav},i}} d\Omega \; \tfrac{1}{2}\Big(\mathrm{Re}(u)^2 + \mathrm{Im}(u)^2 \Big), \tag{5.15}$$

in which the region of Ω directly beneath the i^{th} metal strip is denoted $\Omega_{\mathrm{cav},i}$. This is plotted for the three cavities in Fig. 5.3(a), where the boundary effects on the edge cavities are clearly visible. While the domain is left-right symmetric, differences between the left and right cavities can arise since the triangulation is not symmetric in general. In Fig. 5.3(b), the energy density is shown for each of the five points A–E labelled in (a). The fundamental mode is shown in B, in which a half-wavelength spans the cavity. D and E show the second harmonic, with three maxima in the energy density. The first harmonic should be observed at a frequency of approximately 5.0 THz, near C, although the symmetry of this mode requires a π phase difference between the ends of the cavity, which is unachievable given the geometry of the driving. In addition to the boundary effects, we see splitting of the cavity resonances, most likely due to resonances occurring *between* the cavities. With the cavities having been spaced 12 μm apart, their fundamental mode is expected to also be close to 2.5 THz.

5.2 Single Josephson junction radiation via the finite element method

Having introduced the finite element method for a purely electromagnetic problem in the previous section, we now consider applying this method to Josephson systems. As discussed in Chapter 2, the model of Bulaevskii and Koshelev [36] is well-suited as a starting point as it treats the coupling between Josephson oscillations and the external electromagnetic field directly. The interaction between the two is mediated through the interfacial boundary conditions at the edges of the junction. Approaching this with the finite element method, we will solve for the electromagnetic fields throughout the domain. This will enable us to advance to more complex geometries than those possible in the analytic treatment of Ref. [36].

Fig. 5.4(a) depicts the single junction geometry to be used. As before, we restrict our focus to a geometry infinitely extended along the y axis, thus reducing this to a two-

[9]The electric components (E_x, E_z) are derived from the gradient ∇B_y, and may also be efficiently calculated and integrated from the solution u.

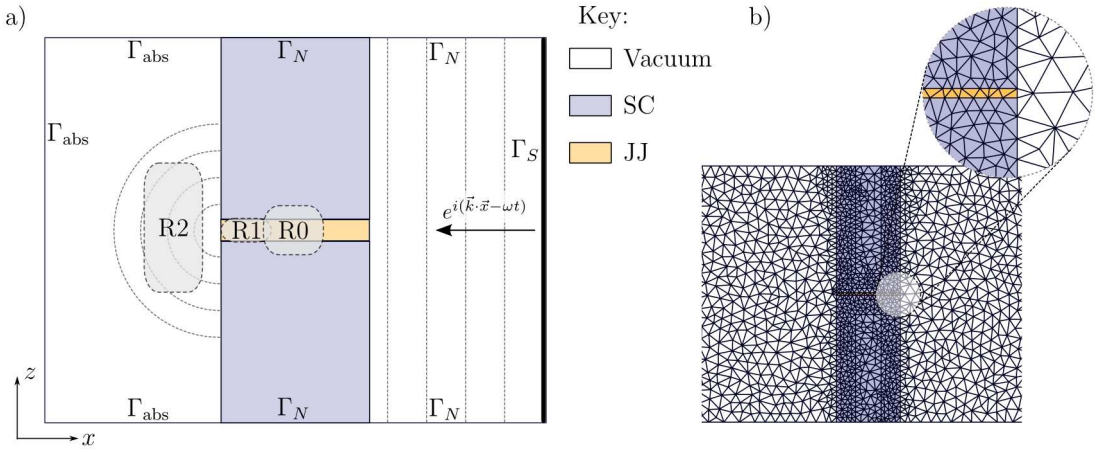

Figure 5.4: (a) Schematic of the single junction geometry. There is a driving/absorbing boundary Γ_S at the right, producing field oscillations in the adjacent vacuum region. A central region consisting of superconducting (SC) and Josephson (JJ) regions supports partial transmission of electromagnetic radiation, which may be emitted into the leftmost vacuum region. The boundaries $\{\Gamma_i\}$ are set as follows: Γ_S is a source/absorber, Γ_{abs} is solely absorbing and Γ_N is a Neumann boundary. The three regions R0–R2 denote domains over which the magnetic field will be integrated to measure the frequency-dependent response. The dashed lines in the vacuum region indicate the anticipated wavefronts due to driving at Γ_S. (b) A coarse, initial mesh for this geometry with regions at far left and right truncated. Regions are coloured as in (a).

dimensional problem in the xz plane. It is then possible to solve for the y component of the magnetic field $\vec{B}$, just as in Sec. 5.1.1. In the vacuum regions $B_y(\omega)$ satisfies

$$\nabla^2 B_y(\omega) + k^2 B_y(\omega) = 0,$$

which is a wave-like Helmholtz equation. As discussed in Sec. 2.3.2, in the superconducting regions (marked "SC") $B_y(\omega)$ satisfies

$$\nabla^2 B_y(\omega) - \frac{1}{\lambda_\omega^2} B_y(\omega) = 0,$$

where $\lambda_\omega^{-2} = 1/\lambda_{ab}^2 - \epsilon_s \omega^2/c^2 - i\omega\sigma_q/\epsilon_0 c^2$, λ_{ab} is the London penetration depth, ϵ_s is an effective dielectric constant of the superconductor, and σ_q is the contribution to the conductivity due to dissipative currents in the superconductor. The dielectric Josephson region (marked "JJ") requires more careful consideration. From the formulation of

Ref. [36],

$$\nabla^2 B_y - \frac{1}{\lambda_\omega^2} B_y = \frac{\Phi_0}{2\pi\lambda_{ab}^2} \partial_x \phi(x,\omega)\ \delta(z), \tag{5.16}$$

indicating how the Josephson phase provides a driving term for the magnetic field. Additionally, from the Maxwell relations we can identify the independent relation

$$\partial_x B_y = J_c \left(\frac{\omega^2}{\omega_p^2} - 1 + i\omega\beta \right) \phi, \tag{5.17}$$

where $\beta = (\Phi_0/2\pi)(\sigma/DJ_c)$ has dimensions of time and is proportional to the damping due to the junction conductivity σ. We find that eliminating $\phi(x,\omega)$ from Eqs. (5.16, 5.17) gives the following equation for B_y,

$$\left[1 - \frac{\lambda_J^2}{\lambda_{ab} D} \left(\frac{\omega^2}{\omega_p^2} - 1 + i\omega\beta \right)^{-1} \right] \partial_x^2 B_y + \partial_z^2 B_y - \frac{1}{\lambda_\omega^2} B_y = 0, \tag{5.18}$$

where λ_J is the Josephson lengthscale defined by $\lambda_J^2 = \Phi_0/2\pi\mu_0 J_c(2\lambda_{ab}+D)$. Note that in the absence of damping ($\beta \to 0$) the divergence of the x-lengthscale causes singular behaviour as $\omega \to \omega_p$. Physically the damping will remain finite, but one should be aware of the possibility of numerical instabilities at low damping[10]. We compose the weak form in precisely the same manner as explained in Sec. 5.1. The only additional complication is the appearance of a boundary term between the JJ region and the vacuum. This occurs from the replacement we make via Green's first identity,

$$\int_\Omega d\Omega\ f\nabla^2 g = -\int_\Omega d\Omega\ \nabla f \cdot \nabla g + \int_{\partial\Omega} d\Gamma\ f(\vec{n}\cdot\nabla)g.$$

Between regions the prefactor f is typically constant, thus the terms $\int_{\partial\Omega} d\Gamma\ f(\vec{n}\cdot\nabla)g$ from each side of the boundary will be equal in magnitude but have oppositely-directed outward normals $\vec{n}$, and so will cancel. This will not be the case when Eq. (5.18) interfaces with a term $\nabla^2 B_y$, and so there arises a boundary term

$$\frac{\lambda_J^2}{\lambda_{ab} D} \left(\frac{\omega^2}{\omega_p^2} - 1 + i\omega\beta \right)^{-1} \int d\Gamma\ \bar{u}\ \big(\vec{n}\cdot\nabla\big)u,$$

where the domain of integration is the boundary between the JJ and vacuum regions. This section has outlined our approach to converting the Josephson system into a form suitable for use with the finite element method; in the next section we explore the electrodynamics of the single junction numerically to verify that it yields a correct physical picture.

[10] One could multiply through by the factor $\big(\omega^2/\omega_p^2 - 1 + i\omega\beta\big)$, although it turns out that in the finite element formulation this causes further problems related to surface terms that arise along the perimeter of the Josephson region.

5.2.1 Numerical results

There are two principal ways in which we may numerically extract physical information about the system. In the first of these, we can define regions of interest in the domain, calculate the time-averaged integrated energy density (or other quantity of interest) and plot these as a function of driving frequency. This gives a sense for the spectral response of the system. Defining multiple regions of integration also helps overcome the ambiguity in defining each oscillator. For example, even in the case of the bare cavity, the cavity volume is ill-defined. By comparing the integrals on multiple regions we may determine the sensitivity of the results to the region choice. Our second tool is to examine the solution across the entire domain at particular frequencies of interest.

Fig. 5.5(a) displays the energy $E(\omega) = \int d\Omega \, |B_y|^2/2\mu_0$ where the regions of integration are depicted in Fig. 5.4(a). With energy plotted on a logarithmic scale, vertically displaced curves represent functions which have identical ω-dependence but differing prefactors. The three spectra in Fig. 5.5(a) are similar, indicating that the measure is robust against the choice of integration region. While not at all physical for an artificial Josephson junction (in which frequencies in the GHz range would be more usual), this is a more useful test of the calculation in anticipation of working in the microcavity scenario. This enables us to determine the stability of the FEM scheme given the discretisation scale, choice of finite elements, and so forth.

Fig. 5.5(b) presents the solution throughout the domain and the cross-section along the junction and out to the left boundary. These correspond to the three frequencies of interest marked in (a). At the plasmon frequency ω_p, there is no visible response in the spectrum, and the solution (b)A shows only weak penetration into the JJ region. This is consistent with the results of Ref. [36], in which Eq. (12) gives the boundary condition connecting $\phi(x, \omega)$ with B_y at the junction edge, namely

$$\partial_x \phi(x, \omega)\Big|_{\text{edge}} \approx -\frac{\lambda_{ab}}{\lambda_\omega} \frac{4\pi\lambda_{ab}}{\Phi_0} B_y(\omega)\Big|_{\text{edge}}.$$

On resonance, we expect $\phi(x, t) \sim e^{i\omega_p t}$ which is spatially constant and therefore $B_y = 0$ at the edges. From the perspective of Ref. [36] in which Josephson oscillations radiate at their boundaries, the $k = 0$ mode cannot radiate within the approximations of their analysis. Equivalently, the external electromagnetic drive cannot excite this mode. Moving to the modes B and C portrayed in Fig. 5.5(b), these correspond to the first two finite k modes of the junction. Defining x_0 to be the x coordinate of

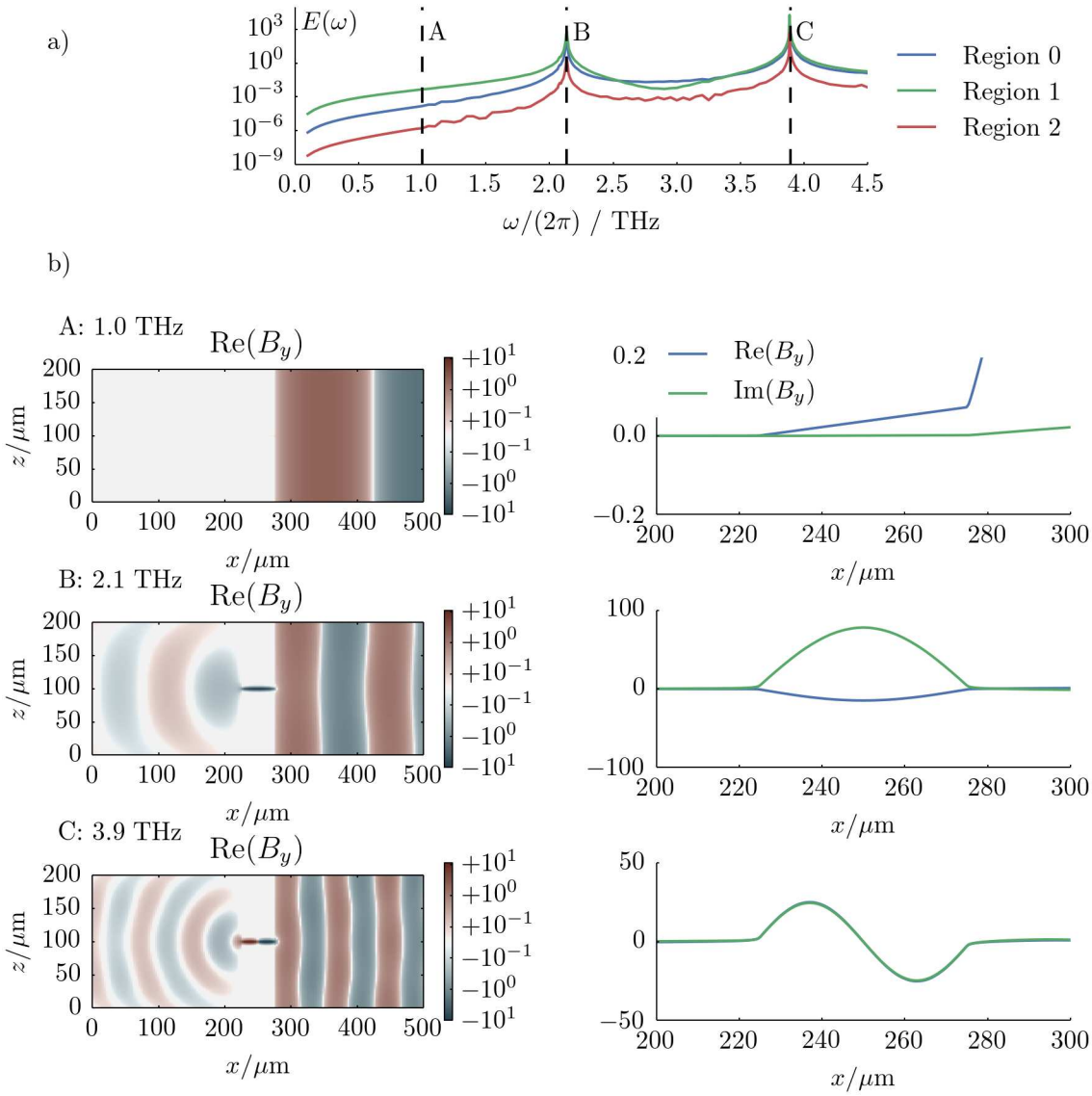

Figure 5.5: (a) Frequency dependence of the energy $E(\omega) = \int d\Omega\ |B_y|^2/2\mu_0$ (in dimensionless units) over the three integration regions R0–R2 marked in Fig. 5.4. The calculation parameters were $\omega_p = 2\pi \times 1$ THz, and D, λ and λ_J chosen to produce $\omega_1 \sim 2\pi \times 2.1$ THz. After triangulating the mesh, CG_2 elements were used to approximate individually the real and imaginary parts of the complex solution space. Both regions R0 and R1 are around the Josephson region, while region R2 is in the left vacuum region and measures the field being transmitted through the junction. (b) Left: Plots of $\mathrm{Re}(B_y)$ throughout the FEM domain. The impedance matching at the junction–vacuum interface is poor, leading to the field in the left vacuum region being orders of magnitude smaller than at the source. To plot this, $\mathrm{Re}(B_y)$ has been transformed onto a custom logarithmic scale as indicated by the legend. Right: Cross-sections of $\mathrm{Re}(B_y)$ and $\mathrm{Im}(B_y)$ along the line $z = 100$ μm. The approximate Dirichlet boundary conditions for B_y translate to approximate Neumann boundary conditions for the phase $\phi(x, \omega)$, as expected.

the left side of the junction, we see from Eq. (5.17) that as $B_y \sim \sin(n\pi(x-x_0)/L_c)$, $\phi \sim \cos(n\pi(x-x_0)/L_c)$, satisfying the Neumann boundary conditions for the phase as $\partial_x\phi(x=0) = \partial_x\phi(x=x_0) = 0$. For these harmonics, there is no approximate node in the magnetic field at the junction edge, allowing for energy transfer and coupling between the Josephson phase and the external field.

5.3 Microcavity array via the finite element method

In this section we turn to the main focus of this chapter, calculating the effective coupling in a microcavity array geometry as depicted in Fig. 5.6. First, we examine the calculation of Laplace et al. [33] in which this system is modelled with an anisotropic, frequency-dependent permittivity tensor, and develop a FEM description of this problem. In Sec. 5.3.1 we present the numerical results. We then draw on the output of this model in Sec. 5.3.2 where we propose the most simple two-oscillator Hamiltonian and fit its parameters to reproduce their spectra.

In Fig. 5.6(a) we show the envisioned experimental geometry, and a two-dimensional approximation of this displayed in (b). There is an underlying substrate, upon which layers of dielectric, cuprate, dielectric, and finally metal are deposited. As indicated, the SC layer may be modelled in one of two ways depending on the method, either that of Ref. [33] (Sec. 5.3.1) or the explicit Josephson layers (for future work).

In this section we approach the microcavity array from the effective dielectric model described in Laplace et al. [33]. The entire cuprate region is modelled using the permittivity tensor

$$\epsilon = \begin{pmatrix} \epsilon_\infty & 0 & 0 \\ 0 & \epsilon_\infty & 0 \\ 0 & 0 & \epsilon_\infty(1-\omega_p^2/\omega^2) \end{pmatrix}, \tag{5.19}$$

which is expected to provide an accurate description of the electrodynamics of the cuprate, specifically including the anisotropy of the layered structure and the internal supercurrent. The parameter ϵ_∞ gives the dielectric response in the x and y directions, and that in the z direction when $\omega \gg \omega_p$. The frequency ω_p is the c-axis Josephson frequency for the cuprate. Note the vanishing of the permittivity ϵ_{zz} as $\omega \to \omega_p$. Given the tensor permittivity, it does not seem possible to reduce Maxwell's equations to an equation for the scalar field B_y. From the two-dimensional simplification of

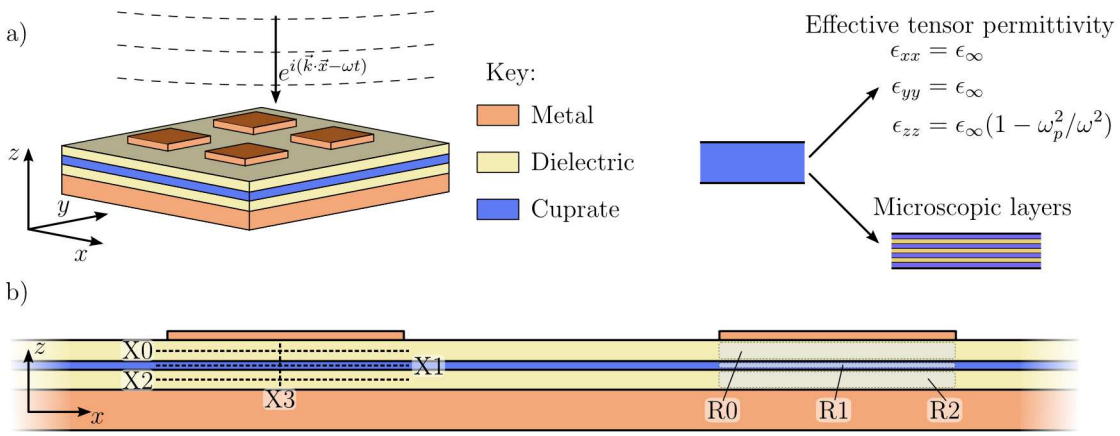

Figure 5.6: (a) Proposed experimental geometry in which a sandwich of dielectric, cuprate and dielectric layers is deposited onto a metal substrate. Metal stripes are placed above to form microcavities. (b) We will approximate the three-dimensional geometry with this two-dimensional cross-section. This geometry is very similar to that studied in the example in Sec. 5.1.1. Depending on the model, the SC layer is modelled either as a bulk effective dielectric, or is resolved into many sub-layers marked as either SC or JJ. The regions R0–R2 are regions of integration defined here for future reference. Likewise, the lines X0–X3 are cross-sections through the geometry.

the geometry, we can instead work with the electric field $\vec{E} = (E_x, 0, E_z)$. From the Maxwell equations and the anisotropic permittivity in the cuprate region described by Eq. (5.19), we may write the strong form of the FEM problem as

$$\begin{aligned}
\nabla \times (\nabla \times \vec{E}) - \frac{\omega^2}{c^2}\vec{E} &= \vec{0}, \quad \vec{x} \in \Omega_{\text{vac}}, \\
\nabla \times (\nabla \times \vec{E}) - \epsilon\frac{\omega^2}{c^2}\vec{E} &= \vec{0}, \quad \vec{x} \in \Omega_{\epsilon}, \\
\nabla \times (\nabla \times \vec{E}) - \frac{\omega^2}{c^2}\vec{\epsilon}\vec{E} &= \vec{0}, \quad \vec{x} \in \Omega_{\text{SC}}, \\
\vec{n} \times \vec{E} &= 0, \quad \vec{x} \in \Gamma_D, \\
-ik\ \vec{n} \times \vec{E} + \nabla \times \vec{E} &= -2ik\vec{n} \times \vec{E}_{\text{in}} \exp(-i\vec{k} \cdot \vec{x}), \quad \vec{x} \in \Gamma_S,
\end{aligned} \tag{5.20}$$

where Ω_{vac}, Ω_ϵ and Ω_{SC} are the vacuum, dielectric and cuprate regions respectively, Γ_D is the Dirichlet boundary on metallic surfaces (as well as the side walls, by symmetry) and Γ_S is the source region. In the subdomain Ω_ϵ, ϵ is the (scalar) permittivity, here

taken to be $\epsilon_\infty = 25$. In the subdomain $\Omega_{\rm SC}$, ϵ is the tensor permittivity defined in Eq. (5.19).

The first stage in converting the strong form above into a suitable weak form is to perform an integration by parts on the $\nabla \times (\nabla \times \vec{E})$ term above. For generality, consider the PDE

$$\nabla \times (\nabla \times \vec{E}) + \frac{1}{c^2}\epsilon \frac{\partial^2}{\partial t^2}\vec{E} = -\mu_0 \frac{\partial}{\partial t}\vec{J},$$

which assumes that the permittivity ϵ is a constant tensor and that there may be a finite current $\vec{J}$. To incorporate dissipation, we will assume a simple Ohmic relation $\vec{J} = \sigma \vec{E}$. Taking the Fourier transform, we reach

$$\nabla \times (\nabla \times \vec{E}) - \left(\epsilon \frac{\omega^2}{c^2} + i\omega\mu_0\sigma\right)\vec{E} = 0.$$

As should be familiar by now, we split the field $\vec{E}$ into real and imaginary parts $\vec{v} + i\vec{w}$, multiply by test functions $\vec{v}$ and $\vec{w}$ and integrate over the domain, giving

$$\begin{aligned} \left(\vec{v}, \nabla \times (\nabla \times \vec{v})\right)_\Omega - \frac{\omega^2}{c^2}\left(\vec{v}, \epsilon\vec{v}\right)_\Omega + \omega\mu_0\sigma\left(\vec{v}, \vec{w}\right)_\Omega = 0, \\ \left(\vec{w}, \nabla \times (\nabla \times \vec{w})\right)_\Omega - \frac{\omega^2}{c^2}\left(\vec{w}, \epsilon\vec{w}\right)_\Omega - \omega\mu_0\sigma\left(\vec{w}, \vec{v}\right)_\Omega = 0. \end{aligned} \tag{5.21}$$

We now perform integration by parts on the first term, which makes the replacement

$$\int_\Omega d\Omega\ \vec{f} \cdot \nabla \times (\nabla \times \vec{g}) = \int_\Omega d\Omega\ (\nabla \times \vec{f}) \cdot (\nabla \times \vec{g}) - \int_{\partial\Omega} d\Gamma\ (\vec{n} \times \vec{f}) \cdot (\nabla \times \vec{g})$$

for arbitrary vector fields $\vec{f}$ and $\vec{g}$. The triple scalar product in the boundary term has been re-ordered to read as an inner product between test and trial functions. Finally, the boundary term $(\vec{n} \times \vec{f}, \nabla \times \vec{g})_{\partial\Omega}$ needs to incorporate the domain boundary conditions. On a perfectly conducting surface, the field $\vec{E}$ satisfies $\vec{n} \times \vec{E} = 0$, i.e. it has zero tangential component. On absorbing or source boundary regions, we can generalise the discussion of Sec. 5.1 to find that the field $\vec{E}$ obeys

$$-ik\ \vec{n} \times \vec{E} + \nabla \times \vec{E} = -2ik\vec{n} \times \vec{E}_{\rm in} \exp(-i\vec{k} \cdot \vec{x}),$$

where $k = \omega/c$ and $\vec{E}_{\rm in}$ is the incident field vector on Γ_S. Recall from Sec. 5.1 that such absorbing boundary conditions only absorb the component of with $\vec{k}$ perpendicular to the boundary; any parallel component will be reflected. Putting it all together, the weak form for the effective dielectric model is given by

$$\begin{aligned} \left(\nabla \times \vec{v}, \nabla \times \vec{v}\right)_\Omega - \frac{\omega^2}{c^2}\left(\vec{v}, \epsilon\vec{v}\right)_\Omega + \omega\mu_0\sigma\left(\vec{v}, \vec{w}\right)_\Omega - \frac{\omega}{c}\left(\left(\vec{v} \cdot \vec{n}, \vec{w} \cdot \vec{n}\right)_{\Gamma_S} - \left(\vec{v}, \vec{w}\right)_{\Gamma_S}\right) \\ = \frac{2\omega}{c}\left(\left(\vec{v} \cdot \vec{n}, \vec{w}_{\rm in} \cdot \vec{n}\right)_{\Gamma_S} - \left(\vec{v}, \vec{w}_{\rm in}\right)_{\Gamma_S}\right), \end{aligned} \tag{5.22}$$

$$\left(\nabla\times\vec{w},\nabla\times\vec{w}\right)_\Omega-\frac{\omega^2}{c^2}\left(\vec{w},\epsilon\vec{w}\right)_\Omega-\omega\mu_0\sigma\left(\vec{w},\vec{v}\right)_\Omega+\frac{\omega}{c}\left(\left(\vec{w}\cdot\vec{n},\vec{v}\cdot\vec{n}\right)_{\Gamma_S}-\left(\vec{w},\vec{v}\right)_{\Gamma_S}\right)$$
$$=-\frac{2\omega}{c}\left(\left(\vec{w}\cdot\vec{n},\vec{v_{\text{in}}}\cdot\vec{n}\right)_{\Gamma_S}-\left(\vec{w},\vec{v}_{\text{in}}\right)_{\Gamma_S}\right), \quad (5.23)$$

where the tensor ϵ and conductivity σ are piecewise functions on the current subdomain.

In this geometry, the electric field $\vec{E}$ lives in a two-dimensional space. There are various possible finite elements that could be used in discretising the weak form Eqs. (5.22, 5.23). The most basic approach would use scalar Lagrange elements CG_q for the two components of the electric field. While the calculation can proceed, it turns out that this is a rather poor choice since the electromagnetic field has significantly more structure than a tensor product of scalar elements can express. For example, at a dielectric interface, $\vec{n}\times\vec{E}_1=\vec{n}\times\vec{E}_2$; only the tangential component of the vector field is continuous. Furthermore, naïve Lagrange CG_q (or indeed any scalar) elements do not enforce the zero divergence condition $\nabla\cdot\vec{E}=0$ in the absence of free charge. This leads to the "spurious modes" problem which plagued early applications of FEM to computational electromagnetics [127].

The solution is to make use of finite elements which preclude these unphysical solutions from the outset. The Nédélec finite elements (of which there is a first kind [141] and a second kind [142]) do precisely this. These are introduced as three-dimensional elements, however they have two-dimensional analogues in common use. These elements are $H(\mathrm{curl})$-conforming[11], in which $H(\mathrm{curl})$ is a Sobolev space, meaning that they have a continuous tangential component between cells[12].

5.3.1 Effective tensor dielectric model

Having set up the formulation, we are now in a position to perform calculations on this system. In Fig. 5.7(a), we have plotted the integral of the energy density as a function of driving frequency for microcavity arrays both with and without the cuprate layer. The regions of integration are labelled in Fig. 5.6. Fig. 5.7(b) indicates the electric field with arrows as well as the energy density with shading at three points of interest marked on (a). With no SC layer in the cavity, there is a single resonance at the

[11]Note that Refs. [141, 142] also introduce $H(\mathrm{div})$-conforming elements, which are appropriate for vector fields with a continuous *normal* component between cells.

[12]Contrast this against the CG_q elements introduced in Sec. 5.1, in which the nodal degrees of freedom constrained the scalar field to be continuous between cells.

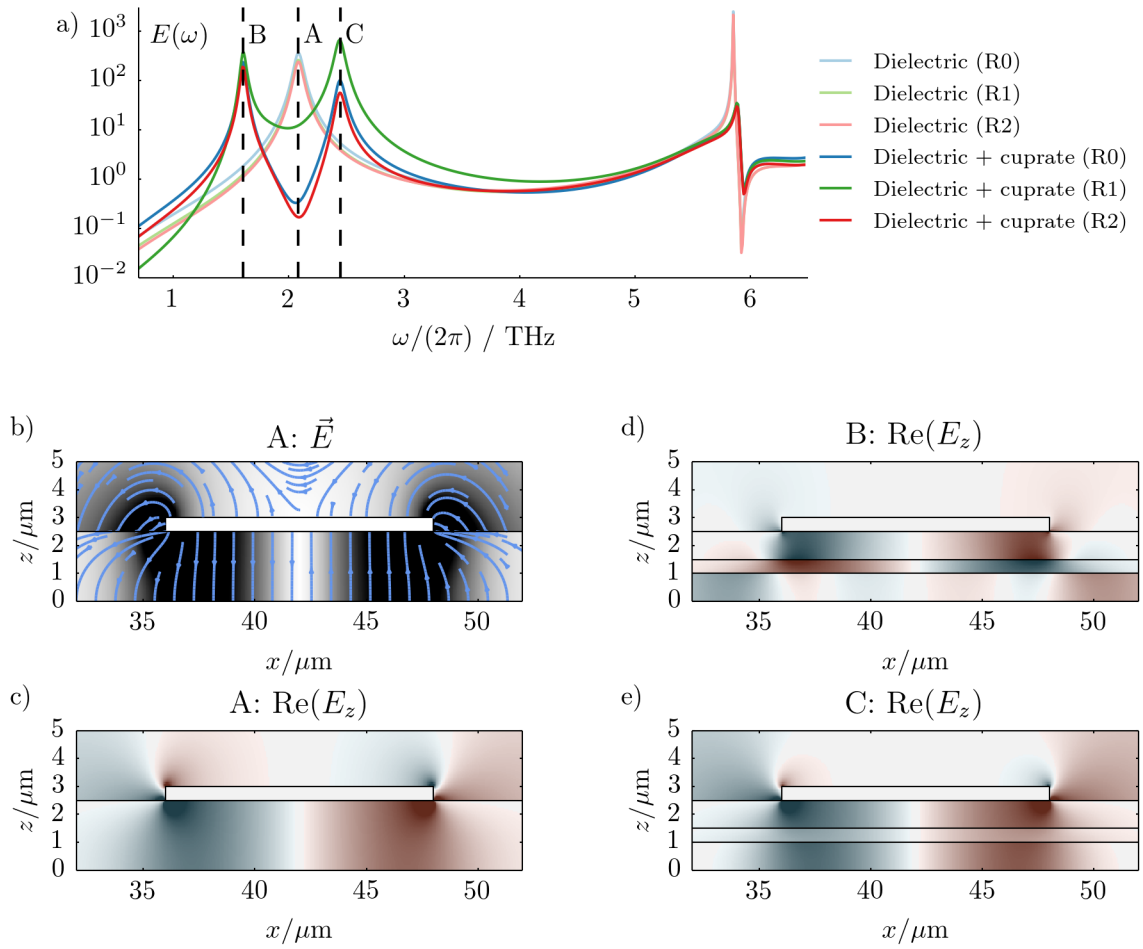

Figure 5.7: A study of the effective dielectric model Eqs. (5.22, 5.23) in the cavity array geometry. After triangulating the mesh, the solution space is approximated with Nédélec elements of the first kind (and quadratic order) for the real and imaginary parts. (a) Response of the cavity mode as a function of ω, where the cavity contains dielectric only (pale lines) or an SC layer (dark lines). The regions of integration are as labelled in Fig. 5.6. Note that we should not expect the response in regions R0 and R2 to be symmetric, since one is at the top of the cavity, the other at the bottom, and the driving/geometry is not symmetric with respect to the two regions. (b) Electric fields around the cavity region at the resonance marked (A) in the absence of the SC layer. The arrows indicate the direction of the electric field at throughout the region, while the shaded intensity is proportional to the energy density $\int d\Omega \ \left(|E_x|^2 + |E_z|^2\right)$. (c–e) The z-component of the electric field at the resonances (A), (B) and (C) respectively. The cavity mode at (A) consists of antinodes at the cavity edges, with a node in the centre. The two resonances (B) and (C) correspond to anti-phase and in-phase combinations of the SC and surrounding dielectric regions.

cavity frequency ~ 2.1 THz, plus higher harmonics. Fig. 5.7(c) shows that this cavity mode fits a half-wavelength into the cavity length, with maxima in $|\vec{E}|$ at both ends and a node at the centre. Including an SC layer with $\omega_p = 2\pi \times 2.1$ THz, there is a substantial splitting of the cavity peak into a pair separated by approximately 0.9 THz. The lower and upper peaks are plotted in Fig. 5.7(d) and (e) respectively. We see that these correspond to anti-phase and in-phase oscillations of the SC layer with respect to the cavity. In Sec. 5.3.2 we will fit a simple two-oscillator Hamiltonian to these spectra to infer the physical parameters of the oscillators, including their coupling strength. Additionally, whether the fit is possible indicates the suitability of a pair of linearly-coupled oscillators as a toy model for this system.

5.3.2 Fitting a model Hamiltonian

In this final section, we address the problem of interpreting the spectra in this chapter in terms of coupled oscillators, and specifically the coupling strength. The approach is simple: we take a plausible Hamiltonian for two coupled oscillators and determine which physical parameters best describe the observed spectra. From the quality of the fit we may determine whether the proposed Hamiltonian appropriately describes the FEM model, or whether additional terms are required.

We begin by proposing the simplest of coupled Hamiltonians,

$$H = \frac{p_c^2}{2m_c} + \tfrac{1}{2}m_c\Omega_c^2 x_c^2 + \frac{p_p^2}{2m_p} + \tfrac{1}{2}m_p\omega_p^2 x_p^2 + G x_c x_p, \tag{5.24}$$

i.e. that of two linearly coupled oscillators. The cavity mode analogue has position x_c, momentum p_c, frequency Ω_c and the Josephson plasmon analogue has position x_p, momentum p_p and frequency ω_p. The linear coupling between the oscillators is of strength G. This is a classical Hamiltonian, although quantising and writing in ladder operators is also useful, in which case we write

$$\hat{H} = \hbar\Omega_c \hat{a}^\dagger \hat{a} + \hbar\omega_p \hat{b}^\dagger \hat{b} + \hbar g\big(\hat{a} + \hat{a}^\dagger\big)\big(\hat{b} + \hat{b}^\dagger\big), \tag{5.25}$$

where $\hat{a}$ and $\hat{b}$ are the ladder operators for oscillators c and p respectively, and the coupling g is a frequency given by

$$g = \sqrt{\frac{G^2}{4m_c m_p \Omega_c \omega_p}}.$$

Since g is a rate, it may be directly compared with the oscillator frequencies Ω_i and damping rates γ_i. Oscillators c and p represent the cavity and Josephson modes respectively. We assume both to be damped, and only the cavity mode is driven. This gives rise to the classical dynamics

$$\begin{aligned}
\partial_t x_c &= \frac{p_c}{m_c}, \\
\partial_t p_c &= -m_c \Omega_c^2 x_c - \gamma_c p_c - G x_p + F(t), \\
\partial_t x_p &= \frac{p_p}{m_p}, \\
\partial_t p_p &= -m_p \omega_p^2 x_p - \gamma_p p_p - G x_c,
\end{aligned}$$

in which $F(t)$ has been introduced as the force driving the cavity oscillator, and γ_c and γ_p as the damping rates of the two oscillators. Since the FEM calculations are performed in the frequency domain, it is appropriate to treat $F(t)$ as a monochromatic driving $F_0(\omega)\exp(i\omega t)$. Furthermore, since the FEM boundary conditions produced incident oscillations of fixed amplitude, we can treat F_0 as being a constant, independent of ω. Thus, given the set of physical parameters $\mathcal{P} = \{m_c, m_p, \Omega_c, \omega_p, \gamma_c, \gamma_p, G, F_0\}$ we may compute quantities such as $\langle x_c^2(\omega)\rangle$ and $\langle x_p^2(\omega)\rangle$, in which the frequency-dependence is made explicit. These are related to meaningful physical quantities, for example $\langle \frac{1}{2} m_c \Omega_c^2 x_c^2\rangle$ corresponds to the mean potential energy of the cavity mode. If the model is suitable, we expect $\langle \frac{1}{2} m_c \Omega_c^2 x_c^2\rangle$ to take a similar ω-dependence to quantities such as $\int d\Omega \frac{1}{2} B_y^2/\mu_0$ (which is position-like).

We then perform a fit as follows. For the FEM calculation, the quantity $E(\omega) = \int d\Omega \frac{1}{2} B_y^2/\mu_0$ is calculated for a number of frequencies $\{\omega_i\}$ which well-represent the observed resonances. For a given parameter set $\mathcal{P}$, we calculate the toy model response $\tilde{E}(\omega;\mathcal{P}) = \langle \frac{1}{2} m_c \Omega_c^2 x_c^2\rangle$ for each frequency ω_i. A cost function C is then chosen to provide a scalar measure of the extent of the difference between the two spectra. Here, we choose a squared-error cost function,

$$C = \sum_i \tfrac{1}{2} \left(\log_{10}(E(\omega_i)) - \log_{10}(\tilde{E}(\omega_i;\mathcal{P})) \right)^2, \tag{5.26}$$

in which differences in the *logarithms* of the response are penalised. This is important: using a cost function with terms $\frac{1}{2}(E - \tilde{E})^2$, the contributions to the cost would be concentrated entirely around the largest peak, but as Fig. 5.7(a) shows, the response varies over multiple orders of magnitude and a good toy model should be able to describe this. Parameters may be fitted by one of many optimisation techniques, such

as gradient descent, conjugate gradient (CG) methods with line search, or advanced optimisation routines such as BFGS [143]. Our model has an extremely small number of parameters, and furthermore we can initialise these with a reasonable physical guess. These properties suggest that the conjugate gradient method will be a good choice. It deals poorly with local minima, although a good initial guess should place the optimiser within the basin of attraction of the sought solution. It also requires the gradients $\partial C/\partial p_i$, for all parameters p_i in the set $\mathcal{P}$. We could use symbolic or automatic differentiation to obtain expressions for these, however in practice it is sufficient to estimate each gradient numerically via[13]

$$\frac{\partial C}{\partial p_i} = \frac{C(\ldots, p_i + \epsilon) - C(\ldots, p_i - \epsilon)}{2\epsilon} + \mathcal{O}(\epsilon^2).$$

The cost of evaluating this grows linearly with N_p, the number of parameters to fit. With so few parameters, this is a more effective approach than producing analytic forms for gradients.

We first apply this method to the spectrum of a microcavity with no cuprate layer. As Fig. 5.8(a) shows, a single oscillator provides an excellent description for the cavity. The fitted parameters imply a resonance with $\Omega_c = 2\pi \times 2.1$ THz and $\gamma_c = 0.47$ THz.

We now turn to the microcavity with embedded superconductor model of Sec. 5.3.1. In Fig. 5.8(b) we reproduce the FEM spectrum of Fig. 5.7(a) and the fitted two-oscillator model. The parameters obtained were $\Omega_c = 2\pi \times 2.1$ THz, $\omega_p = 2\pi \times 2.1$ THz, $\gamma_c = 1.1$ THz, $\gamma_p = 0.2$ THz and $g = 2.6$ THz. In particular, this g is large relative to the frequencies Ω_i, and damping rates γ_i, potentially enabling rapid energy exchange between the Josephson and cavity modes.

5.4 Outlook and further work

In this chapter we have made initial progress into determining how well Josephson modes in cuprates couple to an external cavity mode, specifically considering the geometry of the microcavity array. To begin, we introduced the finite element method in Sec. 5.1, emphasising its application to electromagnetic problems. This led to a solution of the cavity array with the superconductor excluded in Sec. 5.1.2. In Sec. 5.2

[13] It is worth noting that this expression is accurate to order $\mathcal{O}(\epsilon^2)$, unlike the commonly-used finite difference $[C(\ldots, p_i + \epsilon) - C(\ldots, p_i)]/\epsilon$ which is only accurate to order $\mathcal{O}(\epsilon)$.

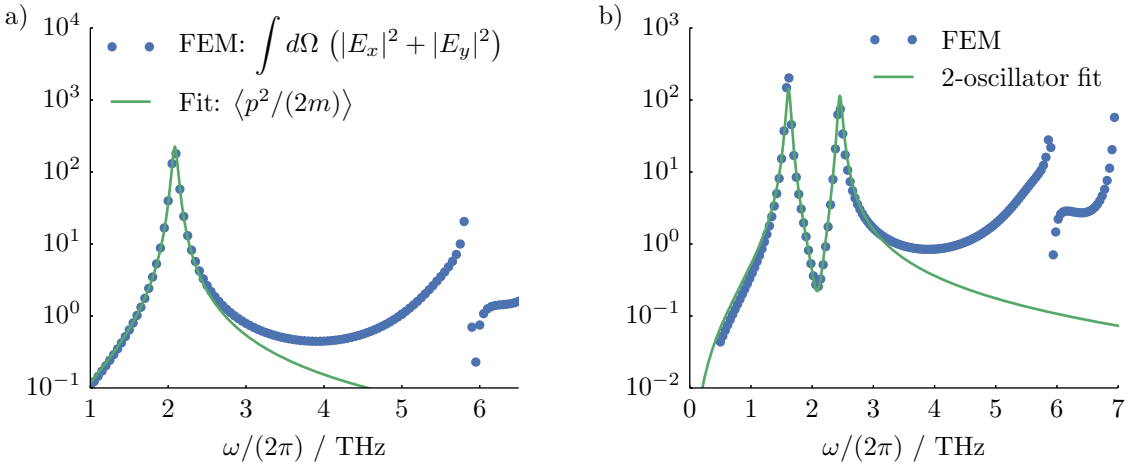

Figure 5.8: (a) Fit of a single-oscillator Hamiltonian $H = p^2/2m + \frac{1}{2}m\Omega^2 x^2$ to finite element calculation of Fig. 5.7(a), "Dielectric (R2)" curve, using conjugate-gradient descent on the cost function Eq. (5.26). The quantity $\langle p^2/(2m)\rangle$ is plotted, to compare with $\int d\Omega \left(|E_x|^2 + |E_y|^2\right)$ from the FEM calculation. Responses in the range 1 THz $\leq \omega/(2\pi) \leq$ 2.5 THz were used in the fit, since the single-oscillator Hamiltonian clearly cannot describe the harmonic at $\sim$ 6 THz. (b) Fit of double-oscillator Hamiltonian Eq. (5.24) to the finite element calculation of Fig. 5.7(a), "Dielectric + cuprate (R2)" curve. Data in the range 1 THz $\leq \omega/(2\pi) \leq$ 3 THz were used in the fit.

we developed a formulation of a single Josephson junction suitable for the use of the finite element method. We then, in Sec. 5.3, considered the effective dielectric model of Laplace et al. [33], expressed in terms of the electric field $\vec{E}$. This produced the spectra of Fig. 5.7(a), in which a significant splitting of $\sim$ 0.9 THz occurs when the superconductor stripe is included. It was possible to describe this well with a pair of coupled oscillators, as in the Hamiltonian of Eq. (5.24).

In addition to the results above, it would be desirable to use a finite element description of a cuprate as a layered Josephson stack, inserted into the microcavity geometry and study the resulting spectra. The parameters in the Hamiltonian of Eq. (5.24) could be fit in exactly the same way, and this would allow for verification of the effective dielectric model used. While initial progress has been made in performing this calculation, the FEM spectra are plagued with unphysical features suggestive of possible numerical instabilities. It is a future goal of this project to overcome these difficul-

ties and compute the spectra with the layered Josephson model. Once this has been accomplished, the development of cooling schemes incorporating external dissipation becomes possible.

6

Conclusions and Outlook

We conclude with a summary of what has been achieved and a view to future directions for this line of research. After introducing the physics of superconductivity, the Josephson effect and high-temperature superconductors in Chapter 2, we discussed the main works in the literature addressing the cavity–junction coupling. Refs. [90–96] study phenomena arising from placing Josephson arrays in resonators and present a promising initial starting point. Crucially, however, their treatment of the system makes assumptions about the geometry which prevents a natural generalisation to our microcavity geometry. The approach of Refs. [36, 97, 98] provides an alternative starting point by working from the Maxwell and Josephson relations directly, building up from a microscopic picture of the electrodynamics. This represents a rigorous foundation, however such a first-principles approach has the issue that the solution for the electrodynamics becomes intractible for anything but the simplest of geometries. This motivates the work of Chapter 5 where we have applied the finite element method to tackle a model similar to that of Ref. [98] but in our geometry of choice.

In Chapter 3, we discussed three cooling schemes of relevance. Through a discussion of sideband cooling in optomechanical systems we introduced the key physics of cooling with light. Moving to superconducting systems, Hammer, Aprili, and Petković [34] present a scheme that has been successfully demonstrated in an artificial Josephson junction, showing enhanced switching currents via a sideband cooling method. Finally we discussed the so-called parametric cooling scheme in which parametric modulation of the strength of a linear coupling induces a cooling process between two oscillators. Our aim in this chapter was twofold: to cover the relevant background of cooling with light, but furthermore to discuss the qualities of these systems that enable cooling

schemes to be a possibility. This is not commonly discussed in the literature. For example, in the optomechanical literature, the Hamiltonian description is essentially fixed owing to the nature of the problem: light exerts a pressure force on the mirror, which gives rise to a $\hbar g_0 \hat{a}^\dagger \hat{a}(\hat{b} + \hat{b}^\dagger)$ coupling term (Eq. (3.3)). In seeking to develop new cooling schemes in new systems, it is crucial to understand the necessary physics that enables such processes.

In Chapter 4, we described a parametric cooling scheme for bilayer cuprates, based on our publication Ref. [35]. Starting from a Josephson stack description of a bilayer cuprate, our scheme upconverts interlayer Josephson plasma fluctuations into higher-frequency intralayer fluctuations. Upconversion is an essential step in any cooling scheme, moving the thermal fluctuations up in frequency to an oscillator which then contains more quanta than the thermal average, and thus will tend to dissipate such fluctuations into any coupled bath. We showed that this upconversion process is plausible in certain bilayer cuprates, and identified YBCO and TBCCO-2201 as materials having the most promising physical parameters for experimental verification.

In Chapter 5, we extended the calculations of Ref. [98] to enable the more complex geometry of the microcavity array to be addressed. By exploiting the flexibility of the finite element method we were able to find good FEM descriptions of the single Josephson junction and subsequently the junction stack embedded in the microcavity array. In this work we restricted our attention to a two-dimensional approximation of the microcavity array on the basis that the physics is expected to be unchanged. Working with the effective dielectric model suggested in Ref. [33], our calculations suggest that strong coupling with $g/\omega_p \sim 0.2$ can be achieved using this geometry. In the future, we would like to reproduce this result using the microscopic model for the Josephson electrodynamics, however issues of numerical stability must first be resolved.

In addition to the further work outlined above, the subsequent goal of this research project should be to combine the upconversion process outlined (or similar) with the cavity coupling in order to produce a cooling scheme in which energy is dissipated externally. This would pave the way towards continuously-operable schemes with reduced danger of unintentionally heating the superconductor. Looking further, there is potential to examine the in-plane fluctuations and the physics as the temperature approaches the transition at T_c. Finally, the question of inducing an out-of-equilibrium superconducting state above T_c remains.

A

Numerical methods

In this appendix we introduce the numerical methods for stochastic integration as used in this thesis. Such integration schemes are used heavily in reaching the results of Chapter 4.

A.1 Langevin dynamics

In this thesis, laser cooling schemes are explored predominantly by numerical means. In order to model classical, thermal systems, we adopt the classical Langevin framework [144, 145]. We consider a system of particles indexed by i and described by the dynamical equations

$$\begin{aligned} \dot{x}_i &= \frac{p_i}{m_i}, \\ \dot{p}_i &= F_i(\{x_j\}) - \gamma_i p_i + \xi_i(t). \end{aligned} \tag{A.1}$$

A particle with index i, position x_i, momentum p_i and mass m_i moves in one dimension (for simplicity) under a force F_i. The Langevin framework incorporates a damping force $-\gamma_i p_i$ and a stochastic force $\xi_i(t)$ intended to model the effect of being coupled to a thermal bath. In molecular dynamics, this framework is used to account for other particles and degrees of freedom not explicitly modelled, Brownian motion being a common example of this. Typical assumptions are that the noise term $\xi_i(t)$ is Gaussian, white and uncorrelated between different particles. Denoting its strength as Γ_i, it thus

satisfies

$$\langle \xi_i(t) \rangle = 0,$$
$$\langle \xi_i(t)\xi_j(t') \rangle = \Gamma_i \delta_{ij} \delta(t - t').$$

In simple situations it is possible to solve these equations analytically. For example, consider a single particle in a harmonic potential in the overdamped regime $\gamma > 2\Omega_m$, for which Eq. (A.1) simplifies to[1]

$$m\gamma\dot{x} + m\Omega_m^2 x = \xi(t).$$

This has the formal solution

$$x(t) = x(0) \exp\left(\frac{-\Omega_m^2 t}{\gamma}\right) + \frac{1}{m\gamma} \int_0^t dt' \; \xi(t') \exp\left(-\frac{\Omega_m^2}{\gamma}(t - t')\right). \tag{A.3}$$

A timescale γ/Ω_m^2 appears as the time over which correlations in the particle's motion vanish due to the thermal bath. Furthermore, we can relate the damping and forcing to the bath temperature. By equipartition the average potential energy $\langle \frac{1}{2} m\Omega_m^2 x^2(t) \rangle = \frac{1}{2} k_B T$, leading to the relation

$$\Gamma = 2\gamma m k_B T, \tag{A.4}$$

which is a statement of the fluctuation-dissipation theorem. Working in reverse, for a fixed γ, we can use a measurement of the fluctuations to infer Γ and thus measure the temperature when out-of-equilibrium.

A.1.1 Numerical integrators

Analytic approaches are, while useful, rarely possible for sufficiently complex systems. This necessitates the numerical integration of Langevin equations. One simple approach is the Euler scheme, discussed by Gardiner [146] and Van Kampen [147], however this is a relatively low-accuracy method. Instead we make use of the velocity Verlet

[1] This is an approximation for the low-frequency response only, specifically we can rewrite Eq. (A.1) in the Fourier domain, where we define $\tilde{x}[\omega] = \frac{1}{2\pi} \int dt \; x(t) \exp(i\omega t)$ as the Fourier transform of the variable $x(t)$. This gives

$$\left[-\frac{\omega^2}{\gamma\Omega_m} - \frac{i\omega}{\Omega_m} + \frac{\Omega_m}{\gamma}\right] \tilde{x}[\omega] = \frac{\tilde{\xi}[\omega]}{m\gamma\Omega_m}, \tag{A.2}$$

and provided we are in the regime $\Omega_m < \gamma$, $\omega \ll \gamma$, the leftmost term $(-\omega^2/\gamma\Omega_m)\tilde{x}[\omega]$ becomes negligible with respect to the term $-i\omega/\Omega_m$, allowing the second time-derivative in Eq. (A.1) to be dropped under these conditions.

algorithm [126]. This is a quasi-symplectic propagator which has the advantage of being relatively simple to express (unlike e.g. fourth-order schemes [146]), and exploits the symplectic structure of the phase space flows of the underlying Hamiltonian. The key advantage is superior accuracy over long integration times in comparison to standard methods[2] [148]. For the dynamics described by Eq. (A.1), the update equations for a single time step read as [126]

$$p^\star = e^{-\gamma dt/2} p_0 + \frac{1 - e^{-\gamma dt/2}}{\gamma} F(x_0) + \mathcal{N}^{(0)}\left\{ m k_B T \left(1 - e^{-\gamma dt}\right)\right\}, \tag{A.5a}$$

$$x_{dt} = x_0 + \frac{dt}{m} p^\star, \tag{A.5b}$$

$$p_{dt} = e^{-\gamma dt/2} p^\star + \frac{1 - e^{-\gamma dt/2}}{\gamma} F(x_{dt}) + \mathcal{N}^{(1)}\left\{ m k_B T \left(1 - e^{-\gamma dt}\right)\right\}, \tag{A.5c}$$

where x_0 and p_0 are the values of the position and momentum at the start of the time step. The time step length is dt. The two instances of $\mathcal{N}^{(m)}\{\sigma^2\}$ denote two independent samples from a Gaussian distribution with zero mean and variance σ^2. The various exponentials and prefactors should be cached to avoid redundant recomputation. Additionally, it is often the evaluation of $F(x)$ which dominates the computation of Eq. (A.5), and so it is important to note that the force evaluation $F(x_{dt})$ is identical to the evaluation $F(x_0)$ at the start of the next time step. Thus only one force call per time step is required.

A.1.2 Fokker-Planck formulation

The Langevin approach above describes the trajectory of a single instance through its phase space, under the influence of both deterministic and stochastic forces. By comparison, in the Fokker-Planck approach the probability density $P(\vec{z}, t) = P(x_1, x_2, \ldots, p_1, p_2, \ldots, t)$ is the central object and its evolution in time is described by a Fokker-Planck equation. Consider a system of variables $\vec{z}$ obeying the Langevin equations

$$\frac{d\vec{z}}{dt} = \vec{A}(\vec{z}, t) + \vec{\xi}(t), \tag{A.6}$$

where $\vec{A}$ gives the deterministic dynamics and $\vec{\xi}(t)$ is the stochastic force satisfying

$$\langle \xi_i(t) \xi_j(t') \rangle = B_{ij} \delta(t - t'). \tag{A.7}$$

[2]For comparison, the Euler scheme is strongly convergent with order $\frac{1}{2}$, and weakly convergent with order 1. The velocity Verlet algorithm shown is weakly convergent with order 2 [126], the weak order of convergence being more relevant for distributional quantities. By contrast, the strong order of convergence is more important for applications requiring the study of individual trajectories.

The matrix elements B_{ij} give the strength and correlations of the stochastic forces[3]. The probability density $P(\vec{z},t)$ obeys the general Fokker-Planck equation [147, 149]

$$\frac{\partial}{\partial t}P(\vec{z},t) = -\sum_i \frac{\partial}{\partial z_i}A_i(\vec{z},t)P(\vec{z},t) + \frac{1}{2}\sum_{i,j}\frac{\partial^2}{\partial z_i \partial z_j}B_{ij}(\vec{z},t)P(\vec{z},t). \tag{A.8}$$

The first term on the RHS is the 'drift term' arising from the deterministic dynamics. The second term is referred to as the 'diffusion term' and describes the spreading-out of the probability distribution due to the noise $\vec{\xi}(t)$. As a concrete example, for a single Josephson junction we can write [149]

$$\frac{\partial}{\partial t}P(\phi,\dot{\phi},t) = -\frac{\partial(\dot{\phi}P)}{\partial\phi} + \frac{\partial}{\partial\dot{\phi}}\left[(\omega_p^2\sin\phi + \gamma\dot{\phi})P\right] + \frac{2e}{\hbar I_c}\gamma\omega_p^2 k_B T\,\frac{\partial^2 P}{\partial\dot{\phi}^2} \tag{A.9}$$

for the dynamics of the Josephson phase, where the noise term has arisen as the ratio of the thermal energy k_BT to the Josephson energy $E_J = \hbar I_c/2e$. The symbol $\dot{\phi} := \partial\phi/\partial t$ is the time-derivative of the Josephson phase ϕ, and is treated as an independent variable. Eq. (A.9) is the Kramers' equation for a single particle in a $(1-\cos\phi)$ potential.

In the case that the Fokker-Planck equation is linear, there is a direct solution in terms of its second moments. For the general linear Fokker-Planck equation

$$\frac{\partial P(z,t)}{\partial t} = -\sum_{ij} A_{ij}\frac{\partial}{\partial z_i}z_j P + \frac{1}{2}\sum_{ij}B_{ij}\frac{\partial^2 P}{\partial z_i\partial z_j}, \tag{A.10}$$

the first- and second-order moments evolve according to [147]

$$\frac{\partial}{\partial t}\langle z_i\rangle = \sum_j A_{ij}(t)\langle z_j\rangle, \tag{A.11a}$$

$$\frac{\partial}{\partial t}\langle z_i z_j\rangle = \sum_k A_{ik}(t)\langle z_k z_j\rangle + \sum_k A_{jk}(t)\langle z_i z_k\rangle + B_{ij}. \tag{A.11b}$$

Defining $\Xi_{ij} := \langle z_i z_j\rangle - \langle z_i\rangle\langle z_j\rangle$, the full solution is a multivariate Gaussian, namely

$$P(\vec{z},t) = (2\pi)^{-\frac{1}{2}N}(\det\Xi)^{-1/2}\exp\left[-\frac{1}{2}(\vec{z}-\langle\vec{z}\rangle)^T\Xi^{-1}(\vec{z}-\langle\vec{z}\rangle)\right], \tag{A.12}$$

[3]Note that it will commonly be the case that B_{ij} is diagonal, corresponding to independent noise acting on the variables $\{z_i\}$. Additionally, in Newton-like differential equations the noise terms are only finite for the momentum variables, being zero for position variables. However, the possibility of off-diagonal elements allows for correlations between the noise terms, which may be useful in some applications.

in which N is the dimension of the phase space.

By numerically integrating the closed first-order system of Eq. (A.11), we may directly solve the Fokker-Planck equation. This is equivalent to sampling across many Langevin trajectories, however there is the advantage that only a single numerical integration is required. Thus the approach of integrating Eq. (A.11) can be more efficient for systems with a modest number of degrees of freedom. For example, this Fokker-Planck approach is ideal for simulating the systems of Chapter 4 in the case of a small stack (up to ten junctions), providing the linearised equations of motion are being used and only the fluctuations are of interest.

For high-dimensional problems, Langevin trajectories are preferred since this Fokker-Planck approach will keep track of all pairs of covariances, hence for the 100-junction stack calculations of Chapter 4 Langevin trajectories are used exclusively. In high dimension, most pairs will be physically separated and thus only weakly correlated. There is the approach of Ammar et al. [150, 151] which exploits this redundancy and can tackle the high-dimensional Fokker-Planck equation directly. So-called tensor train methods may also be of use in addressing the high-dimensional Fokker Planck equation efficiently [152], by compressed representations of the vector space.

Bibliography

[1] H. K. Onnes. "The resistance of pure mercury at helium temperatures". *Commun. Phys. Lab. Univ. Leiden* **12**, 120, 1911.

[2] H. K. Onnes. "Further experiments with liquid helium. H. On the electrical resistance etc. (continued). VIII. The sudden disappearance of the ordinary resistance of tin, and the superconductive state of lead". *Commun. Phys. Lab. Univ. Leiden*, 133d, 1913.

[3] G. Aschermann, E. Friedrich, E. Justi, and J. Kramer. "Supraleitfähige Verbindungen mit extrem hohen Sprungtemperaturen (NbH und NbN)". *Phys. Zeir.* **42**, 349, 1941.

[4] G. F. Hardy and J. K. Hulm. "Superconducting Silicides and Germanides". *Physical Review* **89**, 884, 1953.

[5] J. Bardeen, L. N. Cooper, and J. R. Schrieffer. "Theory of Superconductivity". *Physical Review* **108**, 1175, 1957.

[6] J. G. Bednorz and K. A. Müller. "Possible high T_c superconductivity in the Ba-La-Cu-O system". *Zeitschrift für Physik B Condensed Matter* **64**, 189, 1986.

[7] M. K. Wu, J. R. Ashburn, C. J. Torng, P. H. Hor, R. L. Meng, L. Gao, Z. J. Huang, Y. Q. Wang, and C. W. Chu. "Superconductivity at 93 K in a new mixed-phase Y-Ba-Cu-O compound system at ambient pressure". *Physical Review Letters* **58**, 908, 1987.

[8] P. Dai, B. Chakoumakos, G. Sun, K. Wong, Y. Xin, and D. Lu. "Synthesis and neutron powder diffraction study of the superconductor $HgBa_2Ca_2Cu_3O_{8+\delta}$ by Tl substitution". *Physica C: Superconductivity* **243**, 201, 1995.

[9] P. W. Anderson. "The Resonating Valence Bond State in La_2CuO_4 and Superconductivity." *Science (New York, N.Y.)* **235**, 1196, 1987.

[10] P. Monthoux, A. Balatsky, and D. Pines. "Weak-coupling theory of high-temperature superconductivity in the antiferromagnetically correlated copper oxides". *Physical Review B* **46**, 14803, 1992.

[11] V. J. Emery and S. A. Kivelson. "Importance of phase fluctuations in superconductors with small superfluid density". *Nature* **374**, 434, 1995.

[12] J. Wheatley, T. Hsu, and P. Anderson. "Interlayer pair hopping: Superconductivity from the resonating-valence-bond state". *Physical Review B* **37**, 5897, 1988.

[13] S. Chakravarty, A. Sudbø, P. W. Anderson, and S. Strong. "Interlayer tunneling and gap anisotropy in high-temperature superconductors." *Science (New York, N.Y.)* **261**, 337, 1993.

[14] D. Wineland and W. Itano. "Laser cooling of atoms". *Physical Review A* **20**, 1521, 1979.

[15] B. Abbott et al. "Detector description and performance for the first coincidence observations between LIGO and GEO". *Nuclear Instruments and Methods in Physics Research Section A: Accelerators, Spectrometers, Detectors and Associated Equipment* **517**, 154, 2004.

[16] B. Abbott et al. "Observation of a kilogram-scale oscillator near its quantum ground state". *New Journal of Physics* **11**, 073032, 2009.

[17] M. Aspelmeyer, T. J. Kippenberg, and F. Marquardt. "Cavity optomechanics". *Reviews of Modern Physics* **86**, 1391, 2014.

[18] P. Pringsheim. "Zwei Bemerkungen über den Unterschied von Lumineszenz- und Temperaturstrahlung". *Zeitschrift für Physik* **57**, 739, 1929.

[19] R. I. Epstein, M. I. Buchwald, B. C. Edwards, T. R. Gosnell, and C. E. Mungan. "Observation of laser-induced fluorescent cooling of a solid". *Nature* **377**, 500, 1995.

[20] G. Nemova and R. Kashyap. "Laser cooling of solids". *Reports on Progress in Physics* **73**, 086501, 2010.

[21] A. Subedi, A. Cavalleri, and A. Georges. "Theory of nonlinear phononics for coherent light control of solids". *Physical Review B* **89**, 220301, 2014.

[22] M. Rini, R. Tobey, N. Dean, J. Itatani, Y. Tomioka, Y. Tokura, R. W. Schoenlein, and A. Cavalleri. "Control of the electronic phase of a manganite by mode-selective vibrational excitation." *Nature* **449**, 72, 2007.

[23] M. Först, R. I. Tobey, S. Wall, H. Bromberger, V. Khanna, A. L. Cavalieri, Y.-D. Chuang, W. S. Lee, R. Moore, W. F. Schlotter, J. J. Turner, O. Krupin, M. Trigo, H. Zheng, J. F. Mitchell, S. S. Dhesi, J. P. Hill, and A. Cavalleri. "Driving magnetic order in a manganite by ultrafast lattice excitation". *Physical Review B* **84**, 241104, 2011.

[24] A. D. Caviglia, R. Scherwitzl, P. Popovich, W. Hu, H. Bromberger, R. Singla, M. Mitrano, M. C. Hoffmann, S. Kaiser, P. Zubko, S. Gariglio, J.-M. Triscone, M. Först, and A. Cavalleri. "Ultrafast Strain Engineering in Complex Oxide Heterostructures". *Physical Review Letters* **108**, 136801, 2012.

[25] D. Fausti, R. I. Tobey, N. Dean, S. Kaiser, A. Dienst, M. C. Hoffmann, S. Pyon, T. Takayama, H. Takagi, and A. Cavalleri. "Light-induced superconductivity in a stripe-ordered cuprate." *Science (New York, N.Y.)* **331**, 189, 2011.

[26] S. Kaiser, C. R. Hunt, D. Nicoletti, W. Hu, I. Gierz, H. Y. Liu, M. L. Tacon, T. Loew, D. Haug, B. Keimer, and A. Cavalleri. "Optically induced coherent transport far above T_c in underdoped $YBa_2Cu_3O_{6+\delta}$". *Physical Review B* **89**, 184516, 2014.

[27] W. Hu, S. Kaiser, D. Nicoletti, C. R. Hunt, I. Gierz, M. C. Hoffmann, M. Le Tacon, T. Loew, B. Keimer, and A. Cavalleri. "Optically enhanced coherent transport in $YBa_2Cu_3O_{6.5}$ by ultrafast redistribution of interlayer coupling." *Nature Materials* **13**, 705, 2014.

[28] K. Miyano, T. Tanaka, Y. Tomioka, and Y. Tokura. "Photoinduced Insulator-to-Metal Transition in a Perovskite Manganite". *Physical Review Letters* **78**, 4257, 1997.

[29] A. Cavalleri, C. Tóth, C. Siders, J. Squier, F. Ráksi, P. Forget, and J. Kieffer. "Femtosecond Structural Dynamics in VO_2 during an Ultrafast Solid-Solid Phase Transition". *Physical Review Letters* **87**, 237401, 2001.

[30] S. Iwai, S. Tanaka, K. Fujinuma, H. Kishida, H. Okamoto, and Y. Tokura. "Ultrafast Optical Switching from an Ionic to a Neutral State in Tetrathiafulvalene-p-Chloranil (TTF-CA) Observed in Femtosecond Reflection Spectroscopy". *Physical Review Letters* **88**, 057402, 2002.

[31] M. Chollet, L. Guerin, N. Uchida, S. Fukaya, H. Shimoda, T. Ishikawa, K. Matsuda, T. Hasegawa, A. Ota, H. Yamochi, G. Saito, R. Tazaki, S.-I. Adachi, and S.-Y. Koshihara. "Gigantic photoresponse in 1/4-filled-band organic salt $(EDO\text{-}TTF)_2PF_6$." *Science (New York, N.Y.)* **307**, 86, 2005.

[32] L. Perfetti, P. Loukakos, M. Lisowski, U. Bovensiepen, H. Berger, S. Biermann, P. Cornaglia, A. Georges, and M. Wolf. "Time Evolution of the Electronic Structure of 1T-TaS_2 through the Insulator-Metal Transition". *Physical Review Letters* **97**, 067402, 2006.

[33] Y. Laplace, S. Fernandez-Pena, S. Gariglio, J.-M. Triscone, and A. Cavalleri. "Proposed cavity Josephson plasmonics with complex-oxide heterostructures". *arXiv preprint*, 1503.06117, 2015.

[34] J. Hammer, M. Aprili, and I. Petković. "Microwave Cooling of Josephson Plasma Oscillations". *Physical Review Letters* **107**, 017001, 2011.

[35] S. J. Denny, S. R. Clark, Y. Laplace, A. Cavalleri, and D. Jaksch. "Proposed Parametric Cooling of Bilayer Cuprate Superconductors by Terahertz Excitation". *Physical Review Letters* **114**, 137001, 2015.

[36] L. Bulaevskii and A. Koshelev. "Radiation from a Single Josephson Junction into Free Space due to Josephson Oscillations". *Physical Review Letters* **97**, 267001, 2006.

[37] H. K. Onnes. *Through Measurement to Knowledge: The Selected Papers of Heike Kamerlingh Onnes 1853-1926*. Springer, 1991.

[38] W. Meissner and R. Ochsenfeld. "Ein neuer Effekt bei Eintritt der Supraleitfähigkeit". *Die Naturwissenschaften* **21**, 787, 1933.

[39] L. Landau. "On the Theory of Phase Transitions". *Zh. Eksp. Teor. Fiz.* **7**, 19, 1937.

[40] L. D. Landau. *Collected Papers*. Pergamon Press, 1965.

[41] M. Tinkham. *Introduction to Superconductivity*. 2nd ed. Dover Publications, 1996.

[42] J. F. Annett. *Superconductivity, superfluids and condensates*. Oxford University Press, 2004.

[43] A. Altland and B. Simons. *Condensed Matter Field Theory*. Cambridge University Press, 2006.

[44] L. Cooper. "Bound Electron Pairs in a Degenerate Fermi Gas". *Physical Review* **104**, 1189, 1956.

[45] V. Ginzburg and D. Kirzhnits. *High-temperature superconductivity*. Consultants Bureau, 1982.

[46] J. Nagamatsu, N. Nakagawa, T. Muranaka, Y. Zenitani, and J. Akimitsu. "Superconductivity at 39 K in magnesium diboride." *Nature* **410**, 63, 2001.

[47] N. Tsuda. *Electronic Conduction in Oxides*. Springer Science & Business Media, 2000.

[48] A. P. Drozdov, M. I. Eremets, I. A. Troyan, V. Ksenofontov, and S. I. Shylin. "Conventional superconductivity at 203 K at high pressures in the sulfur hydride system". *Nature* **525**, 73, 2015.

[49] B. Josephson. "Possible new effects in superconductive tunnelling". *Physics Letters* **1**, 251, 1962.

[50] R. P. Feynman, R. B. Leighton, and M. Sands. *The Feynman Lectures on Physics, Volume III*. Addison-Wesley, 1965.

[51] D. E. McCumber. "Effect of ac Impedance on dc Voltage-Current Characteristics of Superconductor Weak-Link Junctions". *Journal of Applied Physics* **39**, 3113, 1968.

[52] D. Larbalestier, A. Gurevich, D. M. Feldmann, and A. Polyanskii. "High-Tc superconducting materials for electric power applications." *Nature* **414**, 368, 2001.

[53] A. Gurevich. "To use or not to use cool superconductors?" *Nature materials* **10**, 255, 2011.

[54] R. M. Nault. *Report of the Basic Energy Sciences Workshop on Superconductivity*. Tech. rep. Argonne National Laboratory, 2006.

[55] C. E. Gough, M. S. Colclough, E. M. Forgan, R. G. Jordan, M. Keene, C. M. Muirhead, A. I. M. Rae, N. Thomas, J. S. Abell, and S. Sutton. "Flux Quantization in a high-T_c superconductor". *Nature* **326**, 855, 1987.

[56] P. A. Lee, N. Nagaosa, and X.-G. Wen. "Doping a Mott insulator: Physics of high-temperature superconductivity". *Reviews of Modern Physics* **78**, 17, 2006.

[57] R. Kleiner and P. Müller. "Intrinsic Josephson effects in high-Tc superconductors". *Physical Review B* **49**, 1327, 1994.

[58] A. G. Loeser, Z.-X. Shen, D. S. Dessau, D. S. Marshall, C. H. Park, P. Fournier, and A. Kapitulnik. "Excitation Gap in the Normal State of Underdoped $Bi_2Sr_2CaCu_2O_{8+\delta}$". *Science* **273**, 325, 1996.

[59] H. Ding, T. Yokoya, J. C. Campuzano, T. Takahashi, M. Randeria, M. R. Norman, T. Mochiku, K. Kadowaki, and J. Giapintzakis. "Spectroscopic evidence for a pseudogap in the normal state of underdoped high-Tc superconductors". *Nature* **382**, 51, 1996.

[60] C. Renner, B. Revaz, J.-Y. Genoud, K. Kadowaki, and Ø. Fischer. "Pseudogap Precursor of the Superconducting Gap in Under- and Overdoped $Bi_2Sr_2CaCu_2O_{8+\delta}$". *Physical Review Letters* **80**, 149, 1998.

[61] V. Emery and S. Kivelson. "Superconductivity in Bad Metals". *Physical Review Letters* **74**, 3253, 1995.

[62] J. M. Wheatley, T. C. Hsu, and P. W. Anderson. "Interlayer effects in high-Tc superconductors". *Nature* **333**, 121, 1988.

[63] P. W. Anderson. "Interlayer tunneling mechanism for high-tc superconductivity: comparison with C axis infrared experiments." *Science (New York, N.Y.)* **268**, 1154, 1995.

[64] P. W. Anderson. "c-Axis Electrodynamics as Evidence for the Interlayer Theory of High-Temperature Superconductivity". *Science* **279**, 1196, 1998.

[65] R. Kleiner, F. Steinmeyer, G. Kunkel, and P. Müller. "Intrinsic Josephson effects in $Bi_2Sr_2CaCu_2O_8$ single crystals". *Physical Review Letters* **68**, 2394, 1992.

[66] A. Irie, Y. Hirai, and G. Oya. "Fiske and flux-flow modes of the intrinsic Josephson junctions in $Bi_2Sr_2CaCu_2O_y$ mesas". *Applied Physics Letters* **72**, 2159, 1998.

[67] V. M. Krasnov, A. Yurgens, and D. Winkler. "Fiske steps in intrinsic $Bi_2Sr_2CaCu_2O_{8+x}$ stacked Josephson junctions". *Physical Review B* **59**, 8463, 1999.

[68] S. Kim, H. Wang, T. Hatano, S. Urayama, S. Kawakami, M. Nagao, Y. Takano, T. Yamashita, and K. Lee. "Fiske steps studied by flux-flow resistance oscillation in a narrow stack of $Bi_2Sr_2CaCu_2O_{8+\delta}$ junctions". *Physical Review B* **72**, 140504, 2005.

[69] Y.-J. Doh, J. Kim, K.-T. Kim, and H.-J. Lee. "Microwave-induced constant voltage steps in surface junctions of $Bi_2Sr_2CaCu_2O_{8+\delta}$ single crystals". *Physical Review B* **61**, R3834, 2000.

[70] H. Wang, P. Wu, and T. Yamashita. "Terahertz Responses of Intrinsic Josephson Junctions in High TC Superconductors". *Physical Review Letters* **87**, 107002, 2001.

[71] Y. Latyshev, M. Gaifullin, T. Yamashita, M. Machida, and Y. Matsuda. "Shapiro Step Response in the Coherent Josephson Flux Flow State of $Bi_2Sr_2CaCu_2O_{8+\delta}$". *Physical Review Letters* **87**, 247007, 2001.

[72] W. Lawrence and S. Doniach. "Theory of Layer-Structure Superconductors". In: *Proceeding of the Twelth International Conference on Low Temperature Physics*. Ed. by E. Kanda. Tokyo: Keigaku, 1970.

[73] L. Bulaevskii, M. Zamora, D. Baeriswyl, H. Beck, and J. Clem. "Time-dependent equations for phase differences and a collective mode in Josephson-coupled layered superconductors". *Physical Review B* **50**, 12831, 1994.

[74] X. Hu and S.-Z. Lin. "Phase dynamics in a stack of inductively coupled intrinsic Josephson junctions and terahertz electromagnetic radiation". *Superconductor Science and Technology* **23**, 053001, 2010.

[75] E. Roddick and D. Stroud. "Effect of Phase Fluctuations on the Low-Temperature Penetration Depth of High- Tc Superconductors". *Physical Review Letters* **74**, 1430, 1995.

[76] E. Carlson, S. Kivelson, V. Emery, and E. Manousakis. "Classical Phase Fluctuations in High Temperature Superconductors". *Physical Review Letters* **83**, 612, 1999.

[77] S. Vadlamannati, Q. Li, T. Venkatesan, W. McLean, and P. Lindenfeld. "Enhanced Kosterlitz-Thouless transition in $YBa_2Cu_3O_{7-x}/PrBa_2Cu_3O_{7-x}$ multilayers as a measure of two-dimensionality". *Physical Review B* **44**, 7094, 1991.

[78] J. Corson, R. Mallozzi, J. Orenstein, J. N. Eckstein, and I. Bozovic. "Vanishing of phase coherence in underdoped $Bi_2Sr_2CaCu_2O_{8+\delta}$". *Nature* **398**, 221, 1999.

[79] Y. Wang, Z. Xu, T. Kakeshita, S. Uchida, S. Ono, Y. Ando, and N. Ong. "Onset of the vortexlike Nernst signal above Tc in $La_{2-x}Sr_xCuO_4$ and $Bi_2Sr_{2-y}La_yCuO_6$". *Physical Review B* **64**, 224519, 2001.

[80] L. Li, Y. Wang, M. J. Naughton, S. Ono, Y. Ando, and N. P. Ong. "Strongly nonlinear magnetization above Tc in $Bi_2Sr_2CaCu_2O_{8+\delta}$". *Europhysics Letters (EPL)* **72**, 451, 2005.

[81] D. Matthey, N. Reyren, J.-M. Triscone, and T. Schneider. "Electric-Field-Effect Modulation of the Transition Temperature, Mobile Carrier Density, and In-Plane Penetration Depth of $NdBa_2Cu_3O_{7-\delta}$ Thin Films". *Physical Review Letters* **98**, 057002, 2007.

[82] A. Hosseini, D. Broun, D. Sheehy, T. Davis, M. Franz, W. Hardy, R. Liang, and D. Bonn. "Survival of the d-Wave Superconducting State near the Edge of Antiferromagnetism in the Cuprate Phase Diagram". *Physical Review Letters* **93**, 107003, 2004.

[83] Y. Zuev, M. Seog Kim, and T. Lemberger. "Correlation between Superfluid Density and TC of Underdoped $YBa_2Cu_3O_{6+x}$ Near the Superconductor-Insulator Transition". *Physical Review Letters* **95**, 137002, 2005.

[84] R. Liang, D. A. Bonn, W. N. Hardy, and D. Broun. "Lower Critical Field and Superfluid Density of Highly Underdoped $YBa_2Cu_3O_{6+x}$ Single Crystals". *Physical Review Letters* **94**, 117001, 2005.

[85] A. Rüfenacht, J.-P. Locquet, J. Fompeyrine, D. Caimi, and P. Martinoli. "Electrostatic Modulation of the Superfluid Density in an Ultrathin $La_{2-x}Sr_xCuO_4$ Film". *Physical Review Letters* **96**, 227002, 2006.

[86] D. Broun, W. Huttema, P. Turner, S. Özcan, B. Morgan, R. Liang, W. Hardy, and D. Bonn. "Superfluid Density in a Highly Underdoped $YBa_2Cu_3O_{6+y}$ Superconductor". *Physical Review Letters* **99**, 237003, 2007.

[87] A. Mihlin and A. Auerbach. "Temperature dependence of the order parameter of cuprate superconductors". *Physical Review B* **80**, 134521, 2009.

[88] L. Benfatto, C. Castellani, and T. Giamarchi. "Kosterlitz-Thouless Behavior in Layered Superconductors: The Role of the Vortex Core Energy". *Physical Review Letters* **98**, 117008, 2007.

[89] M. L. Bellac, F. Mortessagne, and G. G. Batrouni. *Equilibrium and Non-Equilibrium Statistical Thermodynamics*. Cambridge University Press, 2004.

[90] J. Harbaugh and D. Stroud. "Model for a Josephson junction array coupled to a resonant cavity". *Physical Review B* **61**, 14765, 2000.

[91] E. Almaas and D. Stroud. "Dynamics of a Josephson array in a resonant cavity". *Physical Review B* **65**, 134502, 2002.

[92] E. Almaas and D. Stroud. "Resonant-cavity-induced phase locking and voltage steps in a Josephson array". *Physical Review B* **63**, 144522, 2001.

[93] W. Al-Saidi and D. Stroud. "Eigenstates of a small Josephson junction coupled to a resonant cavity". *Physical Review B* **65**, 014512, 2001.

[94] W. A. Al-Saidi. "Topics in the Theory of Small Josephson Junctions and Layered Superconductors". PhD thesis. Ohio State University, 2003.

[95] I. Tornes and D. Stroud. "Possibility of c-axis voltage steps for a cuprate superconductor in a resonant cavity". *Physical Review B* **68**, 052512, 2003.

[96] I. Tornes and D. Stroud. "Long Josephson junction in a resonant cavity". *Physical Review B* **71**, 144503, 2005.

[97] L. Bulaevskii and A. Koshelev. "Radiation due to Josephson Oscillations in Layered Superconductors". *Physical Review Letters* **99**, 057002, 2007.

[98] L. N. Bulaevskii and A. E. Koshelev. "Radiation from Flux Flow in Josephson Junction Structures". *Journal of Superconductivity and Novel Magnetism* **19**, 349, 2006.

[99] D. Wineland, R. Drullinger, and F. Walls. "Radiation-Pressure Cooling of Bound Resonant Absorbers". *Physical Review Letters* **40**, 1639, 1978.

[100] S. Andreev, V. Balykin, V. Letokhov, and V. Minogin. "Radiative slowing and reduction of the energy spread of a beam of sodium atoms to 1.5 K in an oppositely directed laser beam". *JETP Lett* **34**, 442, 1981.

[101] S. Chu. "Laser manipulation of atoms and particles." *Science (New York, N.Y.)* **253**, 861, 1991.

[102] V. B. Braginsky, Y. I. Vorontsov, and K. S. Thorne. "Quantum nondemolition measurements." *Science (New York, N.Y.)* **209**, 547, 1980.

[103] C. M. Caves, K. S. Thorne, R. W. P. Drever, V. D. Sandberg, and M. Zimmermann. "On the measurement of a weak classical force coupled to a quantum-mechanical oscillator. I. Issues of principle". *Reviews of Modern Physics* **52**, 341, 1980.

[104] J. Zhang, D. Li, R. Chen, and Q. Xiong. "Laser cooling of a semiconductor by 40 Kelvin." *Nature* **493**, 504, 2013.

[105] P. Domokos and H. Ritsch. "Mechanical effects of light in optical resonators". *Journal of the Optical Society of America B* **20**, 1098, 2003.

[106] F. Marquardt, A. Clerk, and S. Girvin. "Quantum theory of optomechanical cooling". *Journal of Modern Optics* **55**, 3329, 2008.

[107] M. Aspelmeyer, S. Gröblacher, K. Hammerer, and N. Kiesel. "Quantum optomechanics – throwing a glance". *Journal of the Optical Society of America B* **27**, A189, 2010.

[108] M. Aspelmeyer, P. Meystre, and K. Schwab. "Quantum optomechanics". *Physics Today* **65**, 29, 2012.

[109] P. Meystre. "A short walk through quantum optomechanics". *Annalen der Physik* **525**, 215, 2013.

[110] D. Blair, E. Ivanov, M. Tobar, P. Turner, F. van Kann, and I. Heng. "High Sensitivity Gravitational Wave Antenna with Parametric Transducer Readout". *Physical Review Letters* **74**, 1908, 1995.

[111] P. Cohadon, A. Heidmann, and M. Pinard. "Cooling of a Mirror by Radiation Pressure". *Physical Review Letters* **83**, 3174, 1999.

[112] I. Wilson-Rae, P. Zoller, and A. Imamoğlu. "Laser Cooling of a Nanomechanical Resonator Mode to its Quantum Ground State". *Physical Review Letters* **92**, 075507, 2004.

[113] I. Martin, A. Shnirman, L. Tian, and P. Zoller. "Ground-state cooling of mechanical resonators". *Physical Review B* **69**, 125339, 2004.

[114] A. Schliesser, R. Rivière, G. Anetsberger, O. Arcizet, and T. J. Kippenberg. "Resolved-sideband cooling of a micromechanical oscillator". *Nature Physics* **4**, 415, 2008.

[115] C. Law. "Interaction between a moving mirror and radiation pressure: A Hamiltonian formulation". *Physical Review A* **51**, 2537, 1995.

[116] A. Xuereb. "Optical Cooling Using the Dipole Force". PhD thesis. University of Southampton, 2011.

[117] M. Fistul and A. Ustinov. "Quantum cavity modes in spatially extended Josephson systems". *Physical Review B* **75**, 214506, 2007.

[118] L. Brown and G. Gabrielse. "Geonium theory: Physics of a single electron or ion in a Penning trap". *Reviews of Modern Physics* **58**, 233, 1986.

[119] H.-P. Breuer and F. Petruccione. *The Theory of Open Quantum Systems*. Oxford University Press, 2007.

[120] S. P. Vyatchanin. "Effective cooling of quantum systems". *Soviet Physics Doklady* **22**, 321, 1977.

[121] R. Mankowsky, A. Subedi, M. Först, S. O. Mariager, M. Chollet, H. T. Lemke, J. S. Robinson, J. M. Glownia, M. P. Minitti, A. Frano, M. Fechner, N. A. Spaldin, T. Loew, B. Keimer, A. Georges, and A. Cavalleri. "Nonlinear lattice dynamics as a basis for enhanced superconductivity in $YBa_2Cu_3O_{6.5}$". *Nature* **516**, 71, 2014.

[122] M. Machida and S. Sakai. "Unified theory for magnetic and electric field coupling in multistacked Josephson junctions". *Physical Review B* **70**, 144520, 2004.

[123] T. Koyama and M. Tachiki. "I-V characteristics of Josephson-coupled layered superconductors with longitudinal plasma excitations". *Physical Review B* **54**, 16183, 1996.

[124] M. Machida and T. Koyama. "Localized rotating-modes in capacitively coupled intrinsic Josephson junctions: Systematic study of branching structure and collective dynamical instability". *Physical Review B* **70**, 024523, 2004.

[125] G. Schön and A. Zaikin. "Quantum coherent effects, phase transitions, and the dissipative dynamics of ultra small tunnel junctions". *Physics Reports* **198**, 237, 1990.

[126] S. Melchionna. "Design of quasisymplectic propagators for Langevin dynamics." *The Journal of Chemical Physics* **127**, 044108, 2007.

[127] D. B. Davidson. *Computational Electromagnetics for RF and Microwave Engineering*. 2nd ed. Cambridge: Cambridge University Press, 2011.

[128] J. R. Shewchuk. "Triangle: Engineering a 2D Quality Mesh Generator and Delaunay Triangulator". In: *Applied Computational Geometry: Towards Geometric Engineering*. Ed. by M. C. Lin and D. Manocha. Vol. 1148. Lecture Notes in Computer Science. Springer-Verlag, 1996.

[129] C. Geuzaine and J.-F. Remacle. "Gmsh: A 3D finite element mesh generator with built-in pre- and post-processing facilities". *International Journal for Numerical Methods in Engineering* **79**, 1309, 2009.

[130] B. Hanks. "CUBIT - Sandia National Laboratories". *https://cubit.sandia.gov/* 2015.

[131] G. Pelosi, R. Coccioli, and S. Selleri. *Quick Finite Elements for Electromagnetic Waves*. Norwood MA: Artech House, 1998.

[132] J. Jin. *The Finite Element Method in Electromagnetics*. New York: John Wiley & Sons, 2002.

[133] T. J. R. Hughes. *The Finite Element Method: Linear Static and Dynamic Finite Element Analysis*. New York: Dover Publications, 2000.

[134] W. Bangerth, R. Hartmann, and G. Kanschat. "deal.II—A general-purpose object-oriented finite element library". *ACM Transactions on Mathematical Software* **33**, 24, 2007.

[135] A. Logg, K.-A. Mardal, and G. Wells, eds. *Automated Solution of Differential Equations by the Finite Element Method*. Vol. 84. Lecture Notes in Computational Science and Engineering. Berlin, Heidelberg: Springer, 2012.

[136] L. N. Trefethen and D. Bau III. *Numerical Linear Algebra*. SIAM, 1997.

[137] W. Bangerth, C. Burstedde, T. Heister, and M. Kronbichler. "Algorithms and data structures for massively parallel generic adaptive finite element codes". *ACM Transactions on Mathematical Software* **38**, 14, 2011.

[138] T. A. Davis. "Algorithm 832: UMFPACK V4.3—an unsymmetric-pattern multifrontal method". *ACM Transactions on Mathematical Software* **30**, 196, 2004.

[139] P. R. Amestoy, I. S. Duff, J. Koster, and J.-Y. L'Excellent. "A fully asynchronous multifrontal solver using distributed dynamic scheduling". *SIAM Journal of Matrix Analysis and Applications* **23**, 15, 2001.

[140] P. R. Amestoy, A. Guermouche, J.-Y. L'Excellent, and S. Pralet. "Hybrid scheduling for the parallel solution of linear systems". *Parallel Computing* **32**, 136, 2006.

[141] J. C. Nédélec. "Mixed finite elements in R3". *Numerische Mathematik* **35**, 315, 1980.

[142] J. C. Nédélec. "A new family of mixed finite elements in R3". *Numerische Mathematik* **50**, 57, 1986.

[143] J. Nocedal and S. Wright. *Numerical Optimization*. 2nd ed. New York: Springer-Verlag New York, 2006.

[144] P. Langevin. "Sur la théorie du mouvement brownien". *Comptes Rendus de l'Académie des Sciences* **146**, 530, 1908.

[145] D. Frenkel and B. Smit. *Understanding Molecular Simulation*. Elsevier, 2002.

[146] C. W. Gardiner. *Handbook of Stochastic Methods for Physics, Chemistry, and the Natural Sciences, 3rd ed.* Vol. 13. Springer Series in Synergetics. Springer-Verlag, 2004.

[147] N. Van Kampen. *Stochastic Processes in Physics and Chemistry*. Elsevier, 1981.

[148] G. N. Milstein and M. V. Tretyakov. "Quasi-symplectic methods for Langevin-type equations". *IMA Journal of Numerical Analysis* **23**, 593, 2003.

[149] W. Coffey, Y. P. Kalmykov, and J. T. Waldron. *The Langevin Equation: With Applications to Stochastic Problems in Physics, Chemistry, and Electrical Engineering*. World Scientific, 2004.

[150] A. Ammar, B. Mokdad, F. Chinesta, and R. Keunings. "A new family of solvers for some classes of multidimensional partial differential equations encountered in kinetic theory modeling of complex fluids". *Journal of Non-Newtonian Fluid Mechanics* **139**, 153, 2006.

[151] A. Ammar, B. Mokdad, F. Chinesta, and R. Keunings. "A new family of solvers for some classes of multidimensional partial differential equations encountered in kinetic theory modelling of complex fluids". *Journal of Non-Newtonian Fluid Mechanics* **144**, 98, 2007.

[152] S. V. Dolgov, B. N. Khoromskij, and I. V. Oseledets. "Fast Solution of Parabolic Problems in the Tensor Train/Quantized Tensor Train Format with Initial Application to the Fokker–Planck Equation". *SIAM Journal on Scientific Computing* **34**, A3016, 2012.